NEW APPROACHES IN RADAR WAVEFORM DESIGN

by

DMITRY CHEBANOV

A dissertation submitted to the Graduate Faculty in Computer Science in partial fulfillment of the requirements for the degree of Doctor of Philosophy, The City University of New York

2008

This manuscript has been read and accepted for
the Graduate Faculty in Computer Science in satisfaction of
the dissertation requirement for the degree of Doctor of Philosophy.

Professor Irina Gladkova

Date — Chair of Examining Committee

Professor Ted Brown

Date — Executive Officer

Professor Octavio Betancourt

Professor Truong-Thao Nguyen

Professor Burton Randol

Dr. Vadim Potievsky

Supervisory Committee

THE CITY UNIVERSITY OF NEW YORK

Abstract

NEW APPROACHES IN RADAR WAVEFORM DESIGN

by

Dmitry Chebanov

Adviser: Professor Irina Gladkova

In this work we discuss two problems that appear in modern radar waveform design. First, we propose a new approach to one of the most challenging problems in this area of research - the construction of waveforms with optimal ambiguity characteristics in a chosen a priori region surrounding the main lobe. Our approach is based on the projection of the signal onto an appropriate orthonormal basis in the space of radar waveforms and approximating the signal with desired ambiguity properties by a finite number of basis waveforms. In particular, we consider well-known Hermite waveforms as the basis functions and discuss the problem of minimizing the volume under the ambiguity surface over a certain given region.

The second part of the dissertation is devoted to the problem of the range sidelobe suppression in stepped-frequency LFM pulse trains. Frequency stepping is one of the known techniques employed by modern radars to achieve high range resolution. The main advantage of this approach is that the instantaneous bandwidth of a radar is quite small compared with the total processing bandwidth. This allows the transmission of waveforms with extremely wide overall bandwidth (and, as a consequence, the attainment of high range resolution) without the usage of the expensive hardware needed to support the wide instantaneous bandwidth. We present a systematic approach for designing pulse trains producing the autocorrelation function whose sidelobes are less than some predetermined level.

Acknowledgements

I would like to express my sincere gratitude to all the people who have helped me in one way or another during my time at The Graduate Center of CUNY. First I would like to thank my advisor, Professor Irina Gladkova, for introducing me to an exciting research area - radar waveform design - and providing support, both academic and financial.

Next I want to thank the members of my supervisory committee for their guidance and countless discussions. I would also like to thank Professor Ted Brown for his kind support over the years.

Finally, I would like to say a word for my family. I wish to thank my parents and my brother for their love and guidance over the years. They have always supported and encouraged me to do my best in all matters of life. I would like to especially thank my wife, Olena, and my daughter, Valentyna, for their love and support throughout this entire process.

This research was partially supported by the U.S. Army Research Laboratory and the U.S. Army Research Office under Contract DAAD19-03-1-0329.

Contents

List of Tables

List of Figures

Chapter 1

Introduction

Radar (derived from "RAdio Detection And Ranging") is an electromagnetic system whose the basic purpose is to detect the presence of an object of interest and provide information concerning the object's location, motion, size, and other parameters. Radar is now extensively used in many applications – meteorology, mapping, air traffic control, ship and aircraft navigation, police speeding control, etc. It is now being used for mineral exploration and delineation and for land-mine detection. Of course, its primary role is in defense. The theory of radar is well developed and has many interesting and difficult theoretical and practical problems.

A radar system consists of a signal source or "transmitter" and a signal detector or "receiver". The transmitter radiates an electromagnetic signal which is scattered by objects in its environment. The resulting echoes are recorded by the receiver. In the simplest radar systems the directions of arrival, time delays and Doppler shifts of the echoes are used to estimate the directions, ranges and speeds of the scattering objects. The goal of a sophisticated system is to classify objects into identifiable classes by means of their echoes. This is an inverse scattering problem. An associated problem is that of waveform design; that is the choice of a signal

waveform which optimizes the information obtainable from the echoes.

Suitable waveform selection is an important problem in radar design, because it controls the resolution, clutter performance and computational complexity of the processing. The ambiguity function of a transmitted signal is the complex envelope of the matched-filter response in delay and doppler.

It measures the uncertainty with which the returning echo distinguishes, simultaneously, both ranges and velocities of a target system. The ambiguity function and its plot, the ambiguity surface, may be used to assess qualitatively how well a waveform can achieve the requirements of accuracy, ambiguity, resolution, and clutter rejection. Therefore, it is natural to use the ambiguity surface as a measure of performance in radar waveform design.

In this manuscript we propose new approaches for solving two problems appearing in the radar waveform design that have both theoretical and practical importance.

First, we discuss a new approach to one of the most challenging problems of the radar waveform design – the construction of waveforms with optimal ambiguity characteristics in a chosen a priori region surrounding the main lobe. Our approach is based on the projection of the signal onto an appropriate orthonormal basis in the space of radar waveforms and approximating the signal with desired ambiguity properties by a finite number of basis waveforms. In particular, we consider well-known Hermite waveforms as the basis functions and discuss the problem of minimizing the volume under the ambiguity surface over a certain given region. In the case of a circular region, we show that under some, rather general assumptions, a Hermite waveform of a certain order is a solution for this problem.

Next, we consider the problem of sidelobe suppression in stepped-frequency LFM pulse trains. Frequency stepping is one of the known techniques employed by mod-

ern radars to achieve high range resolution. The main advantage of this approach is that the instantaneous bandwidth of a radar is quite small compared with the total processing bandwidth. This allows the transmission of waveforms with extremely wide overall bandwidth (and, as a consequence, the attainment of high range resolution) without the usage of the expensive hardware needed to support the wide instantaneous bandwidth. In this thesis we present a systematic approach for designing pulse trains producing the autocorrelation function whose sidelobes are less than some predetermined level.

1.1 Ambiguity function and its properties

1.1.1 Definitions and notations

The ambiguity function of a complex-valued waveform $s(t)$ of finite energy is a complex two-dimensional function of $s(t)$:

$$\chi_s^*(\tau,\nu) = \int_{-\infty}^{\infty} s(t)\overline{s(t-\tau)}e^{-j2\pi\nu t}dt, \tag{1.1}$$

where $\overline{s(t)}$ means the complex conjugate of $s(t)$. The absolute value $|\chi_s^*(\tau,\nu)|$ of the ambiguity function is called the ambiguity surface.

The ambiguity function was first introduced by Woodward in his classical book [40]. The ambiguity function has an important practical meaning (see [8, 32, 35, 40]): it represents the output of a filter where a signal has been matched with its doppler-shifted and time-translated version. In more details, as a function of both time-delay τ and Doppler delay ν, the ambiguity function can be interpreted in two ways [8, 32]. First, we can think of the bank of filters, each matched to a different doppler, that constitute the matched-filter receiver for an unknown doppler shift. The ambiguity function describes the complete two-dimensional receiver response

in delay and doppler. Therefore, $|\chi^*(\tau, \nu)|$ represents the combined response of all filters of a doppler bank with infinitesimal spacing in ν. Alternatively, the ambiguity function gives the response of a single filter as the doppler coefficient of the received signal is varied.

As a consequence of these properties of the ambiguity function, combined resolution in delay and doppler could be analyzed as follows [8, 32]: We associate one ambiguity function with each target within the radar beam. These functions are translated with respect to each other in τ and ν, in accordance with the differential ranges and range rates of the targets. All functions then are superposed to obtain the combined receiver response to all targets. A cut through the superposition for constant doppler would then give the combined response of the single filter adjusted for that particular doppler. By analyzing such a response, we could determine which peaks are clearly recognizable as the central response lobes of herewith resolvable targets.

We remark here that the definition of the ambiguity function assumes the narrowband approximation [8, 22] for the received signal, which is usually adequate for radar applications. The structure of radar echo in this case is derived based on assumptions [8, 43] that (1) the speeds of the scattering objects are much less than the speed of radar waves (i.e., speed of light) and essentially constant during the interval required for the radar pulse to sweep over the objects; (2) the transmitter and receiver are in far field of the scattering objects; (3) secondary echoes due to the radar systems components as well as noise in the medium are negligible; etc. Publications [18, 32, 33, 34] demonstrate attempts to extend resolution theory beyond those assumptions.

We also remark that the name *ambiguity function* for $\chi^*(\tau, \nu)$ is somewhat misleading [35] since this function describes more about the waveform than just its am-

biguity properties. Woodward [40] coined the name to demonstrate that the total volume under this function is a constant, independent of the shape of the transmitted waveform (see property **P.7** on page 7). Thus the total area of ambiguity, or uncertainty, is the same no matter how $|\chi^*(\tau,\nu)|$ is distributed over (τ,ν)-plane.

We should note that the above way (1.1) to define $\chi^*(\tau,\nu)$ is only one of a few equivalent versions of ambiguity function's definition adopted in the radar literature (see [8, 22, 32] for further references on this topic). One says that formula (1.1) defines the ambiguity function of $s(t)$ in the asymmetrical form. Other very useful definition of the ambiguity function,

$$\chi_s(\tau,\nu) = \int_{-\infty}^{\infty} s\left(t+\frac{\tau}{2}\right)\,\overline{s\left(t-\frac{\tau}{2}\right)}\,e^{-j\,2\pi\nu t}\,dt, \tag{1.2}$$

which is said to be done in the symmetrical form, is chosen for theoretical studies because it simplifies the appearance of many theoretical results. One can show (see, for example, [32] for details) that the definitions (1.1) and (1.2) are related by a linear phase term $\chi_s^*(\tau,\nu) = e^{j\pi\tau\nu}\chi_s(\tau,\nu)$. The last immediately implies that $|\chi_s(\tau,\nu)| = |\chi_s^*(\tau,\nu)|$.

1.1.2 Some properties of ambiguity function

In what follows, extensive use of square-integrable function theory is made. So, we denote the space of all the functions $f(\mathbf{x}) : G \to \mathbb{C}$, where $G \subseteq \mathbb{R}^n$ and $\mathbf{x} = (x_1, x_2, \ldots, x_n) \in \mathbb{R}^n$, satisfying

$$\int_{-\infty}^{\infty} |f(\mathbf{x})|^2 d\mathbf{x} < \infty,$$

by $L^2(G)$. Clearly, $L^2(G) \subseteq L^2(\mathbb{R}^n)$ for $G \subseteq \mathbb{R}^n$. The inner product of $f(\mathbf{x}) \in L^2(G)$ and $g(\mathbf{x}) \in L^2(G)$ is

$$< f, g >_{L^2(G)} = \int_G f\overline{g}\; d\mathbf{x}$$

and the square of the resulting norm in $L^2(G)$ is

$$\|f\|^2_{L^2(G)} = < f, f >_{L^2(G)} = \int_G |f(\mathbf{x})|^2 d\mathbf{x}.$$

The ambiguity function has many remarkable properties (see [2, 8, 22, 32, 41], etc). Below we list the main ones.

- **P.1** (Time shift) If $s_1(t) = s(t - t_0)$, then $\chi_{s_1}(\tau, \nu) = e^{-j2\pi\nu t_0}\chi_s(\tau, \nu)$.
- **P.2** (Frequency shift) If $s_1(t) = s(t)e^{j2\pi ft}$, then $\chi_{s_1}(\tau, \nu) = e^{-j2\pi f\tau}\chi_s(\tau, \nu)$.
- **P.3** (Symmetry) $\chi_s(\tau, \nu) = \overline{\chi_s(-\tau, -\nu)}$ and $|\chi_s(\tau, \nu)| = |\chi_s(-\tau, -\nu)|$, that is $|\chi_s(\tau, \nu)|$ is symmetric with respect to the origin.
- **P.4** (Maximum) The largest value of the ambiguity function always is at the origin:

  $$|\chi_s(\tau, \nu)| \leq |\chi_s(0, 0)| = \|s\|^2_{L^2(\mathbb{R})}$$

  with strict inequality if $(\tau, \nu) \neq (0, 0)$.
- **P.5** (Scaling) If $s_1(t) = s(at)$, then $\chi_{s_1}(\tau, \nu) = \chi_s(a\tau, \nu/a)/|a|$.
- **P.6** (Quadratic Phase Property) If $s_1(t) = s(t)e^{j\pi\alpha t^2}$, then $\chi_{s_1}(\tau, \nu) = \chi_s(\tau, \nu - \alpha\tau)$.
- **P.7** (Volume Property) $\|\chi_s(\tau, \nu)\|^2_{L^2(\mathbb{R}^2)} = |\chi_s(0, 0)|^2 = \|s\|^4_{L^2(\mathbb{R})}$.
- **P.8**. $\chi_s(\tau, \nu) = \chi_{\overline{S}}(\nu, \tau)$, or

  $$\chi_s(\tau, \nu) = \int_{-\infty}^{\infty} S\left(f + \frac{\nu}{2}\right) \overline{S\left(f - \frac{\nu}{2}\right)} e^{-j\,2\pi\nu f}\, df,$$

  where $S(f)$ is the Fourier transform of $s(t)$ defined as $S(f) = \int_{-\infty}^{\infty} s(t)e^{-j2\pi ft}dt$.

- **P.9**. If $s(t)$ is a time-limited signal of duration T, then $\chi_s(\tau,\nu) = 0$ over $\{(\tau,\nu) : |\tau| \geq T, \nu \in \mathbb{R}\}$.

We should remark at this point that the above properties strongly constrain the set of two-dimensional functions that can be ambiguity surfaces. The volume under the surface must equal the square of the maximum. Any attempt to push down the ambiguity surface in one place makes it pop up somewhere else [2].

At the end of this subsection we observe that, by setting $\nu = 0$ in (1.1), we obtain the autocorrelation function of $s(t)$:

$$R_s(\tau) = \chi_s^*(\tau, 0) = \int_{-\infty}^{\infty} s(t)\overline{s(t-\tau)}dt$$

and, by setting $\tau = 0$ in (1.1), we have the Fourier transform of the square of the pulse:

$$R_s(\tau) = \chi_s^*(0, \nu) = \int_{-\infty}^{\infty} |s(t)|^2 e^{-j2\pi\nu t}dt. \tag{1.3}$$

As it can be seen from (1.3), all the waveforms of the same real envelope have the same ambiguity cross-section along doppler-delay axis. In particular, for all the pulses of constant amplitude, $|\chi_s(0,\nu)|$ has a sinc-like shape.

1.1.3 Ideal ambiguity function

If there were no theoretical restrictions, the ideal radar waveform would produce [8, 32, 35] an ambiguity function that is zero everywhere except the origin. The single peak at the origin eliminates any ambiguities, and its infinitesimal thickness permits the frequency and the echo delay time to be determined simultaneously to as high a degree of accuracy as desired. It would also permit the resolution of two targets no matter how close together they were on the ambiguity plot [35].

Unfortunately, the properties **P.4** and **P.7** of the ambiguity function prohibit this type of idealized behavior [8, 35].

A reasonable approximation to the ideal ambiguity surface might be a so-called "thumbtack" [8, 32] function which has a narrow central spike, with the bulk of the volume spread over a low-level pedestal surrounding the spike. The narowness of the central spike would guarantee adequate close-target resolvability, and the low level of the pedestal would seem to ensure low interference in the form of self-clutter. The properties of the "thumbtack" function for target resolution can be found in book [32].

1.1.4 The shape of ambiguity surface near the origin

The shape near the origin of the ambiguity surface of a waveform determines the accuracy of range and frequency measurements in a radar using that waveform, and also determines the ability of the radar to resolve two closely spaced targets.

The shape of the main lobe can be described more completely by describing the intersection of the main lobe with a horizontal plane. If the plane is high enough it slices through the main lobe just below the peak and the shape of the cut describes the shape of the main lobe near the peak. Report [41] contains the proof of the fact that, for waveforms having finite timewidth and bandwidth while their epoch and carrier frequencies both equal to zero, this intersection, within the quadratic approximation to $\chi_s(\tau, \nu)$, represents an ellipse in τ and ν which is known as the uncertainty ellipse. Review [2] extends this result to any waveforms whose ambiguity function has all the partial derivatives up to the second order inclusively. It is convenient to write the equation of the uncertainty ellipse down in terms of notations of paper [2]:

$$\tau^2 B_G^2 + 2\tau\nu T_G B_G \rho + \nu^2 T_G^2 = C.$$

Here T_G and B_G are Gabor timewidth and Gabor bandwidth, respectively. They can be computed by the formulas $T_G = \sqrt{\overline{t^2} - \overline{t}^2}$ and $B_G = \sqrt{\overline{f^2} - \overline{f}^2}$, where the time moments are $\overline{t^i} =< t^i s(t), s(t) >_{L^2(\mathbb{R})} /\|s(t)\|^2$ and the frequency moments are $\overline{f^i} =< f^i S(f), S(f) >_{L^2(\mathbb{R})} /\|s(t)\|^2$. There is also a skew parameter ρ defined as $\rho = Re[\overline{tf} - \overline{t}\,\overline{f}]/(T_G B_G)$.

The Gabor bandwidth and the Gabor timewidth are external descriptors of the waveform $s(t)$ in the sense that they can be measured from $|\chi_s(\tau, \nu)|$ without knowledge of the details of $s(t)$. The reciprocal of the Gabor timewidth of the pulse measures the width of the main lobe of the ambiguity surface in the ν direction and the reciprocal of the Gabor bandwidth measures the width of the main lobe of the ambiguity surface in the τ direction.

One of the problems that appears when a radar works in multi-target environment is to resolve the images of two (or more) objects in the range-velocity plane. If the objects have equal radar cross sections, they will be represented in the range-velocity plane by congruent elliptic discs, centered at points (τ_1, ν_1) and (τ_2, ν_2) and similarly oriented [41]. Evidently, the most difficult situation to resolve occurs when the ellipses have a common major axis. Based on the assumption that, in this situation, two objects are just resolved when the centers of the discs are one major semi-axis part, it is shown [41] that the smallest resolvable separation R (called the resolution constant of the waveform $s(t)$) in the range-velocity plane is given by

$$R^2 = \frac{2C^2}{T_G^2 + B_G^2 - \sqrt{(T_G^2 - B_G^2)^2 + 4T_G^2 B_G^2 \rho^2}}.$$

It is proven in [41] that, under practical limitations $T_G \leq T_G^0, B_G \leq B_G^0$, the best resolution constant obtainable is $R = C/\min(T_G^0, B_G^0)$.

We should mention here that the width of the main lobe may not be accurately described by the curvature at the peak. That is why in practice other measures [8, 30, 35] of resolution are used (e.g., 3dB width criterion, Rayleigh criterion, etc.).

1.2 Thesis outline

In this thesis we discuss two problems related to the area of radar waveform design and propose new ways for finding solutions to the problems.

In Chapter 2, we formulate and discuss the problem of approximating a given square-integrable two-dimensional function by ambiguity functions over a subregion of the Euclidean plane. We begin this chapter by recalling the main steps of the classical Wilcox's theory which allows one to perform such an approximation over the whole plane. Next, we give a new example illustrating how the Wilcox's theory can be used in the case when one seeks to approximate a surface of revolution. Then, we describe our model of a radar waveform which extends the Wilcox's class of radar waveforms. This model is used to formulate the problem of interest. Finally, we solve this problem for the case when the following assumptions are fulfilled: (i) the function to be approximated is the ideal ambiguity function, (ii) the waveform producing the ambiguity surface which provides the best approximation to the desired surface is restricted to the finite-dimensional linear spans of the well-known family of Hermite waveforms, and (iii) the approximation is done over either a circular region or a disk surrounding the origin.

In Chapter 3, we review some known classes of radar signals (e.g., a constant-frequency pulse, phase-coded waveforms, an LFM pulse, etc.) and discuss basic approaches to create a train of pulses. We also define a stepped-frequency LFM pulse train with a constant frequency step between the center frequencies of consecutive subpulses and describe some known issues associated with its matched filter response.

In Chapter 4, we propose a new approach for designing stepped-frequency LFM trains with variable frequency steps. We define the family of new waveforms and develop their ambiguity function (and, hence, autocorrelation function). Next, we

analyze the autocorrelation profile produced by proposed waveforms and show that it has desirable features (e.g., reduced range sidelobes and grating lobes). Finally, we study the shape of the ambiguity function of the proposed waveforms for non-zero Doppler shifts and compare the new waveforms with the traditional stepped-frequency pulse trains.

Finally, in Chapter 5, we summarize the results of this work.

Chapter 2

On the synthesis problem for a waveform having a desired ambiguity profile

2.1 Background

The ambiguity function is of fundamental importance in the theory of radar. The use of the ambiguity function to estimate the range and velocity of targets is basic to the theory. The foundations of mathematical theory of radar have been laid down by Calvin Wilcox in his famous 1960 technical report [41]. (The report was published [42] for the first time in 1991.) In this section we recall some important results that will be useful in our work.

2.1.1 Orthogonal expansions of ambiguity functions

In his report [41], Wilcox defines the class $\mathcal{W}^0$ of radar waveforms and the class $\mathcal{X}^0$ of the ambiguity functions of the members of $\mathcal{W}^0$ as follows.

DEFINITION 2.1.1 *A function $s(t)$ is in class $\mathcal{W}^0$ if and only if $s(t), ts(t)$, and $fS(f)$ are in $L^2(\mathbb{R})$, and $\|s(t)\|_{L^2(\mathbb{R})} = 1, < ts(t), s(t) >_{L^2(\mathbb{R})} = < fS(f), S(f) >_{L^2(\mathbb{R})} = 0$.*

DEFINITION 2.1.2 *A function $\chi(\tau, \nu)$ is in class $\mathcal{X}^0$ if and only if $\chi(\tau, \nu) = \chi_s(\tau, \nu)$, where $\chi_s(\tau, \nu)$ is defined by (1.2) and $s(t) \in \mathcal{W}^0$.*

Based on the assumptions mentioned in Definition 2.1.1, the following properties of the elements of $\mathcal{W}^0$ have been proven.

THEOREM 2.1.1 *[41]. The following statements hold.*

1) $s(t) \in \mathcal{W}^0 \Longleftrightarrow S(f) \in \mathcal{W}^0$.

2) $s(t) \in \mathcal{W}^0 \Longrightarrow$

(i) *$s(t)$ and $S(f)$ are in $L^1(\mathbb{R})$;*

(ii) *$s'(t)$ and $S'(f)$ exist almost everywhere and are in $L^2(\mathbb{R})$;*

(iii) *$s(t)$ and $S(f)$ are continuous and bounded on $(-\infty, +\infty)$ and*

$$\lim_{|t|\to\infty} s(t) = 0, \qquad \lim_{|f|\to\infty} S(f) = 0.$$

It was shown [41] that there exists a sequence of members of $\mathcal{W}^0$

$$\phi_0(t), \quad \phi_1(t), \quad \ldots, \quad \phi_m(t), \quad \ldots \tag{2.1}$$

which is complete and orthonormal in $L^2(\mathbb{R})$. Then, by the Riesz-Fischer theorem [31], each $s(t) \in \mathcal{W}^0$ can be represented as

$$s(t) = \lim_{N\to\infty} \sum_{m=0}^{N} a_m \phi_m(t), \tag{2.2}$$

where $a_m = < s(t), \phi_m(t) >_{L^2(\mathbb{R})}$ and $\lim\limits_{N\to\infty} \sum\limits_{m=0}^{N} |a_m|^2 = 1$.

Sequence (2.1) induces the family of the cross-ambiguity functions

$$\psi_{mn}(\tau, \nu) = \int_{-\infty}^{\infty} \phi_m \left(t - \frac{\tau}{2}\right) \overline{\phi_n \left(t + \frac{\tau}{2}\right)}\, e^{-j\,2\pi\nu t}\, dt \tag{2.3}$$

which is also known [41] to be orthonormal and complete in $L^2(\mathbb{R}^2)$. Hence, every square-integrable function $F(\tau,\nu)$ satisfies

$$F(\tau,\nu)=\lim_{N\to\infty}\sum_{k=0}^{N}\sum_{m=0}^{N}b_{km}\psi_{km}(\tau,\nu) \tag{2.4}$$

with $b_{km}=<F(\tau,\nu),\psi_{km}(\tau,\nu)>_{L^2(\mathbb{R}^2)}$ and $\lim\limits_{N\to\infty}\sum\limits_{k,m=0}^{N}|b_{km}|^2<\infty$. In particular, any ambiguity function $\chi(\tau,\nu)\in\mathcal{X}^0$ can be expanded in a series (2.4) such that $b_{km}=<\chi(\tau,\nu),\psi_{km}(\tau,\nu)>_{L^2(\mathbb{R}^2)}$ and $\lim\limits_{N\to\infty}\sum\limits_{k,m=0}^{N}|b_{km}|^2=1$. Furthermore, in this case the b_{km}'s are related to the coefficients of the signal expansion (2.2) by the formula (see [41])

$$b_{km}=a_k\overline{a}_m. \tag{2.5}$$

2.1.2 Hermite waveforms – an example of orthonormal basis in $\mathcal{W}^0$

Hermite waveforms defined [19, 41] as follows

$$u_n(t)=\frac{2^{1/4}}{\sqrt{n!}}\,H_n(2\sqrt{\pi}\,t)e^{-\pi t^2},\quad n=0,1,2,\ldots, \tag{2.6}$$

where $H_n(x)$ is the nth Hermite polynomial

$$H_n(x)=(-1)^n e^{\frac{x^2}{2}}\left(\frac{d}{dx}\right)^n e^{\frac{-x^2}{2}},\quad n=0,1,2,\ldots$$

provide a well-known and quite interesting example of the basis (2.1).

Hermite waveforms as well as their ambiguity functions have many remarkable properties [4, 14, 19, 28, 37, 38, 41]. Below we recall some of them.

I. *Sequence* (2.6) *is complete and orthonormal in* $L^2(\mathbb{R})$. Moreover, $u_n(t)\in\mathcal{W}^0\,\forall n$. Hence, the functions set (2.6) may be chosen as a basis (2.1) of $\mathcal{W}^0$.

II. *Hermite waveform* $u_n(t)$ *is proportional to its Fourier transform* $U_n(f)$. *More precisely,* $U_n(f)=(-j)^n u_n(f),\ n=0,1,2,\ldots$

III. *The cross-ambiguity functions* $\xi_{mn}(\tau,\nu)$ $(n,m=0,1,2,\ldots)$ *obtained from the sequence* $\{u_n(t)\}$ *by means of rule* (2.3) *form a complete and orthonormal set in* $L^2(\mathbb{R}^2)$. It is especially convenient to represent them, for all $m,n\geq 0$, as functions of the polar coordinates (r,θ) defined by $\tau+j\nu=re^{j\,\theta}$:

$$\xi_{mn}\left(\frac{\tau}{\sqrt{\pi}}\,,\frac{\nu}{\sqrt{\pi}}\right)=\sqrt{\pi}\;\Xi_{ik}(r)e^{j\,k\theta}, \tag{2.7}$$

where

$$\Xi_{ik}(r)=(-1)^{\frac{|k|+k}{2}}\sqrt{\frac{i!}{\pi(i+|k|)!}}\;e^{-\frac{r^2}{2}}r^{|k|}L_i^{(|k|)}(r^2), \tag{2.8}$$

$i=(m+n-|m-n|)/2,\ k=m-n$, and $L_i^{(l)}(x)(l,x\geq 0)$ is the generalized Laguerre polynomial defined by

$$L_i^{(l)}(x)=\frac{1}{i!}e^x x^{-l}\left(\frac{d}{dx}\right)^n(x^{n+l}e^{-x})\quad\text{for}\quad x\geq 0. \tag{2.9}$$

IV. It follows particularly from formula (2.7) that *the (auto)ambiguity function,*

$$\xi_{mm}\left(\frac{\tau}{\sqrt{\pi}}\,,\frac{\nu}{\sqrt{\pi}}\right)=e^{-\frac{r^2}{2}}L_m^{(0)}(r^2),$$

produced by the m*th Hermite waveform takes only real values and exhibits a circular symmetry,* i.e. *its ambiguity surface is invariant with respect to rotation about the origin.* So, to imagine the entire surface it is enough to know only one of the cross-sections passing through the origin. All others are exactly the same. Figure 2.1 illustrates the Hermite waveform $u_{100}(t)$ and an arbitrary passing through the origin cross-section of its auto-ambiguity surface $\xi_{100,100}(\tau,\nu)$.

V. *Let* $\chi_u(\tau,\nu)$ *and* $\chi_{u_\theta}(\tau,\nu)$ *be the ambiguity functions of waveforms*

$$u(t)=\sum_{m=0}^{\infty}a_m u_m(t)\qquad\textit{and}\qquad u_\theta(t)=\sum_{m=0}^{\infty}e^{-jm\theta}a_m u_m(t),$$

respectively. Then, $\chi_{u_\theta}(\tau,\nu)=\chi_u(\tau\cos\theta+\nu\sin\theta,-\tau\sin\theta+\nu\cos\theta)$, i.e. the ambiguity function for $u_\theta(t)$ is obtained by rotating $\chi_u(\tau,\nu)$ through the angle θ about the origin.

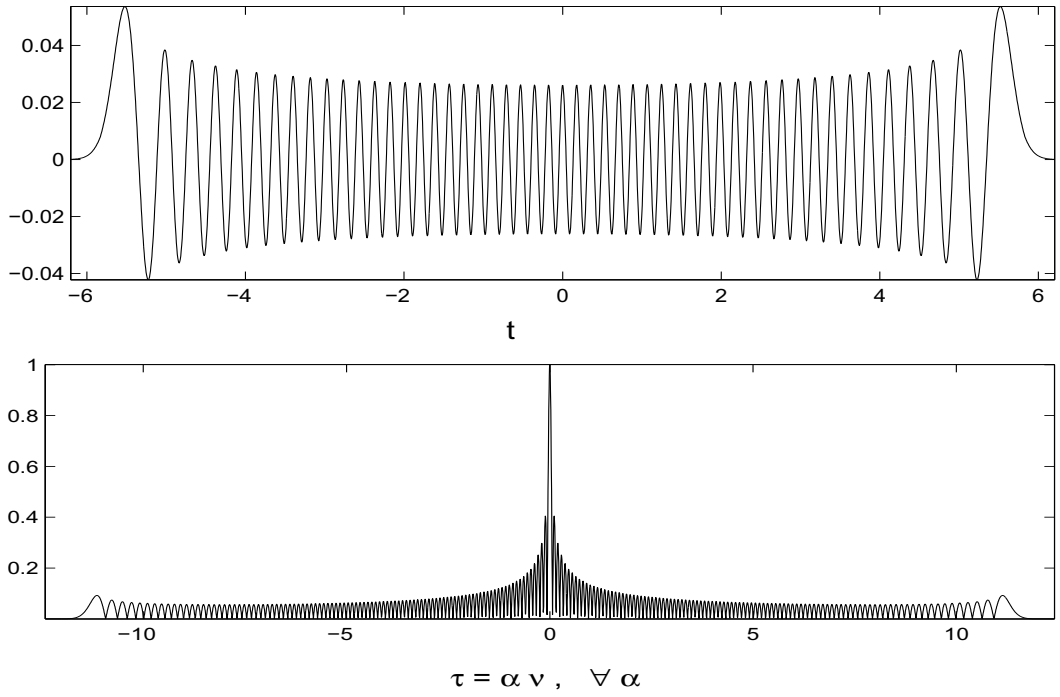

Figure 2.1: Hermite waveform $u_{100}(t)$ (top) and arbitrary cross-section passing through the origin for its ambiguity surface (bottom)

VI. Let us denote by Ω_n the set of all waveforms $u^*(t) = P_n(t)e^{-\pi t^2}$ with the degree of the polynomial $P_n(t)$ not greater that n. (Hardy's theorem (see [41]) shows that the waveforms of the class $\Omega = \Omega_0 \cup \Omega_1 \cup \Omega_2 \cup \ldots$ are the only ones that have the same order at infinity as their Fourier transforms. If a waveform $u(t)$ is smaller at infinity than every waveform in Ω, then $U(f)$ is larger at infinity than every waveform in Ω, and conversely. Thus the waveforms Ω present themselves naturally as the waveforms that are "small at infinity" and can be used as an acceptable approximation of waveforms having finite bandwidth and time duration – requirements desired from engineering viewpoint.) The following result holds [41]: *Among all waveforms from Ω_n, the nth Hermite waveform has the smallest (in the sense of the mainlobe width) resolution parameter,* i.e., it provides the best (with respect to all other elements of Ω_n) capabilities to resolve two or more closely located targets.

2.1.3 Approximation of an arbitrary function by ambiguity functions

One of the ways to design waveforms with good ambiguity characteristics is, first, to invent a function $F(\tau,\nu) \in L^2(\mathbb{R}^2)$ having desirable properties and, then, find the ambiguity function which most closely approximates it. In other words, we come to the following optimization problem.

PROBLEM 2.1.1 *For a given candidate function $F(\tau,\nu) \in L^2(\mathbb{R}^2)$, find the waveform(s) $s(t) \in L^2(\mathbb{R})$ which corresponds to the projection of $F(\tau,\nu)$ on $\mathcal{X}^0$.*

The complete solution to this problem was provided by Wilcox [41] and further generalized by Sussman [36]. It is expressed by the following theorem.

THEOREM 2.1.2 *Problem 2.1.1 always has solutions. Namely, the minimum is $2(1-\mu_0)$ where μ_0 is the largest eigenvalue of*

$$\int_{-\infty}^{\infty} H(x,y)u(y)dy = \mu u(x)$$

and function $H\left(t-\frac{\tau}{2}, t+\frac{\tau}{2}\right)$ is the inverse Fourier transform of $F(\tau,\nu)$ with respect to the variable ν. The minimum is attained for any $u(x)$ that is an eigenfunction corresponding to μ_0.

A variant of Problem 2.1.1 that is of practical interest arises when we restrict $s(t)$ to a finite-dimensional space, say,

$$s(t) = \sum_{m=0}^{N} a_m \phi_m(t) \quad \text{and} \quad \|s(t)\|^2 = \sum_{m=0}^{N} |a_m|^2 = 1. \tag{2.10}$$

In this case Problem 2.1.1 can be reformulated as follows.

PROBLEM 2.1.2 *Assume that some orthonormal basis* (2.1) *is fixed. Then, given a candidate function $F(\tau,\nu) \in L^2(\mathbb{R}^2)$ and a positive integer N, find $s(t)$ satisfying*

(2.10) *that minimizes*

$$\|F(\tau,\nu) - \chi_s(\tau,\nu)\|^2_{L^2(\mathbb{R}^2)}. \tag{2.11}$$

The solution for Problem 2.1.2 is given by the following theorem:

THEOREM 2.1.3 *[36, 41] The minimum of* (2.11) *is* $2(1-\mu_0)$ *where* μ_0 *is the largest eigenvalue of the Hermitian matrix* $\{b_{km}\}$. *It is attained by the waveform* (2.2) *where* $(a_0, a_1, \ldots, a_N)$ *is any eigenvector for* $\{b_{km}\}$ *corresponding to* μ_0.

2.2 Preliminaries

2.2.1 Mathematical model of a radar waveform

In this section we formulate the mathematical model of a radar waveform we will work with in this chapter. Every signal $s(t)$ is assumed to be a real-valued or complex-valued function of time with finite energy. In what follows we restrict our attention to the unit energy signals having finite timewidth and bandwidth.

DEFINITION 2.2.1 *A function* $s(t)$ *(called a waveform) is in class* $\mathcal{W}$ *if and only if* $s(t), ts(t)$, *and* $\omega S(\omega)$ *are in* $L^2(\mathbb{R})$ *and* $\|s(t)\|_{L^2(\mathbb{R})} = 1$.

The above definition does not contain any assumptions regarding waveform's epoch and carrier frequency which we define by $< ts(t), s(t) >_{L^2(\mathbb{R})}$ and $< fS(f), S(f) >_{L^2(\mathbb{R})}$, respectively. It is clear, however, that these quantities are finite for any member of $\mathcal{W}$ (this fact follows from our assumption about square-integrability of $s(t), ts(t)$, and $fS(f)$, and Cauchy-Schwarz inequality). In particular, $\mathcal{W}$ contains all the waveforms whose epoch and carrier frequency are both equal to zero. If these additional assumptions are fulfilled for some $s(t) \in \mathcal{W}$, then, by Definition 2.1.1, $s(t) \in \mathcal{W}^0$; otherwise, $s(t)$ is not in $\mathcal{W}^0$. Hence, $\mathcal{W}^0 \subset \mathcal{W}$. Thus, we have extended,

comparing with Wilcox's model [41], the class of waveforms under consideration. Note that such an extension preserves the properties mentioned in Theorem 2.1.1. The last follows from the observation that the proof of Theorem 2.1.1 remains correct for any $s(t) \in \mathcal{W}$ (not only for $s(t) \in \mathcal{W}^0$).

The structure of the set $\mathcal{W}$ can be further analyzed by means of the following lemma.

LEMMA 2.2.1 *If* $s(t) \in \mathcal{W}$ *and*

$$u(t) = s(t + t_0)e^{-j2\pi f_0(t+t_0)}, \tag{2.12}$$

where $t_0 =< ts(t), s(t) >_{L^2(\mathbb{R})}$ *and* $f_0 =< fS(f), S(f) >_{L^2(\mathbb{R})}$, *then* $u(t) \in \mathcal{W}^0$.

PROOF. Obviously, $s(t) \in L^2(\mathbb{R}) \Longrightarrow u(t) \in L^2(\mathbb{R})$ and $\|u(t)\|_{L^2(\mathbb{R})} = \|s(t)\|_{L^2(\mathbb{R})} = 1$. Next, applying straightforward transformations, one can easily obtain that

$$\begin{aligned} < tu(t), u(t) >_{L^2(\mathbb{R})} &=< ts(t + t_0), s(t + t_0) >_{L^2(\mathbb{R})} =< (t - t_0)s(t), s(t) >_{L^2(\mathbb{R})} \\ &=< ts(t), s(t) >_{L^2(\mathbb{R})} - t_0\|s(t)\|_{L^2(\mathbb{R})} = 0 \end{aligned} \tag{2.13}$$

and

$$\begin{aligned} \|tu(t)\|^2_{L^2(\mathbb{R})} &= \|ts(t + t_0)\|^2_{L^2(\mathbb{R})} = \|(t - t_0)s(t)\|^2_{L^2(\mathbb{R})} \\ &= \|ts(t)\|^2_{L^2(\mathbb{R})} - 2t_0 < ts(t), s(t) >_{L^2(\mathbb{R})} + t_0^2\|s(t)\|^2_{L^2(\mathbb{R})} \\ &= \|ts(t)\|^2_{L^2(\mathbb{R})} - t_0^2 < \infty. \end{aligned} \tag{2.14}$$

Thus, $u(t)$ and $tu(t)$ are in $L^2(\mathbb{R})$ and $< tu(t), u(t) >_{L^2(\mathbb{R})} = 0$.

To show that $fU(f) \in L^2(\mathbb{R})$ and $< fU(f), U(f) >_{L^2(\mathbb{R})} = 0$, it is enough to observe that $U(f) = S(f + f_0)e^{j2\pi f t_0}$ and perform the transformations analogous to (2.13) and (2.14).

It follows from the above lemma that relation (2.12) defines an onto function that maps each element $s(t) \in \mathcal{W}$ to the appropriate (unique) element $u(t) \in \mathcal{W}^0$

(any member of $\mathcal{W}^0$ is mapped to itself). It is also possible to introduce an inverse mapping from $\mathcal{W}^0$ to $\mathcal{W}$ defined by

$$s(t) = u(t - t_0)e^{j2\pi f_0 t}, \tag{2.15}$$

where functions $s(t)$ and $u(t)$ and quantities t_0 and f_0 have the same meaning as in Lemma 2.2.1. Note that equality (2.15) can be interpreted in the following manner: starting with Wilcox's class $\mathcal{W}^0$, we can generate set $\mathcal{W}$ by applying (2.15), for all real-valued t_0 and f_0, to all the members of $\mathcal{W}^0$. This observation can be used as an equivalent definition of class $\mathcal{W}$.

Next, we define the class of the ambiguity functions produced by the elements of $\mathcal{W}$ as follows.

DEFINITION 2.2.2 *A function $\chi(\tau, \nu)$ is in class $\mathcal{X}$ if and only if $\chi(\tau, \nu) = \chi_s(\tau, \nu)$, where $\chi_s(\tau, \nu)$ is defined by* (1.2) *and $s(t) \in \mathcal{W}$.*

It is clear that $\mathcal{X}^0 \subset \mathcal{X}$. Moreover, based on Lemma 2.2.1 and properties **P.1** and **P.2** of the ambiguity function, we can relate the ambiguity function of any waveform $s(t) \in \mathcal{W}$ to the ambiguity function of $u(t)$, given by (2.12), by the formula $\chi_u(\tau, \nu) = \chi_s(\tau, \nu)e^{j2\pi(f_0\tau + t_0\nu)}$. This relation can be thought as the definition of an onto function from $\mathcal{X}$ to $\mathcal{X}^0$ which is similar to that one (see (2.12)) we have in the waveform's space. Hence, starting with class $\mathcal{X}^0$, we can generate all the members of $\mathcal{X}$ by the rule

$$\chi_s(\tau, \nu) = \chi_u(\tau, \nu)e^{-j2\pi(f_0\tau + t_0\nu)}, \tag{2.16}$$

for all $(t_0, f_0) \in \mathbb{R}^2$; that is, the above relation defines class $\mathcal{X}$ in terms of its subclass $\mathcal{X}^0$, from which it can be generated.

One of the most interesting consequences of (2.16) is that $|\chi_s(\tau, \nu)| = |\chi_u(\tau, \nu)|$, that is, for any waveform $s(t) \in \mathcal{W}$, we can always find an element $u(t)$ in $\mathcal{W}^0$ having the same ambiguity surface. In other words, class $\mathcal{X}^0$ contains all possible

"distinct" ambiguity surfaces that can be found in $\mathcal{X}$. Taking into account this remark, it might seem that the extension of Wilcox's model we propose in this section is somewhat unnecessary. However, as we show in the next subsection, class $\mathcal{W}$ becomes useful when one studies linear spans of elements from $\mathcal{W}^0$: in general, a linear combination of any finite number of members from $\mathcal{W}^0$ does not belong to $\mathcal{W}^0$.

Finally, we would like to note that most of the properties of the ambiguity function, we have mentioned in section 2.1, are still fulfilled for some functions that does not belong to $\mathcal{W}$. Despite of this fact, we prefer the waveform's model described here, because it preserves an important (from point of view of engineering requirements) property: all the waveforms under consideration have finite timewidth and bandwidth.

2.2.2 Finite-dimensional subclasses of $\mathcal{W}$

In this subsection we introduce the sequence of finite-dimensional subclasses of $\mathcal{W}$ as follows

DEFINITION 2.2.3 *Let* $\{\phi_m(t)\}_{m=0}^{\infty}$ *be some basis* (2.1) *from* $\mathcal{W}^0$. *A function* $s(t)$ *is in class* $\mathcal{W}_N = \mathcal{W}_N(\{\phi_m(t)\}_{m=0}^{N})\,(N = 0, 1, \ldots)$ *if and only if*

$$s(t) = \sum_{m=0}^{N} a_m \phi_m(t) \tag{2.17}$$

such that $a_m = < s(t), \phi_m(t) >_{L^2(\mathbb{R})}$ *and* $a_m \in \mathfrak{S}_N$, *where* $\mathfrak{S}_N$ *is the* N*-dimensional unit sphere:* $\sum\limits_{m=0}^{N} |a_m|^2 = 1$.

The following lemma states some simple relations between subclasses $\mathcal{W}_N$ and $\mathcal{W}$.

LEMMA 2.2.2 ***1)*** $\mathcal{W}_0 \subset \mathcal{W}_1 \subset \mathcal{W}_2 \subset \ldots$; ***2)*** $\mathcal{W}_N \subset \mathcal{W}$, *for* $N = 0, 1, 2, \ldots$.

PROOF. The correctness of the first statement is evident. To prove the second claim we assume that some natural N and some basis $\{\phi_m(t)\}_{m=0}^N$ of $\mathcal{W}^0$ (see (2.1)) are fixed. Consider any $s(t) \in \mathcal{W}_N$. Taking into account Definition 2.2.3 and orthonormality of $\{\phi_m(t)\}_{m=0}^N$, we find:

$$\|s(t)\|^2_{L^2(\mathbb{R})} = \left\| \sum_{m=0}^{N} a_m \phi_m(t) \right\|^2_{L^2(\mathbb{R})} = \sum_{m=0}^{N} |a_m|^2 \|\phi_m(t)\|^2_{L^2(\mathbb{R})} = 1.$$

Next, we observe that, for $m = 0, 1, 2, \ldots, N$, $\phi_m(t) \in \mathcal{W}^0$ and $a_m \in \mathfrak{S}_N$ imply $\|t\phi_m(t)\|_{L^2(\mathbb{R})} \leq \infty$ and $0 \leq |a_i| \leq 1$, respectively. Then, applying the triangle inequality yields

$$\begin{aligned} \|ts(t)\|_{L^2(\mathbb{R})} &= \left\| \sum_{m=0}^{N} a_m t\phi_m(t) \right\|_{L^2(\mathbb{R})} \leq \sum_{m=0}^{N} \|a_m t\phi_m(t)\|_{L^2(\mathbb{R})} \\ &= \sum_{m=0}^{N} |a_m| \|t\phi_m(t)\|_{L^2(\mathbb{R})} \leq \sum_{m=0}^{N} \|t\phi_m(t)\|_{L^2(\mathbb{R})} < \infty. \end{aligned} \tag{2.18}$$

Thus, we have proved that both $s(t)$ and $ts(t)$ are in $L^2(\mathbb{R})$ and $\|s(t)\|_{L^2(\mathbb{R})} = 1$.

Note that (i) $S(f) = \sum_{m=0}^{N} a_m \Phi_m(f)$, where $\Phi_m(f)$ is the Fourier transform of $\phi_m(t)$, and (ii) $\|f\Phi_m(f)\|_{L^2(\mathbb{R})} < \infty$ $(m = 0, 1, 2, \ldots, N)$, since $\phi_m(t) \in \mathcal{W}$. Now one can easily check that $\|fS(f)\|_{L^2(\mathbb{R})} < \infty$ by applying the sequence of transformations similar to (2.18). This completes the proof of the lemma.

According to Lemma 2.2.2, any waveform $s(t)$ from $\mathcal{W}_N$ is a member of $\mathcal{W}$. To say about its membership in $\mathcal{W}^0$, we have to check whether its epoch and carrier frequency are both equal to zero. The following example demonstrates that, generally speaking, it is not the case.

Example. Consider $s(t) \in \mathcal{W}_1$, that is $s(t) = a_0\phi_0(t) + a_1\phi_1(t)$ such that $|a_0|^2 + |a_1|^2 = 1$. Then,

$$\begin{aligned} < ts(t), s(t) >_{L^2(\mathbb{R})} = |a_0|^2 < t\phi_0(t), \phi_0(t) >_{L^2(\mathbb{R})} + |a_1|^2 < t\phi_1(t), \phi_1(t) >_{L^2(\mathbb{R})} \\ + 2\Re \left\{ a_0 \overline{a}_1 < t\phi_0(t), \phi_1(t) >_{L^2(\mathbb{R})} \right\}. \end{aligned} \tag{2.19}$$

Since $\phi_0(t), \phi_1(t) \in \mathcal{W}^0$, the first two summands in (2.19) are equal to zero and

$$< ts(t), s(t)) >_{L^2(\mathbb{R})} = 2\rho_0\rho_1 \Re\left\{e^{j(\theta_0-\theta_1)} < t\phi_0(t), \phi_1(t)) >_{L^2(\mathbb{R})}\right\},$$

where $\rho_i = |a_i|, \theta_i = \angle a_i, i = 0, 1$. Likewise,

$$< fS(f), S(f)) >_{L^2(\mathbb{R})} = 2\rho_0\rho_1 \Re\left\{e^{j(\theta_0-\theta_1)} < f\Phi_0(f), \Phi_1(f)) >_{L^2(\mathbb{R})}\right\}.$$

At this point, we assume additionally that $\phi_0(t)$ and $\phi_1(t)$ are the first two Hermite waveforms defined by (2.6). Then, $t\phi_0(t) = \phi_1(t)/(2\sqrt{\pi}), \Phi_0(f) = \phi_0(f)$ and $\Phi_1(f) = -j\phi_1(f)$. Therefore, $\sqrt{\pi} < ts(t), s(t)) >_{L^2(\mathbb{R})} = \rho_0\rho_1 \cos(\theta_0 - \theta_1)$ and $\sqrt{\pi} < fS(f), S(f)) >_{L^2(\mathbb{R})} = \rho_0\rho_1 \sin(\theta_0 - \theta_1)$. If $s(t)$ were in $\mathcal{W}_1^0$, it would satisfy

$$< ts(t), s(t)) >^2_{L^2(\mathbb{R})} + < fS(f), S(f)) >^2_{L^2(\mathbb{R})} = 0 \quad \Longrightarrow \quad \rho_0^2\rho_1^2 = 0.$$

The last equality can be fulfilled only if either ρ_0 or ρ_1 equals zero. Hence, in our example, functions of the form $e^{j\theta_i}\phi_i(t)$ $(i = 0, 1)$ are the only members of $\mathcal{W}_1^0$.

At the end of this section, we define the sequence of classes $\mathcal{X}_N$ $(N = 0, 1, 2, \ldots)$ containing the ambiguity functions of the waveforms from $\mathcal{W}_N$.

DEFINITION 2.2.4 *A function $\chi(\tau, \nu)$ is in class $\mathcal{X}_N$ if and only if $\chi(\tau, \nu) = \chi_s(\tau, \nu)$, where $\chi_s(\tau, \nu)$ is defined by* (1.2) *and $s(t) \in \mathcal{W}_N$.*

Based on Definition 2.2.4 and the above discussion, one can derive directly a couple of properties of the $\mathcal{X}_N$s. For instance, by analogy with the proof of Lemma 2.2.2, one can show that (1) $\mathcal{X}_0 \subset \mathcal{X}_1 \subset \mathcal{X}_2 \subset \ldots$ and (2) $\mathcal{X}_N \subset \mathcal{X}$, for $N = 0, 1, 2, \ldots$. Other straightforward property formulated in the below lemma follows from the facts mentioned in section 2.1.1.

LEMMA 2.2.3 *Let $\{\phi_m(t)\}_{m=0}^N$ be some finite-dimensional basis* (2.1) *constituting the class $\mathcal{W}_N$. Then, any ambiguity function $\chi(\tau, \nu) = \chi_s(\tau, \nu) \in \mathcal{X}_N$ can be ex-*

panded in a finite series

$$\chi(\tau,\nu)=\sum_{k=0}^{N}\sum_{m=0}^{N}b_{km}\psi_{km}(\tau,\nu), \tag{2.20}$$

where $\{\psi_{km}(\tau,\nu)\}_{k,m=0}^{N}$ *is the sequence* (2.3) *of cross-ambiguity functions induced by basis functions* $\{\phi_m(t)\}_{m=0}^{N}$ *and the elements of the sequence* $\{b_{km}\}_{k,m=0}^{N}$ *admit representation* (2.5) *through the coefficients of expansion* (2.17) *of the appropriate waveform* $s(t)\in\mathcal{W}_N$.

The classes $\mathcal{X}_N$ play the key role in the rest of this chapter where we discuss various formulations of the problem about finding the projection(s) (in the mean square sense) of a given function on $\mathcal{X}_N$.

2.3 Application of Wilcox's Method: Approximation of a Surface of Revolution

In this section we give an example of the usage of classical Wilcox's method described in section 2.1.3.

We consider the problem of finding the projection of a given function $F(\tau,\nu)\in L^2(\mathbb{R}^2)$ on $\mathcal{X}_N$, i.e. Problem 2.1.2. We recall from subsection 2.1.3 that Wilcox's algorithm mentioned there provides a way to find the solution(s) of the problem in the general case. Our goal here is to demonstrate the application of his approach for specific class of functions $F(\tau,\nu)$ and specific, appropriately chosen, basis $\{\phi_m(t)\}_{m=0}^{N}$. In more details, we assume additionally that $F(\tau,\nu)$ has a circular symmetry. At the same time, as we have seen in subsection 2.1.2, the ambiguity functions $\xi_{mm}(\tau,\nu)$ of Hermite waveforms (2.6) themselves exhibit a circular symmetry. Taking into account this fact as well as other properties of the family of the cross-ambiguity functions (2.7), it is natural to choose the Hermite waveforms as basis functions in

our example. Then, the following theorem holds.

THEOREM 2.3.1 *Let $F(\tau,\nu) \in L^2(\mathbb{R}^2)$ be a radial function and N is an arbitrary natural number. Then $\xi_{pp}(\tau,\nu)$ is the best approximation of $F(\tau,\nu)$ in the $L^2(\mathbb{R}^2)$ sense in the class $\mathcal{X}_N$, where p is the index corresponding to the largest by absolute value coefficient b_{pp} in the decomposition* (2.4) *of $F(\tau,\nu)$ into basis $\{\xi_{nm}(\tau,\nu)\}_{n,m=0}^{N}$.*

PROOF. We observe that functions $F(\tau,\nu)$ and $\xi_{nm}(\tau,\nu)$ $(n,m = 0,1,2,\ldots,N)$ can be represented in the polar coordinates (r,θ) defined by $\tau + j\nu = re^{j\,\theta}$ as follows: $F(\tau,\nu) = H(r)$ (due to the circular symmetry of $F(\tau,\nu)$) and $\xi_{nm}(\tau,\nu) = \widetilde{\xi}_{nm}(r)e^{j(n-m)\theta}$ (due to property III in section 2.1.2), where $H(r)$ and $\{\widetilde{\xi}_{nm}(r)\}_{n,m=0}^{N}$ are some functions of r. Since the sequence $e^{jk\theta}$ $(k = -N,-N+1,\ldots,N-1,N)$ is orthogonal on $0 \le \theta \le 2\pi$, we obtain, for $n \neq m$,

$$< F(\tau,\nu), \xi_{mn}(\tau,\nu) >_{L^2(\mathbb{R}^2)} = \int_0^\infty H(r)\widetilde{\xi}_{nm}(r)rdr \int_0^{2\pi} e^{j(n-m)\theta}d\theta = 0.$$

Therefore, the matrix $\{b_{nm}\}_{n,m=0}^{N}$ in Theorem 2.1.3 is diagonal with the entries $b_{mm} =< F(\tau,\nu), \xi_{mm}(\tau,\nu) >_{L^2(\mathbb{R}^2)}$ $(m = 1,2,\ldots,N)$ on the main diagonal. Hence, the eigenvalues are just the values of the main diagonal, and, by Theorem 2.1.3, $u_p(t) = \arg\min_{s\in\mathcal{W}_N} \|F(\tau,\nu) - \chi_s(\tau,\nu)\|^2_{L^2(\mathbb{R}^2)}$.

Thus, according to Theorem 2.3.1, in the special case when the desired ambiguity surface is the surface of revolution, the solution of Problem 2.1.2 is one of the Hermite waveforms.

Note that up to this point the approximation of a given function by ambiguity functions was supposed to be done over the whole Euclidean plane. In what follows we generalize this problem to subregions of $\mathbb{R}^2$.

2.4 Approximation of an arbitrary square-integrable function by ambiguity functions over a subregion of $\mathbb{R}^2$

One of the main goals of a radar engineer is the design of waveforms with desired range-Doppler characteristics. It may be noticed that the preceding analysis described in subsections 2.1.1 and 2.1.3 shows that, in some theoretical sense, the problem can be regarded as solved. In more detail, if a candidate function $F(\tau, \nu)$ is an ambiguity function, it can be expanded using the orthonormal basis $\{\psi_{km}\}$ (see (2.3), (2.4)) to obtain the corresponding coefficients $\{a_m\}$ from formula (2.5). On the other hand, if a function $F(\tau, \nu)$ itself is not an ambiguity function, it can be approximated by some ambiguity function via the procedure described in subsection 2.1.3.

Note that the above approach is based on the assumption that the desired ambiguity shape is given in analytical form, which is not the case in any practical radar application. In practice, engineers have a general idea of acceptable shape rather than the formulas describing it, thus making Wilcox's algorithm not applicable. Moreover, in many situations, it is not even necessary to have a certain shape for all the values of time and Doppler delays (the region where the ambiguity surface is desired to be small depends on the particular radar application), and Wilcox's algorithm does not treat the situations where only part of the ambiguity surface has to be approximated. In what follows we make an attempt to extend Wilcox's classical results to the case of subregions of R^2.

In general form, the problem can therefore be phrased as follows:

PROBLEM 2.4.1 *For a given candidate function $F(\tau, \nu) \in L^2(\mathbb{R}^2)$, restricted to a*

specified region $G \subseteq \mathbb{R}^2$, find the waveform(s) $s(t) \in \mathcal{W}$ which corresponds to the projection (in the mean square sense) of $F(\tau,\nu)$ on $\mathcal{X}$.

The above, somewhat theoretical formulation, may be discretised in order to permit some practical needs. Accordingly, with this in mind, we reformulate Problem 2.4.1:

PROBLEM 2.4.2 *Assume that some orthonormal basis* (2.1) *and some region $G \subseteq \mathbb{R}^2$ are fixed. Then, given function $F(\tau,\nu) \in L^2(\mathbb{R}^2)$ and a positive integer N, find*

$$\begin{aligned}&\arg\min_{s\in\mathcal{W}_N} \|F(\tau,\nu)-\chi_s(\tau,\nu)\|^2_{L^2(G)}\\ &= \arg\min_{s\in\mathcal{W}_N}\Big(\|\chi_s(\tau,\nu)\|^2_{L^2(G)} - 2\Re\{< F(\tau,\nu),\chi_s(\tau,\nu) >_{L^2(G)}\}\Big) + \|F(\tau,\nu)\|^2_{L^2(G)}.\end{aligned} \tag{2.21}$$

Note that, in the special case of $G = \mathbb{R}^2$, the first and the last terms in (2.21) are both equal to 1, and thus have no effect on the minimization problem. Thus, the restriction of our attention to a suitably specified subset G of $\mathbb{R}^2$ (rather than to all of $\mathbb{R}^2$) results in the retention of certain terms which otherwise would cancel out if we considered all of $\mathbb{R}^2$, and thereby introduces additional parameters which can lead to substantial improvements of the design in the region under consideration.

We would like also to note that, due to Lemma 2.2.3, the norm to be minimized in (2.21) can be written as follows

$$\begin{aligned}&\arg\min_{s\in\mathcal{W}_N} \|F(\tau,\nu)-\chi_s(\tau,\nu)\|^2_{L^2(G)} = Q(a_0,a_1,\ldots,a_N)\\ &= \arg\min_{\{a_i\}\in\mathfrak{S}_N}\left(\sum_{i,k,m,n=0}^{N} c_{ikmn}a_i\overline{a}_k\overline{a}_m a_n - 2\Re\Big\{\sum_{k,m=0}^{N} b_{km}\overline{a}_k a_m\Big\}\right) + \|F(\tau,\nu)\|^2_{L^2(G)},\end{aligned} \tag{2.22}$$

where $c_{ikmn} =< \psi_{ik}(\tau,\nu),\psi_{mn}(\tau,\nu) >_{L^2(G)}$ and $b_{km} =< F(\tau,\nu),\ \psi_{km}(\tau,\nu) >_{L^2(G)}$. Thus, we conclude that to solve Problem 2.4.2 we have to *find* $a_m \in \mathfrak{S}_N\,(m = 0,1,\ldots,N)$ *minimizing the 4th order form* $Q(a_0,a_1,\ldots,a_N)$ defined by (2.22).

2.5 Approximation of ideal ambiguity function

It is well-known fact that an ideal radar waveform would produce a two-dimensional impulse function on the delay-Doppler plane. Such a function (we will denote it by $\chi_{opt}(\tau,\nu)$) would have ideal range-Doppler characteristics. However, since no finite energy signal gives rise to $\chi_{opt}(\tau,\nu)$ [8], we need to modify our notion of ideal ambiguity surface somehow in order to get realizable waveforms with some optimal properties. For many purposes it is desirable to construct a waveform producing a surface which vanishes everywhere in some (perhaps, quite large) neighborhood of the origin and has a (finite) peak at that point (we denote this surface by $\widetilde{\chi}_{opt}(\tau,\nu)$; clearly, $\widetilde{\chi}_{opt}(\tau,\nu)$ itself is an approximation to $\chi_{opt}(\tau,\nu)$). This observation gives rise to a question about finding an ambiguity surface $|\chi(\tau,\nu)|$ which provides the best approximation for $\widetilde{\chi}_{opt}(\tau,\nu)$ over some region G. In other words, the goal is to find $s(t)\in\mathcal{W}$ that minimizes $\|\widetilde{\chi}_{opt}(\tau,\nu)-|\chi_s(\tau,\nu)|\|^2_{L^2(G)}=\|\chi_s(\tau,\nu)\|^2_{L^2(G)}$ (i.e. a waveform that has best 'clear area' under its ambiguity surface squared over G). As can be noticed, this is just a special case of Problem 2.4.1. Referring to the finite-dimensional case (i.e. Problem 2.4.2), we arrive at the final formulation of the problem:

PROBLEM 2.5.1 *Find a waveform $s(t)\in\mathcal{W}_N$ with the smallest volume under $|\chi_s(\tau,\nu)|^2$ over some bounded connected region G, i.e.*

$$\arg\min_{s\in\mathcal{W}_N}\|\chi_s(\tau,\nu)\|^2_{L^2(G)}=\arg\min_{\{a_i\}\in\mathfrak{S}_N}\sum_{i,k,m,n=0}^{N}c_{ikmn}a_i\overline{a}_k\overline{a}_m a_n. \tag{2.23}$$

The mathematical formulation of Problems 2.4.1-2.5.1 for a general region $G\neq\mathbb{R}^2$ appears to be new in radar waveform design. Generally speaking, it is very difficult to find solution(s) of such a non-linear problem (the objective function in the above formulation is of the fourth order and it significantly depends on the choice

of region G as well as basis functions $\{\phi_m(t)\}$). In this section we consider a few examples illustrating the solutions to Problems 2.4.1-2.5.1 under the assumption that G is either disc or annulus and the basis functions $\{\phi_m(t)\}$ are Hermite waveforms (2.6).

2.5.1 Case 1: Approximation over a circular region

We start this subsection with the following theorem stating a very interesting new optimal property of Hermite waveforms:

THEOREM 2.5.1 *Let N be a fixed nonnegative integer and G be a circular region: $G = \{(\tau, \nu) : \tau^2+\nu^2 \leq R^2\}$. Let also $\psi_{iN} = \psi_{iN}(x_0)$ $(i = 0, 1, \ldots, N)$ be the sequence of functions defined by* (A.4) – (A.6)*. If radius R satisfies the set of inequalities*

$$\psi_{iN}(\pi R^2) - \psi_{NN}(\pi R^2) < 0, \tag{2.24}$$

then the family of waveforms

$$u_*(t) = e^{j\phi}u_N(t), \quad \phi \in \mathbb{R}$$

is a solution of Problem 2.5.1 among all the waveforms from $\mathcal{W}_N = \mathcal{W}_N(\{u_m(t)\}_{m=0}^N)$, where $\{u_m(t)\}_{m=0}^N$ is the sequence of Hermite waveforms (2.6)*.*

The proof of the theorem and analysis of conditions (2.24) are given in Appendix.

It follows from the above theorem that the ambiguity surface of the Nth Hermite waveform provides the best (among all the members of $\mathcal{W}_N$) approximation of the ideal ambiguity surface in the mean square sense over *any* circular region centered at the origin. Therefore, the larger N we will choose, the better approximation of the ideal shape we will obtain (this fact is illustrated in Figure 2.2).

As we noted in [15], the Hermite waveforms and their various optimal properties have been known in the radar community for a long period of time [19, 41], but have

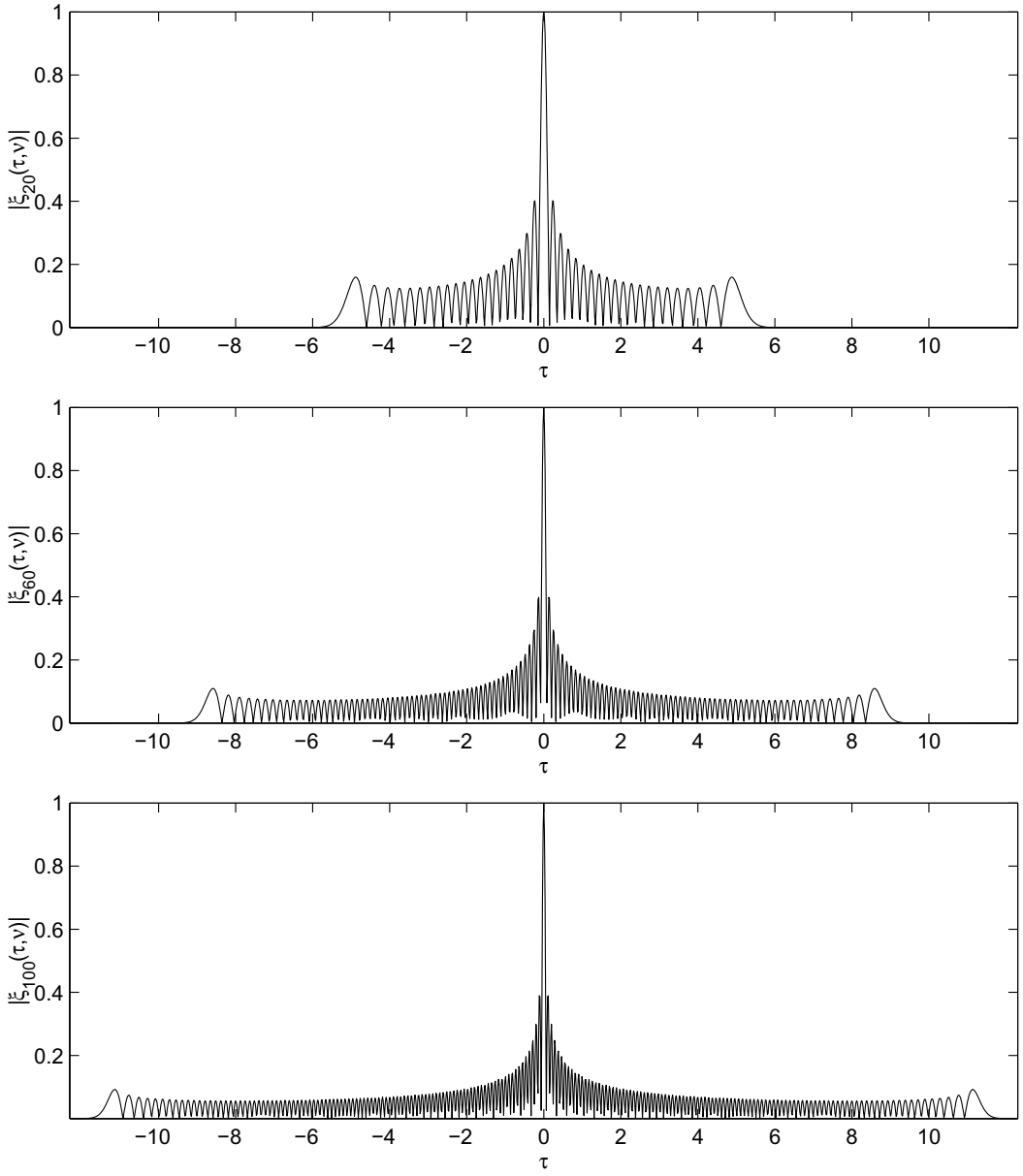

Figure 2.2: Arbitrary (passing through the origin) cross-section of the ambiguity surface $|\xi_{20}(\tau,\nu)|$ (top), $|\xi_{60}(\tau,\nu)|$ (middle), and $|\xi_{100}(\tau,\nu)|$ (bottom)

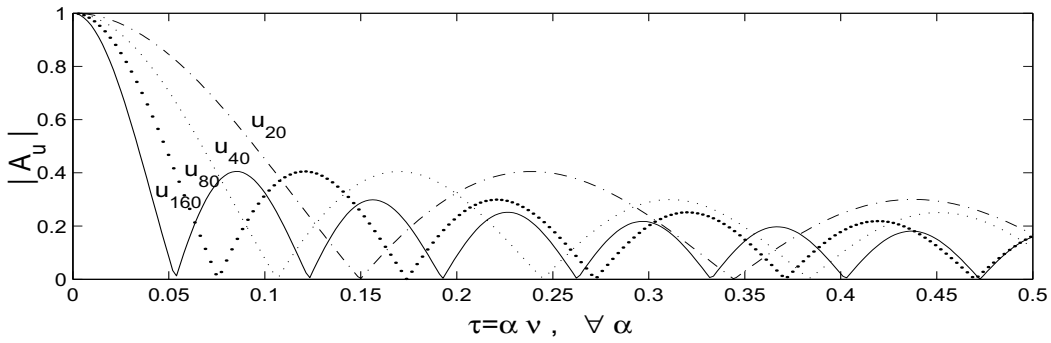

Figure 2.3: Sidelobe level of ambiguity surface for different Hermite waveforms

not been extensively used for practical needs of radar design. One of the reasons is that the few sidelobes (for each of the signal from this family) are relatively high and their level does not become lower with an increase of n. To illustrate this phenomenon, the cross-section of the ambiguity surface in the vicinity of the main lobe for four different Hermite waveforms is displayed in Figure 2.3. As it can be seen from the figure, when n increases, the kth sidelobe ($k = 1, 2, \ldots$) of the Hermite ambiguity surface approaches the origin, becomes more narrow, and, unfortunately, preserves the same height. This property holds for all Hermite waveforms, not only for those depicted in Figure 2.3, thus making the Hermite family of waveforms not suitable for most applications.

We should remark that the sidelobe problem is unfortunate but not surprising, since the optimization Problem 2.5.1 has been formulated in terms of minimal volume under the surface. Reformulation of Problem 2.5.1 in terms of the max-norm (or L_G^∞-norm) that would guarantee the lowest level of sidelobes in the selected region G is, obviously, one way to address the issue of high sidelobes, but in this case the problem becomes more complicated and remains open. However, as we show in the next subsection, the replacement of the selected region G, rather than norm (or basis functions), can lead to acceptable solutions. In more details, we consider the

minimization problem over a circular ring $G_r = \{(\tau, \nu) : r^2 \leq \tau^2 + \nu^2 \leq R^2\}$ and show that appropriate choice of the inner radius r enables us to find a solution of Problem 2.5.1 with low sidelobe level of its ambiguity shape not only over G_r, but for the whole G.

2.5.2 Case 2: Approximation over a disk

Below we consider a few numerical solutions of Problem 2.5.1 for the special case when the region G is the circular ring $G_r = \{(\tau, \nu) : r^2 \leq \tau^2 + \nu^2 \leq R^2\}$ surrounding the main lobe. The choice of radial dimensions of the ring is not arbitrary, it affects the solution of the non-linear optimization problem.

Note that property VI of the Hermite waveforms (see subsection 2.1.2) determines the lower bound on the interior radius r of the considered region G_r, since the Nth Hermite waveform provides the best approximation of the ideal main lobe in the class $\mathcal{W}_N$. Therefore, we choose r to be equal to the width r_N of the main lobe of $u_N(t)$, because the decrease of r does not lead to an improvement of the resolution parameters (the location of r_N can be estimated in terms of the bandwidth β_N or the timewidth τ_N of $u_N(t)$ [41]: $3\sqrt{3}/(16\beta_N\sqrt{2}) < r_N < \sqrt{3}/(2\pi\beta_N)$, where $\beta_N = \tau_N = \sqrt{(N+0.5)/(2\pi)}$). The choice of the exterior radius R is less obvious and affects the volume under the surface as well as the sidelobe distribution.

Sample solutions (see Figures 2.4 and 2.5) vividly illustrate the degree of control we can exert by suitably varying R. The top subplot of Figure 2.4 shows the waveform $s_1(t)$ obtained by means of a numerical solution of Problem 2.5.1 with $N = 199, R = 0.018$, while the bottom subplot of the figure displays the corresponding ambiguity function. Figure 2.5 demonstrates the solution $s_2(t)$ of the same problem with $N = 199, R = 0.05$ and its ambiguity surface. In both cases we achieve our goal of excellent ambiguity profiles in substantial neighborhoods of the origin. The size of

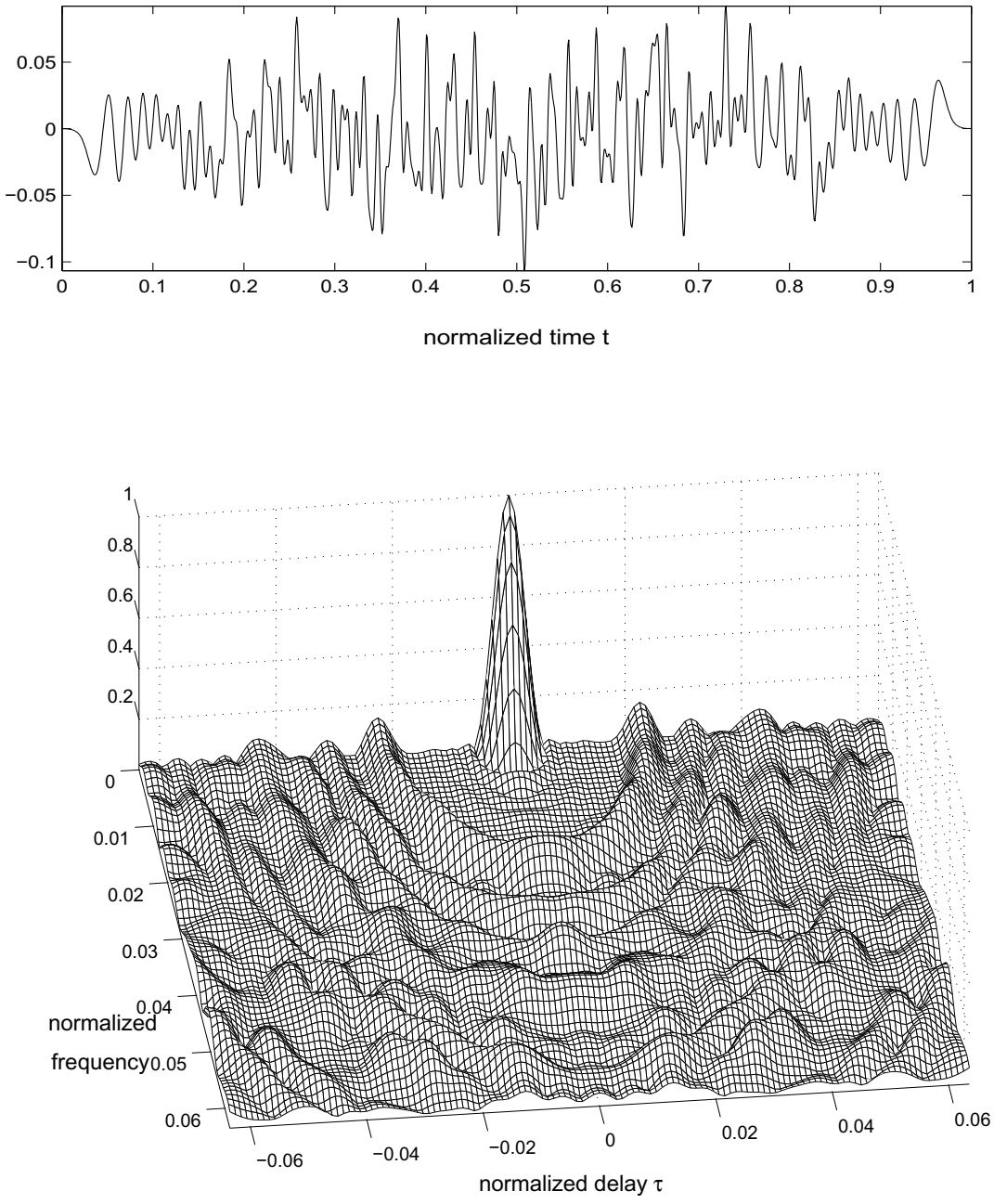

Figure 2.4: Numerical solution of Problem 2.5.1 with $N = 199, R = 0.018$.

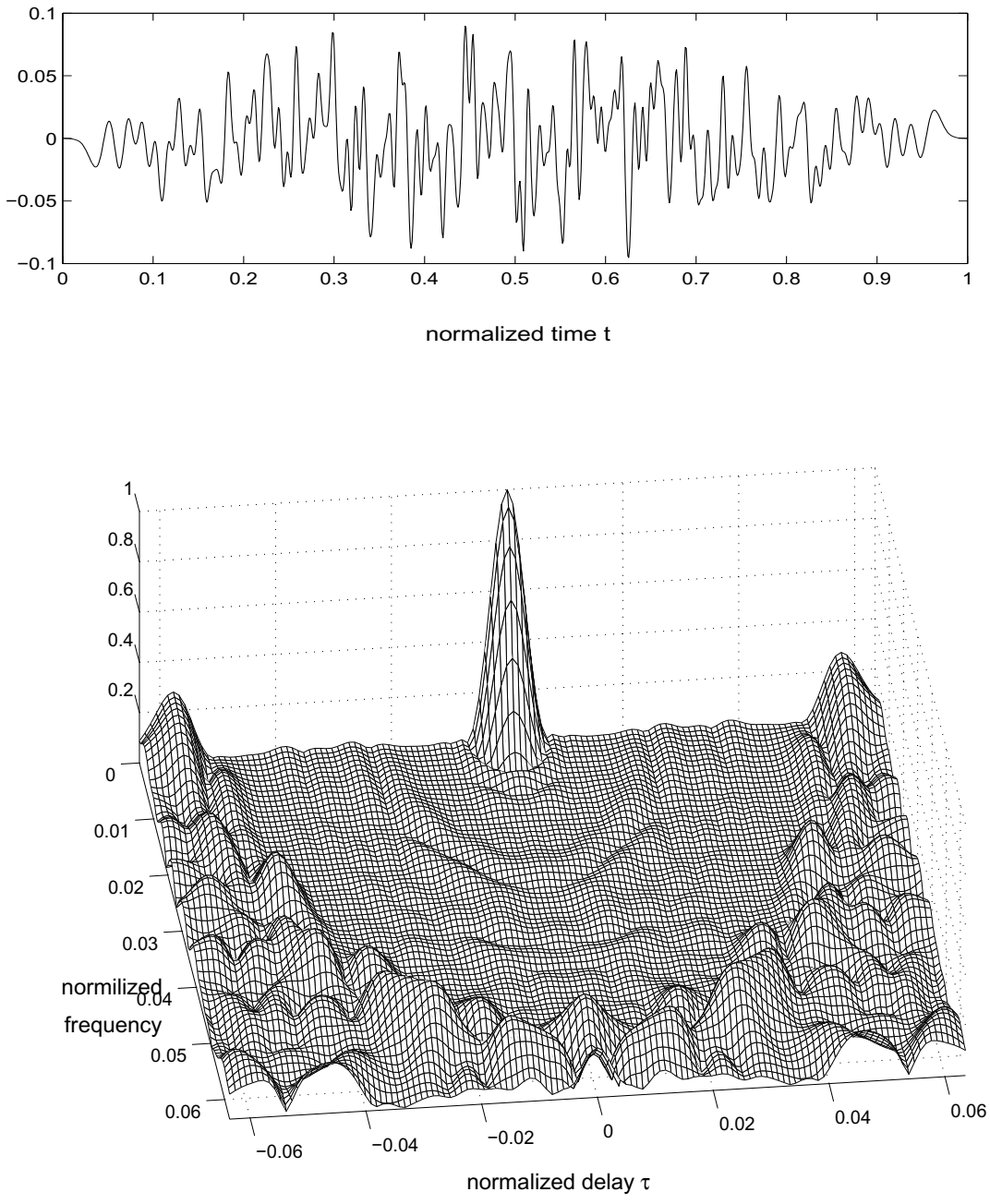

Figure 2.5: Numerical solution of Problem 2.5.1 with $N = 199, R = 0.05$.

the 'clear area' can be expressed by the ratio between R and the value of the smallest positive zero of $|\chi_s(\tau, 0)|$. It is approximately equal to 3.05 and 7.35 for waveforms $s_1(t)$ and $s_2(t)$, respectively. The height of the sidelobe peaks of $|\chi_{s_1}(\tau, \nu)|$ in the region of interest appears to be less than -35 dB (-30 dB for $|\chi_{s_2}(\tau, \nu)|$), whereas the nearest sidelobes outside G_r attain the level of -15 dB (-10 dB). In both cases the main lobe of the ambiguity surface becomes wider than the one for $|\chi_{u_{199}}(\tau, \nu)|$.

2.6 Summary

In his famous report [41], Wilcox introduced a general method for finding a waveform whose ambiguity function is a good approximation over all of $\mathbb{R}^2$ to a specified function. In this chapter, we have extended Wilcox's model of a radar waveform and adapted his method to the problem of producing a close match, over a specified subregion of $\mathbb{R}^2$, to a good ambiguity surface. The optimization over a subregion of $\mathbb{R}^2$ generalizes Wicox's approach, which optimizes over all of $\mathbb{R}^2$. There are new subtleties that appear with this approach, since we can seek, for example, to make an ambiguity small over some region, which, if successful, will push the bulk of the function outside the region where we want it to be small. Obviously, this is not possible if the region is all of $\mathbb{R}^2$, because of the volume property of the ambiguity function.

An obvious long range project is an investigation of the relationship between the choice of an orthonormal basis and the desired region $G \subseteq \mathbb{R}^2$. In this chapter, we have made an attempt to look at what happens with specific example of the orthonormal basis and region G. We have carried out such a project for Hermite waveforms and G having circular symmetry, which is a natural property for the G associated to an Hermite basis. In particular, we have found a new interesting

property of the Hermite waveforms: the Nth Hermite waveform provides the best (among the members of $\mathcal{W}_N$) approximation to the ideal ambiguity surface over any circular region.

We would like to note at the end of this chapter that the solution to the optimization problem $\arg\min_{s\in\mathcal{W}_N} \|\chi_s(\tau,\nu)\|^2_{L^2(G)}$ we have found here does not lead to finding a solution for the problem $\arg\min_{s\in\mathcal{W}} \|\chi_s(\tau,\nu)\|^2_{L^2(G)}$. However, it allows us to suggest an optimal waveform for any finite-dimensional subclass of $\mathcal{W}$ which makes this result important from practical point of view.

Chapter 3

Radar signals

3.1 Introduction

As it was already mentioned before, the aim of a radar engineer is to design waveforms with desired range-doppler characteristics. This problem is extremely complicated due to its nature and some practical limitations that should be taken into account.

First, we should note that the majority of radar signals are narrow bandpass signals (see [8, 22]). Their Fourier transform is limited to some frequency bandwidth centered about a carrier frequency ω_c. A narrow bandpass signal can be written in several forms (see [22] for details), one of which is $s(t) = Re\{u(t)e^{j\omega_c t}\}$ where $u(t)$ is a complex envelope of a real-valued signal $s(t)$. There is, however, a practical justification [22, 32] for dealing only with the complex envelope, $u(t)$, of the radar signal. The important fact that essentially restricts the possible signals under consideration should be taken into account: the radar signals are desired to be of a constant amplitude due to necessity to preserve the signal-to-noise ratio and some hardware limitations (recent paper [44] presents an attempt to start discussion

regarding implementation of signals having a nonconstant amplitude).

Second, it is important to keep in mind that the shape of desired ambiguity surface significantly depends on specific radar application. For some applications as well as for theoretical purposes, it is desirable to obtain "thumbtack" surface (see section 2.3). For other applications, the choice of the surface may be different. For example, there are circumstances [35] when a waveform which is extremely doppler tolerant (that is its ambiguity surface has a ridge along the doppler axis) is required. Sometimes, the desired ambiguity characteristics are based on some additional knowledge. For instance, no waveform is optimum for target resolution in general. Rather, there is an optimum waveform for each target environment; this is the waveform [32] achieving the desired nominal resolution with the least amount of self-clutter and target masking.

Third, once the shape of the desired ambiguity surface has been realized, one wishes to work backwards to find a corresponding waveform. This, however, is unsolved problem: no techniques are known for finding a waveform corresponding to a desired ambiguity surface, nor are a set of rules known for ensuring that a desired ambiguity surface is in fact an ambiguity surface; a waveform that gives rise to this desired surface might not exist. Moreover, as it was said at the end of the previous section, it is sometimes desirable to construct waveforms whose ambiguity surface has a predetermined shape over some subregion of $\mathbb{R}^2$. For example, if the range rate of targets is assumed to be known, one should concentrate on the ambiguity surface profile over a narrow stripe containing the time-delay axis. In this case, the shape of the magnitude of the autocorrelation function is of special importance.

At last, we remark that due to complexity of the ambiguity function there are only few classes of waveforms for which their ambiguity function is available in the closed form. However, many signals are too complicated, and only numerical

calculation of their ambiguity surface is feasible.

The above discussion implies that the design of a radar signal with desirable characteristics of the ambiguity function is based primarily on the radar designer's prior knowledge of radar waveforms and his/her expertise in such designs. Nadav Levanon, who is a world-known expert in the radar waveform design, writes in his recent book [22]: "... the work (or the art) of designing radar waveforms is based mostly on experience and expertise obtained through successive designs. This experience is gained by manipulating signal parameters while using special building blocks with desirable mathematical properties."

In this section we present a short overview of some known classes of radar waveforms.

3.2 Constant-frequency pulse

A constant-frequency (or unmodulated) pulse is a basic radar signal that can be found in any radar textbook. It is defined by

$$u(t) = \frac{1}{\sqrt{T}}\text{rect}\left(\frac{t}{T}\right) \tag{3.1}$$

where T is the pulse duration and $\text{rect}(t)$ is the rectangular pulse

$$\text{rect}(t) = \begin{cases} 1, & -\dfrac{1}{2} \le t \le \dfrac{1}{2}, \\ 0, & \text{otherwise.} \end{cases} \tag{3.2}$$

The ambiguity surface of unmodulated pulse (3.1) is represented [2, 8, 32, 22] by

$$|\chi_u(\tau,\nu)| = \left|\left(1-\frac{|\tau|}{T}\right)\text{sinc}\left[T\nu\left(1-\frac{|\tau|}{T}\right)\right]\right|, \quad |\tau| \le T, \qquad \text{zero elsewhere,}$$

where $\text{sinc}(x) = \sin(\pi x)/(\pi x)$, and is depicted in Figure 3.1. Since the ambiguity surface is symmetric with respect to the origin (see property **P.3** on page 6), only the half of the surface, corresponding to the positive Doppler-delays, is shown.

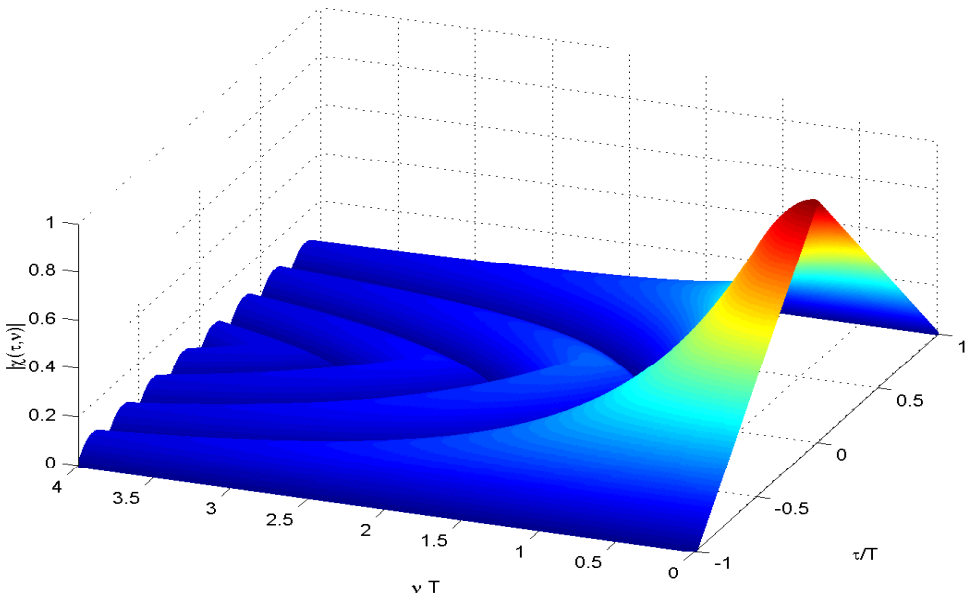

Figure 3.1: The ambiguity surface of constant-frequency pulse (3.1)

It can be seen from Figure 3.1 that $|\chi_u(\tau, \nu)|$ has a triangular zero-Doppler cut. The delay response reaches zero at the pulse width T. The zero-delay cut is $|\operatorname{sinc}(T\nu)|$. Hence, the first Doppler null is at the inverse of the pulse duration. Therefore, the delay resolution of pulse (3.1) is usually approximated by T, while the Doppler resolution – by $1/T$ (note that $T = 1/B$ where B is the signal's bandwidth).

It is well-known (see [8, 22, 27, 32, 35]) that the constant-frequency pulse exhibits poor performance in many aspects: poor range resolution, poor Doppler resolution and high Doppler sidelobes, and inefficient spectral use.

3.3 Pulse compression waveforms

Modern pulse radars generally use pulse compression waveforms whose autocorrelation function's profile produces something approximating "thumbtack".

The essence of pulse compression radar can be summarized as follows [32]: In a system utilizing the modulation signal or complex envelope for the measurement of

range, the sharpness of the matched-filter output signal is inversely proportional to the signal bandwidth. Hence, in order to compress the received signal into a narrow spike, the signal must have a large bandwidth. The problem is to provide this large bandwidth without degrading radar performance in other respects.

Pulse compression is achieved by modulating the transmit waveform in either phase or frequency to achieve a bandwidth significantly in excess of that of the envelope of the transmit pulse itself. The incorporation of pulse compression waveforms requires additional system complexity both in the radar transmitter for the proper encoding of the transmit pulse and, especially, in the radar receiver for compressing the received pulse. Despite this added complexity, many modern radars utilize some form of pulse compression due to the increased capability and flexibility it provides [5].

The range resolution achievable with a pulse compression system is given by $1/B$, where B is the bandwidth of the transmitted waveform. The product TB (here T is the time duration of the transmitted signal and is related to B by $B \gg 1/T$) is called the time-bandwidth product or pulse compression ratio of the system and is usually used [8, 30, 32] to characterize the degree of signal's compression. Note that the resolution attainable with pulse compression systems is a function of only bandwidth and not transmit pulse width, in contrast with simple pulse systems transmitting unmodulated pulses.

3.4 Phase-coded waveforms

One of the early methods for pulse compression is by phase coding that can be described as follows [8, 22, 32, 27]. Consider a pulse of duration T divided in time into N segments of identical duration such that each segment is assigned (or coded)

with a different phase value. The complex envelope of the phase-coded pulse is given by

$$u(t) = \frac{1}{T}\sum_{n=1}^{N} u_n \text{rect}\left[\frac{t-(n-1)t_b}{t_b}\right] \tag{3.3}$$

where $u_n = e^{j\phi_n}$, $t_b = T/N$, and the set of N phases $\{\phi_1, \phi_2, \ldots, \phi_N\}$ is the phase code associated with $u(t)$. For a binary coded waveform, it is fulfilled that $\phi_i \in \{0, 1\}\ \forall i$.

The number of possibilities of generating phase codes of length N is unlimited. The criteria [22] for selecting a specific code are the resolution properties of the resulting waveform, frequency spectrum, and the ease with which the system can be implemented. Sometimes the design is even more complicated by using different phase codes for the transmitted pulse and the reference pulse used at the receiver (possibly even with different lengths). This can improve resolution at the expense of a suboptimal signal-to-noise ratio.

The problem of finding a code with predetermined ambiguity surface is very complicated. A more manageable problem is to obtain a phase-coded waveform with a good autocorrelation function.

The most famous class of phase codes is named *Barker*, after its inventor [1]. They are precisely those binary phase codes that have autocorrelation sidelobes of magnitudes 1 and 0 only. Thus, the Barker codes are the biphase codes with minimum possible peak sidelobe levels and are sometimes referred to as perfect codes. All the known Barker codes can be found in [5, 22]. Although it was only proved that no binary codes exist for all odd $N > 13$ as well as all even $13 < N < 1898884$ (see [22] and references therein for details), it is common belief that no Barker codes exist for all $N > 13$. It should be noted here that these codes are only perfect in the time domain: the output degrades rapidly in the presence of Doppler shift. Papers [6, 7, 10] reported other examples of so-called minimum peak sidelobe

codes that do not meet the Barker condition.

Allowing any phase values in (3.3) can lead to lower sidelobes. However, the outermost sidelobe is always 1 (for any phase code). The polyphase sequence with minimal peak-to-sidelobe ratio excluding the outermost sidelobe are called generalized Barker sequence or polyphase Barker. Systematic methods to construct them were not yet found. Searches for generalized Barker sequences with no restriction on the values of the sequence phases have been carried out using numerical optimization techniques. Examples of such sequences were found for all $N \leq 45$ [3, 12, 13] and presented altogether in [22].

3.5 Linear frequency-modulated pulse

Linear frequency modulation (LFM or chirp) is the oldest and most developed of all the pulse compression techniques, having first been proposed in the late 1940's [8]. The LFM waveform consists of a rectangular (in amplitude) transmit pulse and a carrier frequency that is swept linearly (chirped) over the entire pulse length T, i.e. the complex envelope of the LFM pulse is given by

$$u(t) = \frac{1}{\sqrt{T}} \text{ rect} \left(\frac{t}{T} \right) e^{j\pi k t^2}, \qquad k = \pm \frac{B}{T}. \tag{3.4}$$

The ambiguity surface of chirp pulse (3.4) has the form [2, 8, 32, 22]

$$|\chi_u(\tau, \nu)| = \left| \left(1 - \frac{|\tau|}{T} \right) \text{sinc} \left[T(\nu - k\tau) \left(1 - \frac{|\tau|}{T} \right) \right] \right|, \quad |\tau| \leq T, \quad \text{zero elsewhere}, \tag{3.5}$$

and is depicted in Figure 3.2. As the figure shows, the improved delay resolution of LFM comes with a penalty of delay-Doppler coupling which is expressed by the diagonal ridge. The physical interpretation of this fact is that when $k > 0 (< 0)$, a target with positive Doppler appears closer (farther) than its true range. In many

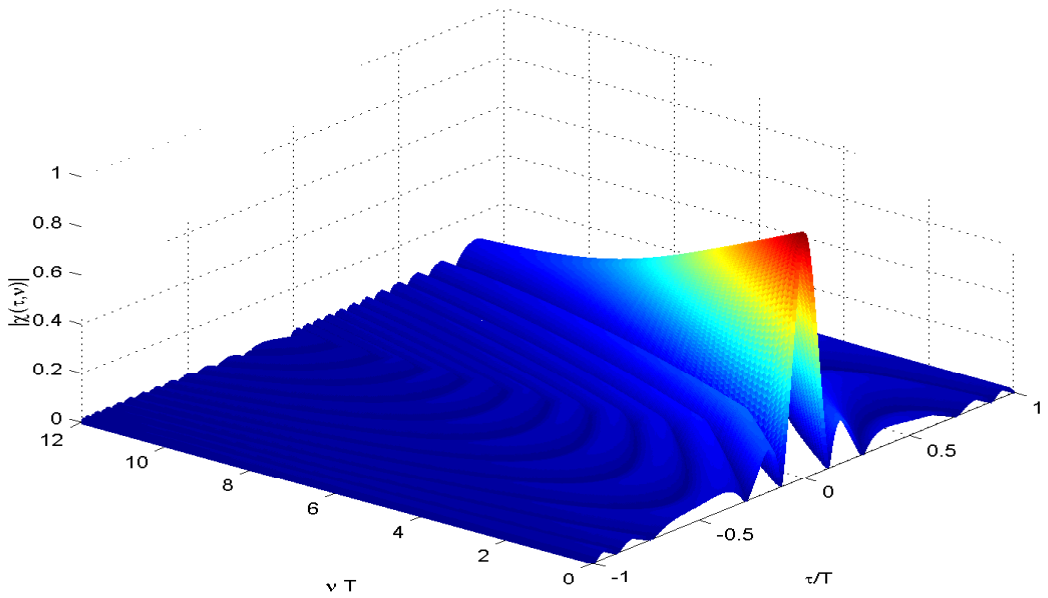

Figure 3.2: The ambiguity surface of LFM pulse (3.4) with $TB = 10$

applications the resulting range error is acceptable. The delay error of the shifted peak response is accompanied by a small decrease in the height of the peak.

Adding linear frequency modulation to the constant-frequency pulse increases the bandwidth and thus improves the range resolution of the chirp by a factor equal to the time-bandwidth product. However, relatively strong sidelobes remain in the autocorrelation function (ACF) of LFM pulse, as seen in Figure 3.3. These sidelobes can be reduced by signal spectrum reshaping that can be done using weighting (see [21] and references therein).

Knowledge of the weighting windows mentioned above may be used to obtain noolinear frequency modulated waveforms with good range resolution properties. Such waveforms are generally derived so that the spectral amplitude weightings used for sidelobe suppression in the LFM receiver are approximated by a nonlinear time frequency distribution characteristic that is shared by both the transmitted waveform and the receiver [5]. That is, these waveforms are usually invented by

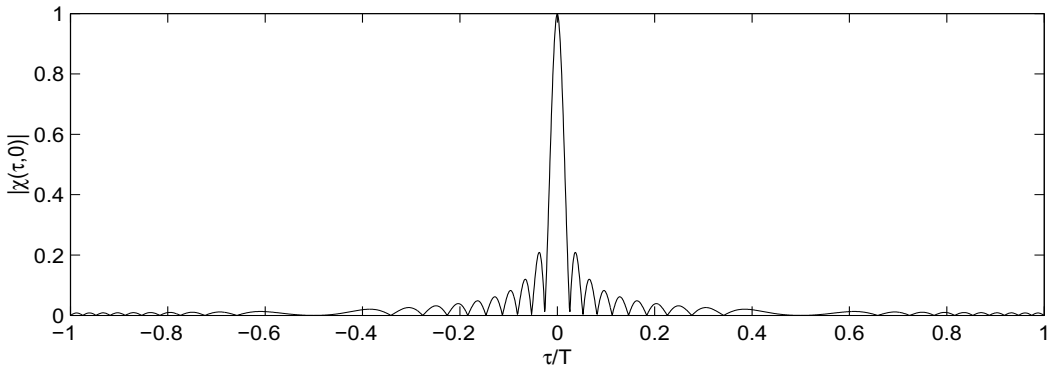

Figure 3.3: The magnitude of autocorrelation function of LFM pulse (3.4) with $TB = 40$

deriving a frequency-time distribution whose square equals the product of a linear FM waveform with a chosen sidelobe reduction weighting function. Examples of such nonlinear FM waveforms are presented in [5, 22].

3.6 Pulse trains

Long duration signals can be generated by periodically repeating a suitable short-duration pulse. A pulse train, then, is a waveform consisting of a finite or infinite number of nonoverlapping pulses. Pulse repetition is convenient method of increasing the signal duration without a proportionate decrease in the bandwidth. In addition, the bandwidth can be increased by shifting the carrier frequency from one pulse to the next. With pulse trains, it thus is possible to design signals of extreme complexity [22, 32] and yet leave the associated equipment relatively manageable.

There are many ways to construct pulse trains. A uniformly spaced pulse train $p(t) = \sum_{n=0}^{N-1} s(t - nT_r)$ provides a simplest example of a train constructed from a pulse $s(t)$ (here T_r is the pulse repetition interval and $s(t)$ is assumed to have a width smaller than T_r). Other basic ways to create the diversity of trains are based [2] on

introducing of

- an irregular spacing of the pulses: $p(t) = \sum_{n=0}^{N-1} s\left(t - \sum_{m=0}^{n} T_m\right)$, where T_m is the mth pulse spacing;
- an irregular pattern of phase shifts of the pulses: $p(t) = \sum_{n=0}^{N-1} s(t - nT_r)e^{-j\theta_n}$, where θ_n is the phase angle of the nth pulse;
- an irregular pattern of frequency shifts of the pulses: $p(t) = \sum_{n=0}^{N-1} s(t-nT_r)e^{-j2\pi f_n t}$, where f_n is the frequency shift of the nth pulse.

The following theorem relates the ambiguity function of a uniform pulse train to the ambiguity function of a single pulse constituting the train.

THEOREM 3.6.1 *(AF of a uniform pulse train) [2]. Let $s_1(t)$ be a pulse of duration T centered at time zero and*

$$p_1(t) = \sum_{n=0}^{N-1} s_1\left(t - nT_r + \frac{1}{2}(N-1)T_r\right) \tag{3.6}$$

be the pulse train centered at time zero as well, where the PRI $T_r > T$. Then

$$\chi_{p_1}(\tau,\nu) = \sum_{n=-(N-1)}^{N-1} \chi_{s_1}(\tau - nT_r, \nu)\frac{\sin\left[\pi\nu T_r(N-|n|)\right]}{\sin \pi\nu T_r}. \tag{3.7}$$

Applying the approaches mentioned above, one can generate the variety of trains. Some of them were extensively studied (see [8, 22, 32] and references therein). We would like to mention here the famous Costas coding, which results in a rather randomlike frequency evolution. Costas [9] showed how a special class of permutation matrices [17] may be beneficially used to determine the frequency-time pattern of a uniform pulse train. Proper choice of burst waveform parameters was shown to result in detection waveform having range and Doppler resolution properties consistent with the overall signal duration and bandwidth. The range-Doppler sidelobe

peaks was shown to be well-controlled so that the "thumbtack" ambiguity function behaviour is closely approximated by the synthesis procedure presented. Below we discuss other example of pulse trains obtained by frequency shifts of neighbor pulses.

3.7 Stepped-frequency pulse train

As we have already mentioned before, modern radars commonly use wide bandwidth pulses to attain high range resolution. However, when such wideband pulses are unavailable due to hardware limitations, high range resolution can still be achieved by coherently combining a sequence of narrowband pulses spanning the desired bandwidth. Collectively, such narrowband pulse sequences are said [22, 29, 39] to compose a "synthetic wideband waveform". Below we will consider a specific variant of such a waveform known as stepped-frequency waveform.

Radars that use stepped-frequency waveforms do not require costly wideband hardware. Instead, high range resolution is attained by transmitting a sequence of narrowband pulses (called a "burst"). The center frequency of each pulse is adjusted so that the aggregate burst covers a relatively wide bandwidth. Frequency steps that allow to adjust the center frequencies of the component pulses can be added to a train of unmodulated as well as to a train of modulated (e.g., LFM) pulses.

If the time gaps between subpulses are small, the entire waveform is transmitted prior to turning on the receiver. Then, the convolutional processing is applied to the full waveform. When the product of the frequency step times the pulse duration is larger than one, the autocorrelation function of the stepped-frequency pulse train suffers from ambiguous peaks, known as "grating lobes". It is also known that replacing the fixed-frequency pulses with LFM pulses can reduce those grating lobes. In this section we review different approaches for the grating lobes suppression in a

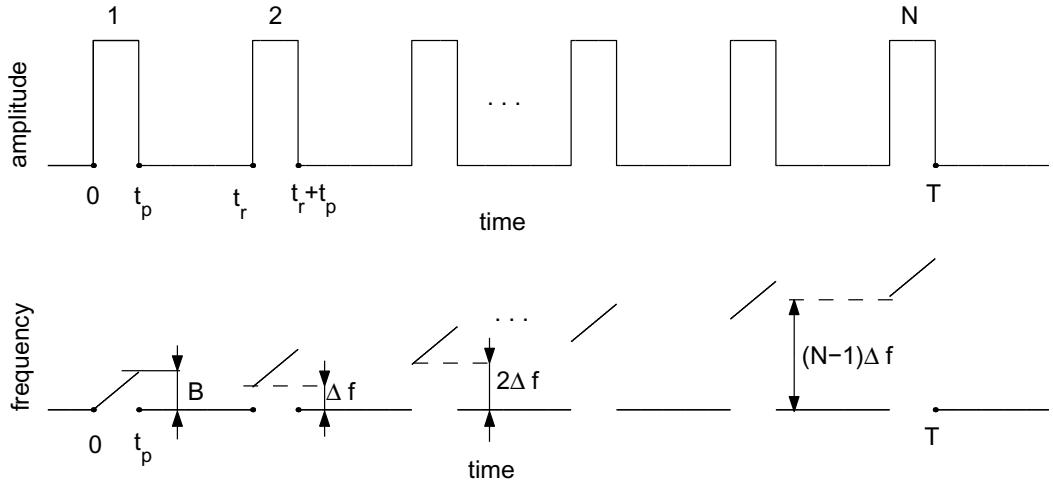

Figure 3.4: Time-energy (top) and time-frequency (bottom) distributions of uniform LFM pulse train $u(t)$ with constant frequency step $\triangle f$

stepped-frequency train of LFM pulses.

Traditional stepped-frequency train of N LFM pulses $s_p(t)$ (see (3.4)), each of duration t_p, has a constant frequency step between consecutive pulses and can be defined [21, 22] as follows (see also Figure 3.4):

$$\begin{aligned} u(t) &= \frac{1}{\sqrt{N}}\, e^{j\pi \frac{\Delta f}{t_r} t^2} \sum_{n=0}^{N-1} s_p(t - nt_r) \\ &= \frac{1}{\sqrt{Nt_p}}\, e^{j\pi \frac{\Delta f}{t_r} t^2} \sum_{n=0}^{N-1} \mathrm{rect}\left(\frac{t - nt_r}{t_p}\right) e^{j\pi(\frac{B}{t_p} - \frac{\Delta f}{t_r})(t-nt_r)^2}, \end{aligned} \tag{3.8}$$

where $t_r > 2t_p$ is the pulse repetition interval, $B(> 0)$ is the radar ultimate bandwidth, $\Delta f(\geq 0)$ is the constant frequency step.

It is shown in [21] that, for $|\tau| \leq t_p$, the magnitude of the autocorrelation function of train (3.8) has the form

$$|R(\tau)| = \left|\left(1 - \frac{|\tau|}{t_p}\right) \mathrm{sinc}\left[B\tau\left(1 - \frac{|\tau|}{t_p}\right)\right]\right| \left|\frac{\sin(N\pi\tau\triangle f)}{N\sin(\pi\tau\triangle f)}\right|. \tag{3.9}$$

As follows from (3.9), the autocorrelation function of the stepped-frequency train $u(t)$ is the two-term product. The first factor here is the autocorrelation function of

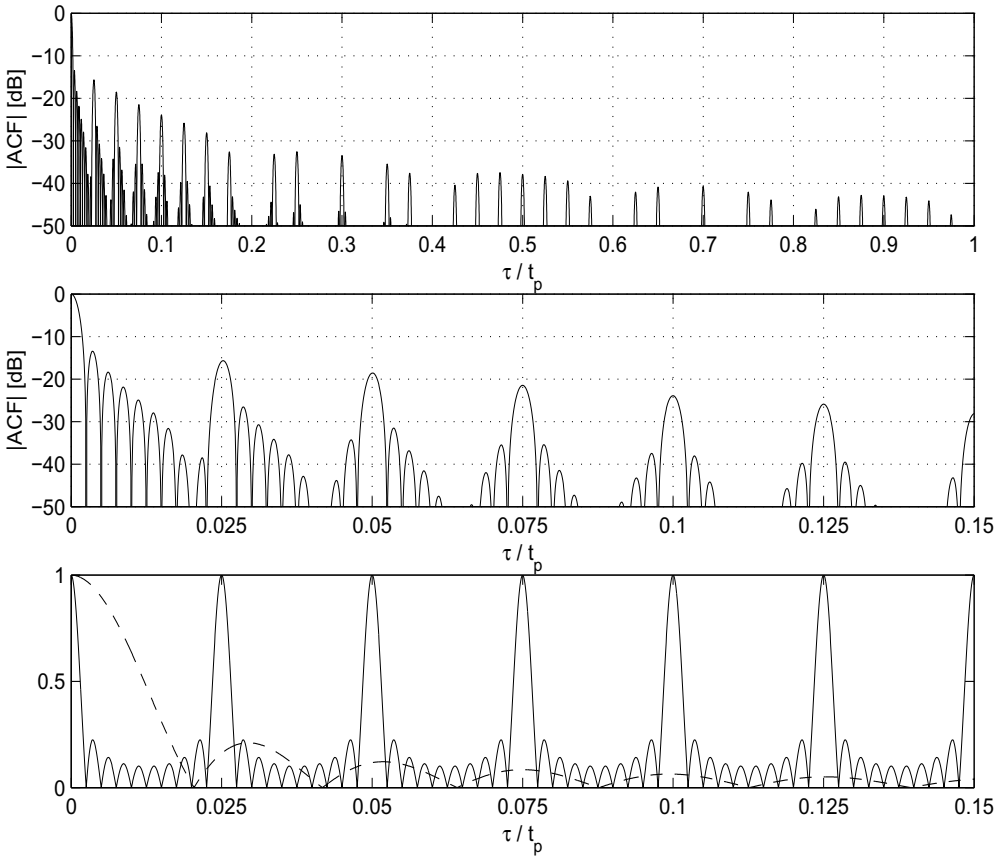

Figure 3.5: Stepped-frequency train of LFM pulses with $N = 10, t_p\Delta f = 40$, and $Bt_p = 50$. Top and Middle: Partial auto-correlation function. Bottom: the first term (dashed line) and the second term (solid line) in (3.9).

any single subpulse in (3.8), while the second factor is a periodic sinc function due to the pulse train. The second term causes the appearance of the grating lobes at the points of its maxima, i.e. at $\tau_n = n/\Delta f$, where $n = \pm 1, \pm 2, \ldots, \pm\lfloor t_p\Delta f \rfloor$. Figure 3.5 shows the magnitude of the autocorrelation function of a typical stepped-frequency LFM train in the vicinity of the origin. It is clear that high spikes appearing at time delays 0.025, 0.05, 0.075, 0.1, and 0.125 essentially reduce waveform's resolution capabilities.

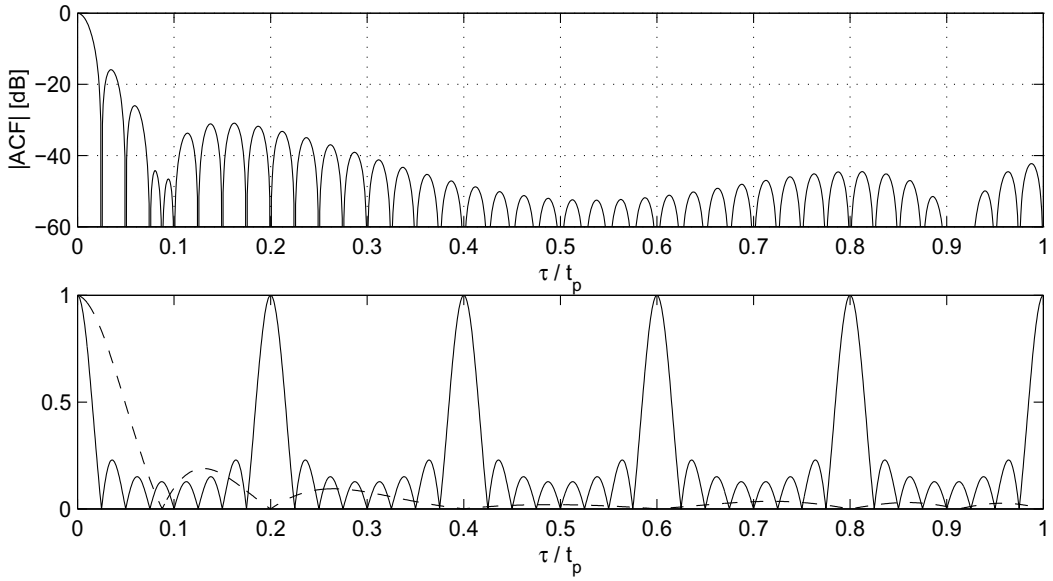

Figure 3.6: Stepped-frequency train of LFM pulses with nullified grating lobes ($N = 8, t_p\Delta f = 5$, and $Bt_p = 12.5$). Top: Partial auto-correlation function. Bottom: the first term (dashed line) and the second term (solid line) in (3.9).

Methods to lower grating lobes in stepped-frequency LFM trains were recently discussed [16, 21, 23]. The case, when $B = \Delta f$, was studied in [23]. It was shown that when all subpulses have equal bandwidth and time duration, the compressed pulse is very similar to an LFM pulse with the composite bandwidth, except for grating lobes at multiples of the subpulse-to-subpulse frequency jump. The maximum grating lobe is about -24 dB, which is too high for many applications. It was also proposed to reduce the grating lobes by varying the width of subpulses, thus destroying periodicity. It was shown that, in a resulting nonperiodic train, the grating lobes can be reduced by a factor which is approximately equal to N.

Publications [16, 21] have studied stepped-frequency trains with overlapped subpulse spectra. It was shown in [21] that a suitable choice of parameters at hand (i.e., $B, \triangle f$, and t_p) allows one to nullify several (or, sometimes, even all) grating lobes of an LFM pulse train (Figure 3.6 illustrates the autocorrelation function with nul-

lified grating lobes produced by one of the waveforms found in [21]). The paper contains analytical description for a discrete set of waveform parameters that provide nullifying of the grating lobes. One of the conclusions that can be drawn from the relationship between t_pB and $t_p\Delta f$ obtained in [21] is that the overlap ratio $B/\Delta f$ is large for large values of t_pB. Therefore, in order to increase the bandwidth significantly (under the restriction that the first two grating lobes are nullified), the number of pulses N has to be large.

Paper [16] suggested a modified method for suppressing grating lobes in stepped-frequency pulse trains. To achieve a desired level of grating lobe suppression it was required that the values of the first term in (3.9) at the points τ_n would be less than some small value ϵ chosen a priori. Such modification of the grating lobes suppression problem leads to a significantly different relationship between t_pB and $t_p\Delta f$ which allows one to find waveforms with large t_pB, small ratio $B/\Delta f$, and small (rather then zero) grating lobes. A pictorial representation for the set of acceptable parameters corresponding to the case $N = 10$ and $\epsilon = 0.01$ (producing grating lobe level $\leq$ -40 dB) is given in Figure 3.7.

We would like to note that both approaches mentioned above have been designed to control the values of $|R_u(\tau)|$ in the close vicinity of the points $\tau_n (n = 1, 2, \ldots, \lfloor t_p\Delta f \rfloor)$. Clearly, this cannot guarantee the achievement of a desired level of sidelobe suppression even for time delays $\tau \geq \tau_1$. Figure 3.8 illustrates this observation. The autocorrelation function depicted in the figure is produced by the waveform having parameters ($N = 10, t_p\Delta f = 100$, and $Bt_p = 1018$) belonging to a shaded region in Figure 3.7. Despite of the fact that $|R_u(\tau_n)| < 0.01$ (for instance, the values of $|R_u(\tau)|$ at the points $\tau_1 = 0.01, \tau_2 = 0.02$, and $\tau_3 = 0.03$ are equal to 0.0076, 0.0023, and 0.0096, respectively), the autocorrelation profile contains a few relatively high spikes. Five of them, denoted by $s_2, s_3, \ldots, s_6$, appear near the

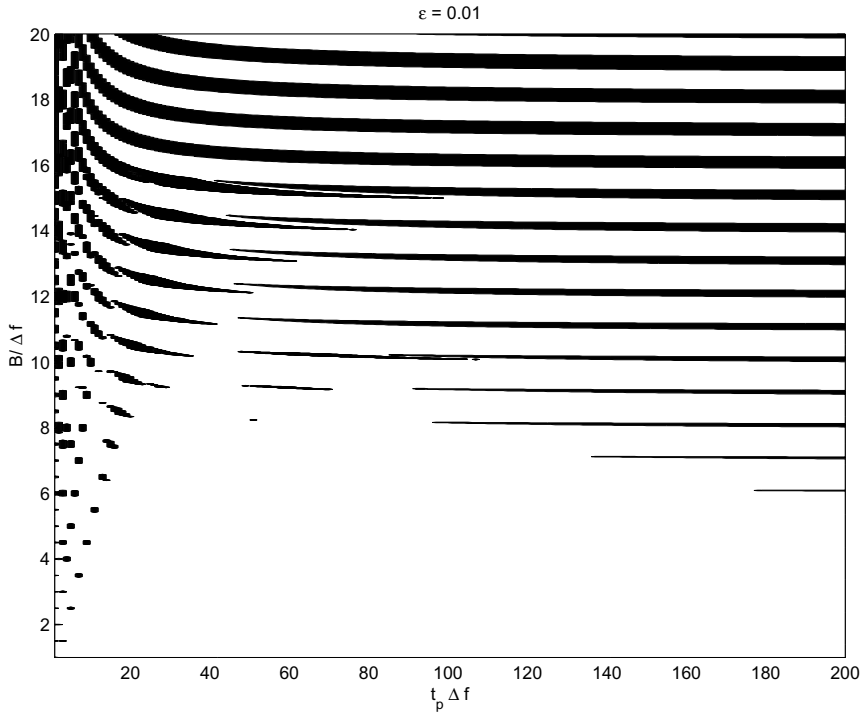

Figure 3.7: Shaded regions represent all possible values of $(t_p\Delta f, B/\Delta f) \in [1, 200] \times [1, 20]$ leading to the grating lobes suppression below -40 dB level.

points τ_1, τ_2, and τ_3, and attain the level of -33.5dB, -32.3dB, -38.3dB, -39.8dB, and -39.8dB, respectively.

The presence of high near-source sidelobes is another feature that degrades the performance of stepped-frequency waveform (3.8). This issue is illustrated in Figures 3.5 and 3.8 (for example, the height of the first, counting from the main lobe, and highest sidelobe s_1 in Figure 3.8 is -26.27dB). It is known that, within the chosen construction of the stepped-frequency waveform with constant time duration t_p, constant bandwidth B, and constant step Δf, it is usually impossible to suppress these few sidelobes.

The usage of variable frequency steps between consecutive subpulses is one of the known ways to effectively reduce all the time sidelobes. (It should be noted at this point that staggering of the frequency steps merely implies reshaping the wave-

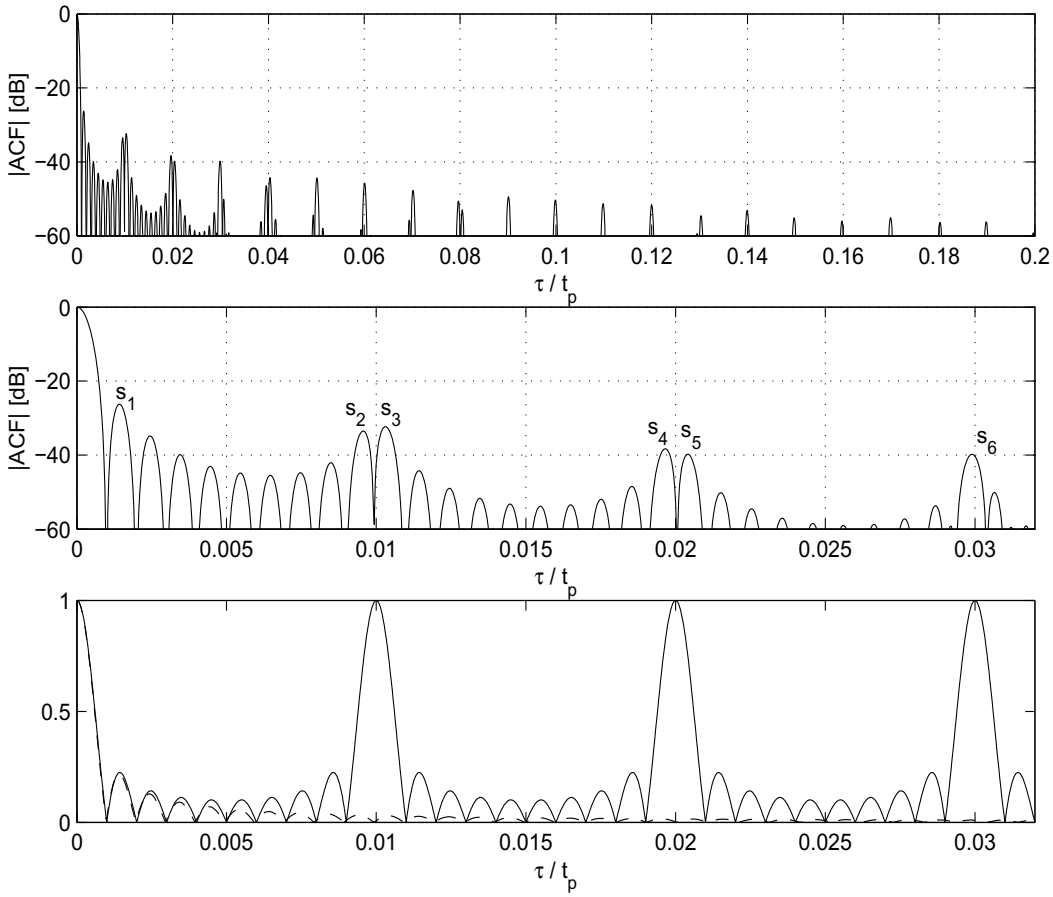

Figure 3.8: Stepped-frequency train of LFM pulses with $N = 10, t_p\Delta f = 100$, and $Bt_p = 1018$. Top and Middle: Partial auto-correlation function. Bottom: the first term (dashed line) and the second term (solid line) in (3.9).

from's spectrum, thus introducing the frequency weighting.) In his recent paper [29], Rabideau has described a numerical algorithm for designing synthetic wide-band waveforms whose spectrum would approximate one of the known weighting functions. It can be done by means of an appropriate choice of nonlinear frequency stepping. The number of pulses constituting the waveform controls the quality of such an approximation. Below we suggest other technique for choosing variable frequency steps in stepped-frequency waveform that leads to overall sidelobe suppression.

Chapter 4

Sidelobe suppression in the stepped-frequency train of LFM pulses

In this chapter we propose a new systematic approach for designing stepped-frequency LFM pulse trains producing the ACF whose peaks are lowered below some predetermined level. It is based on the usage of variable frequency steps that are introduced by means of specific relationships between the positions of the center frequencies of the pulses. Our approach (which is analytical rather than numerical) advantages from the fact that the ACF of the resulting waveform is available in the closed form. This gives us possibility to search for waveforms with a desired threshold level by analyzing the set of their parameter values. Suitable selection of the parameters allows us to design a variety of LFM trains with excellent ACF profiles.

4.1 Waveform Definition

In this section we define a family of compound waveforms that will be subject to study throughout this chapter.

We begin with a "simple" chirp pulse of unit energy

$$s_p(t) = \frac{1}{\sqrt{t_p}}\text{rect}\left(\frac{t - t_p/2}{t_p}\right) e^{j\pi k_p t^2}, \tag{4.1}$$

where t_p is the pulse duration, $j^2 = -1$, k_p is the frequency slope which we assume to be positive ($k_p > 0$), and rect(t) is the well-known rectangular pulse given by (3.2).

Next, we form a uniform train of N pulses (4.1):

$$s_N(t) = \frac{1}{\sqrt{N}} \sum_{n=0}^{N-1} s_p(t - nt_r). \tag{4.2}$$

Here t_r is the pulse repetition interval (PRI) which is assumed to be chosen such that the duty cycle is greater than 2, i.e.

$$t_r > 2t_p. \tag{4.3}$$

Note that the first factor in (4.2) is added to maintain the unit energy of $s_N(t)$. The amplitude and frequency of $s_N(t)$ are schematically depicted in Figure 4.1. As can be seen from the figure, the train $s_N(t)$ occupies the same frequency band as $s_p(t)$, namely,

$$B_p = k_p t_p (\geq 0). \tag{4.4}$$

The total time duration of $s_N(t)$ is $T_p = (N-1)t_r + t_p$.

Now we add an LFM with the frequency slope k_N ($k_N > 0, k_N \neq k_p$) to the entire train (4.2):

$$u_p(t) = s_N(t)e^{j\pi k_N t^2} = \frac{1}{\sqrt{N}} e^{j\pi k_N t^2} \sum_{n=0}^{N-1} s_p(t - nt_r). \tag{4.5}$$

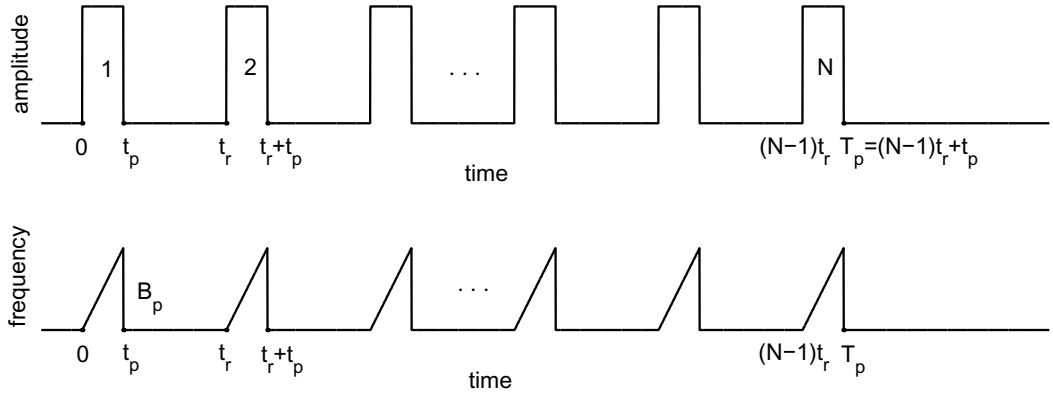

Figure 4.1: Uniform train of N LFM pulses.

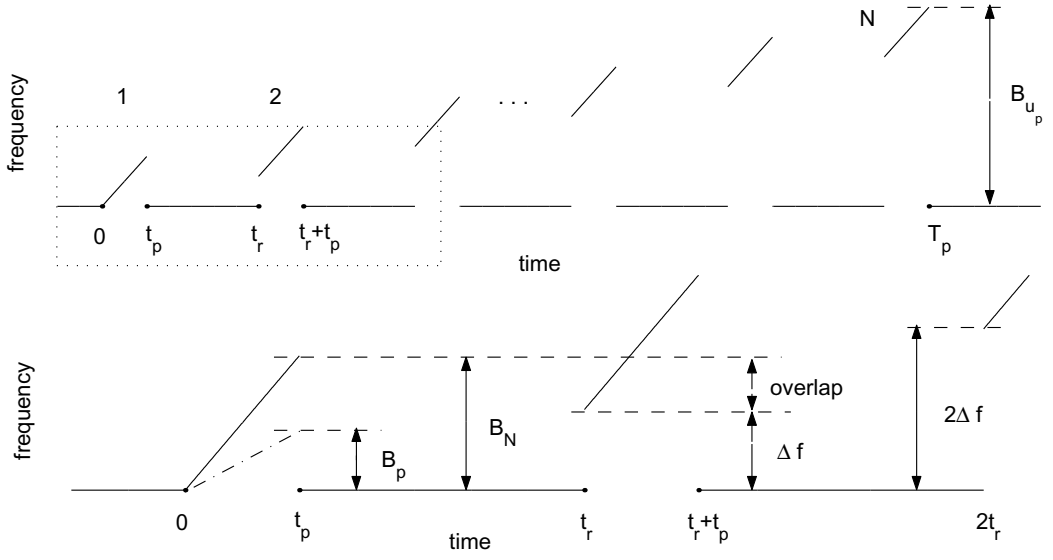

Figure 4.2: Top: Frequency evolution of stepped-frequency LFM pulse train $u_p(t)$. Bottom: zoom on dotted region of the top subplot.

Such an addition changes the instantaneous bandwidth of each component in train (4.2) (see Figure 4.2). We will denote the bandwidth of each subpulse, $\widetilde{s}_n(t) = e^{j\pi k_N t^2} s_p(t - nt_r)$, in train (4.5) by B_N, that is

$$B_N = B_p + k_N t_p = (k_p + k_N)t_p > 0. \tag{4.6}$$

(Note that B_N is not the ultimate bandwidth of any single pulse presented in (4.5).) Moreover, adding an LFM in (4.5) creates a constant frequency step

$$\Delta f = k_N t_r > 0 \tag{4.7}$$

between the center frequencies of the consecutive subpulses in the train $u_p(t)$ (see Figure 4.2). This leads to the essential broadening of the waveform's total bandwidth which becomes equal to

$$B_{u_p} = B_N + (N-1)\Delta f. \tag{4.8}$$

We suppose that there will be either the uniform energy distribution over the frequency band B_{u_p} (i.e., $\Delta f = B_N$) or some frequency overlap, shown in Figure 4.2, between neighbor components of $u_p(t)$ (i.e., $\Delta f < B_N$). In the latter case, the spectrum of $u_p(t)$ will be reshaped, that is it will be different from the rectangular shape. We also remark that the total duration of $u_p(t)$ is T_p.

Next, we apply the two-step design procedure described above to the waveform $u_p(t)$. This allows us to further increase the resulting waveform's bandwidth and reshape its spectrum. In more details, we use the waveform $u_p(t)$ as a single component to create a uniform train of M subpulses (as depicted in Figure 4.3)

$$\begin{aligned} u_M(t) &= \frac{1}{\sqrt{M}} \sum_{m=0}^{M-1} u_p(t - mT_r) = \frac{1}{\sqrt{M}} \sum_{m=0}^{M-1} s_N(t - mT_r) e^{j\pi k_N (t-mT_r)^2} \\ &= \frac{1}{\sqrt{MN}} \sum_{m=0}^{M-1} e^{j\pi k_N (t-mT_r)^2} \sum_{n=0}^{N-1} s_p(t - nt_r - mT_r) \end{aligned} \tag{4.9}$$

with the pulse repetition interval $T_r > 2T_p$.

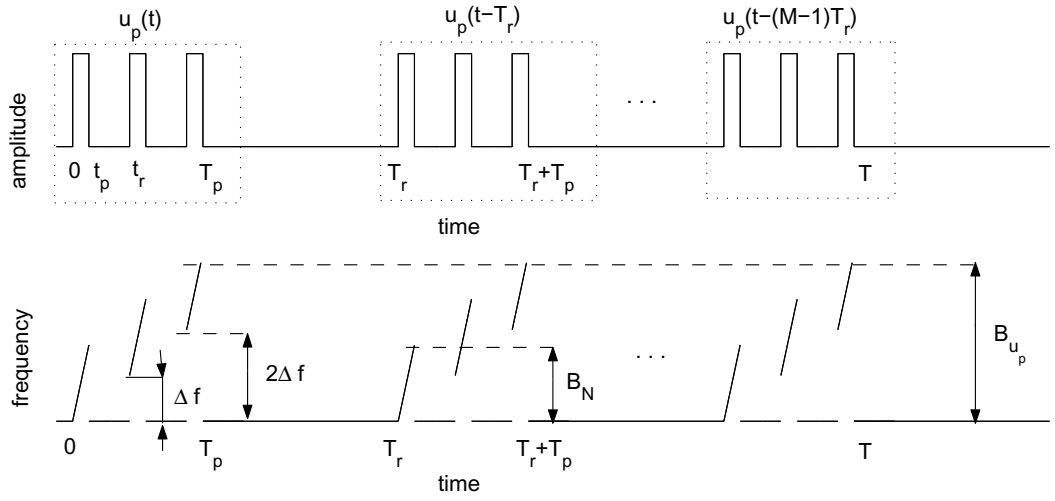

Figure 4.3: Non-uniform stepped-frequency pulse train $u_M(t)$

Finally, we add a new LFM with the frequency slope k_M ($k_M > 0, k_M \neq k_N + k_p$) to the entire train (4.9) (see Figure 4.4):

$$\begin{aligned} u(t) = u_M(t)e^{j\pi k_M t^2} &= \frac{1}{\sqrt{M}} e^{j\pi k_M t^2} \sum_{m=0}^{M-1} u_p(t - mT_r) \\ &= \frac{1}{\sqrt{M}} e^{j\pi k_M t^2} \sum_{m=0}^{M-1} s_N(t - mT_r) e^{j\pi k_N (t-mT_r)^2} \\ &= \frac{1}{\sqrt{MN}} e^{j\pi k_M t^2} \sum_{m=0}^{M-1} e^{j\pi k_N (t-mT_r)^2} \sum_{n=0}^{N-1} s_p(t - nt_r - mT_r). \end{aligned} \tag{4.10}$$

As the result, we obtain a non-uniform train of NM pulses that can be divided into M portions $u^{(1)}(t)$, $u^{(2)}(t), \ldots, u^{(M)}(t)$, where

$$u_i(t) = \frac{1}{\sqrt{M}} e^{j\pi k_M t^2} u_p(t-(i-1)T_r), \quad t \in [(i-1)T_r, (i-1)T_r + T_p], \quad i = 1, 2, \ldots, M. \tag{4.11}$$

Each such a portion $u^{(i)}(t)$ of the "outer" train $u(t)$ is an "inner" uniform stepped-frequency train of N pulses, each of duration t_p, with the ultimate bandwidth B which is equal, due to (4.6), (4.10), to

$$B = B_N + k_M t_P = (k_p + k_N + k_M) t_p > 0. \tag{4.12}$$

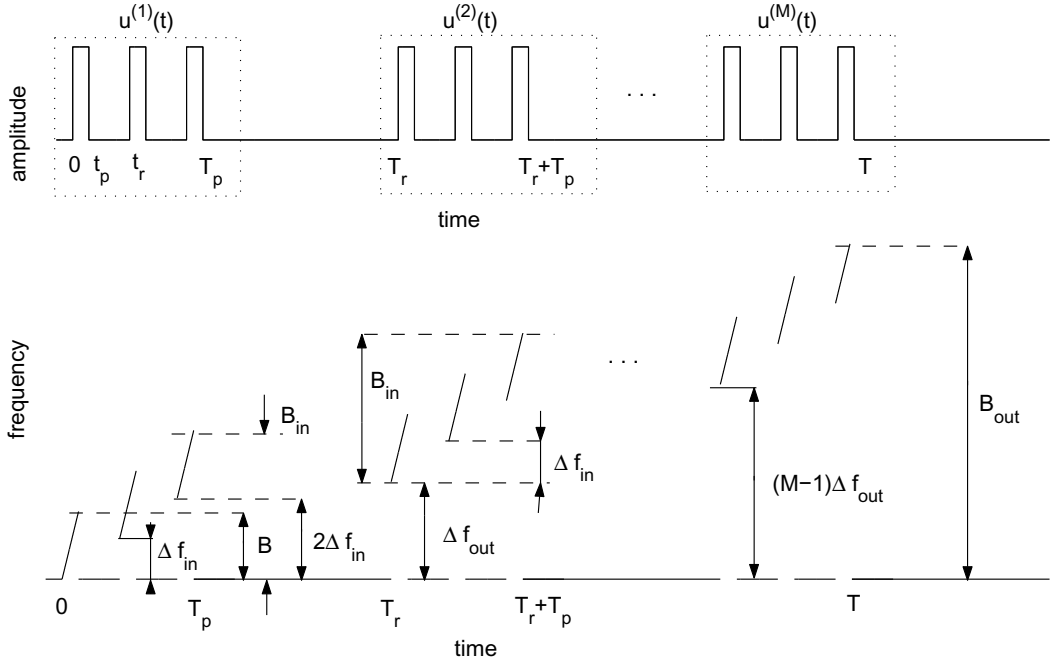

Figure 4.4: Time-energy (top) and time-frequency (bottom) distributions of the LFM pulse train $u(t)$ with nonuniform repetition intervals and variable frequency steps.

After adding the LFM in (4.10), the "inner" frequency step between consecutive pulses in $u^{(i)}(t)$ becomes

$$\triangle f_{in} = \Delta f + k_M t_r = (k_N + k_M) t_r > 0. \tag{4.13}$$

Similar to the case of train (4.5), we require that $\Delta f_{in} \leq B$. As can be seen from Figure 4.4, the frequency band B_{in} of $u^{(i)}(t)$ is equal to

$$B_{in} = B + (N-1)\Delta f_{in} > 0. \tag{4.14}$$

We also recall that the total duration of $u^{(i)}(t)$ $(i = 1, 2, \ldots, M)$ is T_p.

At the same time, "inner" trains $u^{(1)}(t)$, $u^{(2)}(t), \ldots, u^{(M)}(t)$ form the "outer" train $u(t)$. In the time-frequency domain, the band of each train $u^{(i)}(t)$ $(i = 2, 3, \ldots, M)$ is shifted with respect to the band of $u^{(i-1)}(t)$ by the constant frequency

step

$$\Delta f_{out} = k_M T_r > 0. \tag{4.15}$$

Again, we suppose that $\Delta f_{out} \leq B_{in}$. Finally, we note that the total duration of $u(t)$ is

$$T = T_p + (M-1)T_r = t_p + (N-1)t_r + (M-1)T_r \tag{4.16}$$

and the combined frequency deviation of $u(t)$ is

$$B_{out} = B_{in} + (M-1)\Delta f_{out} = B + (N-1)\Delta f_{in} + (M-1)\Delta f_{out}. \tag{4.17}$$

At the end of this section, we would like to note that, even though all the "inner" and "outer" trains are constructed by means of constant frequency steps (Δf_{in} and Δf_{out}, respectively), the frequency steps between the center frequencies of the subpulses in the entire train $u(t)$ satisfy to a nonlinear law. This allows us to reshape the spectrum of $u(t)$ significantly and, as will be shown later, specify the waveform's parameters leading to the desired autocorrelation profiles.

We also remark that under the absence of either "inner" or "outer" trains in our design scheme, consisting of steps (4.1), (4.2), (4.5), (4.9), and (4.10), we would obtain an ordinary periodic stepped-frequency LFM train (3.8). It would be composed out of the same chirp pulse $s_p(t)$ and exhibit a constant frequency step between consecutive pulses.

4.2 Ambiguity Function of the proposed waveform

In this section we develop the ambiguity function $\chi_u(\tau, \nu)$ of the proposed waveform $u(t)$. Subsection 4.2.1 contains some theoretical preliminaries that will be used, along with other properties of the ambiguity function, in subsection 4.2.2 to derive

the closed form representation for $|\chi_u(\tau,\nu)|$. Based on this representation, we obtain the closed formula for the autocorrelation function of $u(t)$ in subsection 4.2.3.

4.2.1 Some properties of the ambiguity function of pulse trains

Our derivation of the ambiguity function of train (4.10) will be based on Theorem 3.6.1. Note that this theorem relates the ambiguity functions of waveforms $s_1(t)$ and $p_1(t)$ that both are centered at the origin. In the previous section, however, we have defined waveforms whose time support was $[0,t_w]$ for some $t_w > 0$. To make Theorem 3.6.1 useful in this case, we observe that the single pulse $s(t) = s_1\left(t - \frac{T}{2}\right)$ and the train

$$p(t) = p_1\left(t - \frac{1}{2}(N-1)T_r - \frac{T}{2}\right) = \sum_{n=0}^{N-1} s_1\left(t - nT_r - \frac{T}{2}\right) = \sum_{n=0}^{N-1} s(t-nT_r) \quad (4.18)$$

are time-limited with supports $[0,T]$ and $[0,(N-1)T_r+T]$, respectively. Then, applying the Time shift property of the ambiguity function (see **P.1** in subsection 1.1.2), we obtain

$$\chi_p(\tau,\nu) = \chi_{p_1}(\tau,\nu)e^{-j\pi\nu(T+(N-1)T_r)} \quad \text{and} \quad \chi_s(\tau,\nu) = \chi_{s_1}(\tau,\nu)e^{-j\pi\nu T}. \quad (4.19)$$

Now we can rewrite (3.7), due to (4.19), as follows:

$$\chi_p(\tau,\nu) = e^{-j\pi\nu(T+(N-1)T_r)}e^{j\pi\nu T}\sum_{n=-(N-1)}^{N-1}\chi_s(\tau-nT_r,\nu)\frac{\sin\left[\pi\nu T_r(N-|n|)\right]}{\sin\pi\nu T_r}. \quad (4.20)$$

Formula (4.20) allows us to relate the ambiguity surfaces of $p(t)$ and $s(t)$:

THEOREM 4.2.1 *(Ambiguity surface of a uniform pulse train) Let $s(t)$ be a pulse with the time support $[0,T]$ and $p(t)$ be the pulse train defined by* (4.18) *with $T_r > T$. Then*

$$|\chi_p(\tau,\nu)| = \left|\sum_{n=-(N-1)}^{N-1}\chi_s(\tau-nT_r,\nu)\frac{\sin\left[\pi\nu T_r(N-|n|)\right]}{\sin\pi\nu T_r}\right|. \quad (4.21)$$

As follows from Theorem 4.2.1, $|\chi_p(\tau,\nu)|$ is the sum of two-term products. The first factor in each product is the ambiguity function of single pulse $s(t)$ delayed by n PRI multiples, while the second factor is a periodic sinc function due to the pulse train. Note that, by property **P.9** from subsection 1.1.2, $\chi_s(\tau,\nu)$ vanishes for $\{(\tau,\nu) : |\tau| \geq T, \nu \in \mathbb{R}\}$. Therefore, the relation between T and T_r should be taken into account in order to determine the support of $|\chi_p(\tau,\nu)|$. Particularly, in the case $T_r > 2T$, which is subject to study in this chapter, representation (4.21) of $|\chi_p(\tau,\nu)|$ can be further simplified.

COROLLARY 4.2.1 *For $T_r > 2T$, formula (4.21) becomes*

$$|\chi_p(\tau,\nu)| = \begin{cases} \left|\chi_s(\tau - nT_r,\nu)\dfrac{\sin\left[\pi\nu T_r(N-|n|)\right]}{\sin \pi\nu T_r}\right|, & \text{if } \tau \in [nT_r - T, nT_r + T] \text{ and} \\ & n = -N+1,\ldots,N-1, \\ 0, & \text{otherwise.} \end{cases} \tag{4.22}$$

PROOF. For the case $T_r > 2T$, the relation between supports of $\chi_s(\tau - nT_r,\nu)$ for different values of n is schematically depicted in Figure 4.5. The proof follows immediately from the observation that supp $\chi_s(\tau - nT_r,\nu) = \{(\tau,\nu) : \tau \in [nT_r - T, nT_r + T],\ \nu \in \mathbb{R}\}$, which implies that the supports of $\chi_s(\tau - n_1T_r,\nu)$ and $\chi_s(\tau - n_2T_r,\nu)$ are not overlapping, if $n_1 \neq n_2$.

Since all the signals under consideration are supposed to be time-limited, we have to deal with the ambiguity surfaces represented in the form similar to (4.22). To make our notation shorter, we will indicate the representation of $|\chi(\tau,\nu)|$ only for those arguments (τ,ν) that are contained into its support. For example, the notation

$$|\chi_p(\tau,\nu)| = \left|\chi_s(\tau - nT_r,\nu)\frac{\sin\left[\pi\nu T_r(N-|n|)\right]}{\sin \pi\nu T_r}\right|,$$

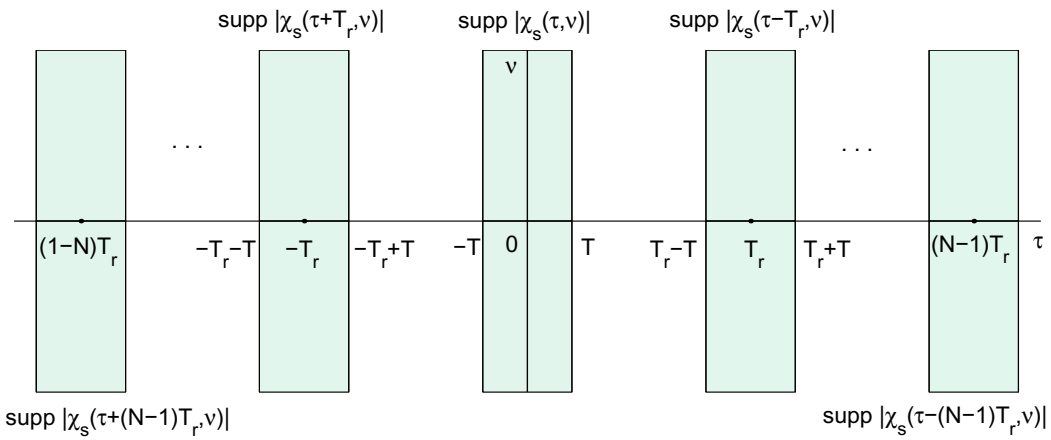

Figure 4.5: Support of the ambiguity function of uniform train $p(t)$ with $T_r > 2T$.

with $\tau \in [nT_r - T, nT_r + T],\ n = -N+1, -N+2, \ldots, N-1$, is equivalent to (4.22).

4.2.2 Ambiguity surface of train (4.10)

In this subsection we derive the closed form representation for the ambiguity surface of stepped-frequency LFM train (4.10).

We begin relating the ambiguity surface of the uniform train $s_N(t)$ defined by (4.2) to the ambiguity surface of the single pulse $s_p(t)$ (see (4.1)) constituting the train. It can be done, due to our assumption (4.3), by applying Corollary 4.2.1:

$$|\chi_{s_N}(\tau,\nu)| = \left|\chi_{s_p}(\tau - nt_r, \nu)\frac{\sin\left[\pi\nu t_r(N-|n|)\right]}{N\sin\pi\nu t_r}\right| \tag{4.23}$$

with $|\tau - nt_r| \le t_p$ and $n = -N+1, -N+2, \ldots, N-1$.

Adding LFM to $s_N(t)$ in (3.8) implies an affine transformation of the (τ,ν)-plane reflected by the Quadratic Phase Property. As the result we obtain the expression for the ambiguity surface of the single inner train $u_p(t)$:

$$\begin{aligned}|\chi_{u_p}(\tau,\nu)| &= \left|\chi_{s_N}(\tau, \nu - k_N\tau)\right| \\ &= \left|\chi_{s_p}(\tau - nt_r, \nu - k_N\tau)\frac{\sin\left[\pi t_r(\nu - k_N\tau)(N-|n|)\right]}{N\sin\left[\pi(\nu - k_N\tau)t_r\right]}\right|,\end{aligned} \tag{4.24}$$

where $|\tau - nt_r| \le t_p$ and n takes on integer values from $-N+1$ up to $N-1$.

Next, we use Corollary 4.2.1 again to get the relation between the ambiguity surface of the uniform pulse train $u_M(t)$ defined by (4.9) and the ambiguity surface of $u_p(t)$:

$$|\chi_{u_M}(\tau,\nu)| = \left|\chi_{u_p}(\tau - mT_r,\nu)\frac{\sin\left[\pi\nu T_r(M-|m|)\right]}{M\sin\pi\nu T_r}\right|,\ |\tau - mT_r| \le T_p, \qquad (4.25)$$

for $m = -M+1, -M+2, \ldots, M-1$. Taking into account representation (4.24) for $|\chi_{u_p}(\tau,\nu)|$, we rewrite (4.25) as follows:

$$\begin{aligned}|\chi_{u_M}(\tau,\nu)| &= \left|\chi_{s_p}(\tau - nt_r - mT_r, \nu - k_N(\tau - mT_r))\right| \\ &\times \left|\frac{\sin\left[\pi t_r(\nu - k_N\tau + mk_NT_r)(N-|n|)\right]}{N\sin\left[\pi(\nu - k_N\tau + mk_NT_r)t_r\right]}\cdot\frac{\sin\left[\pi\nu T_r(M-|m|)\right]}{M\sin\pi\nu T_r}\right| \qquad (4.26)\end{aligned}$$

with $|\tau - mT_r - nt_r| \le t_p$. In the above formula and hereafter we suppose that $n = -N+1, -N+2, \ldots, N-1$ and $m = -M+1, -M+2, \ldots, M-1$.

Now we apply property **P.6** (see subsection 1.1.2) to the waveforms $u(t)$ and $u_M(t)$ bound by relation (4.10). This allows us, due to (4.26), to express the ambiguity surface of the outer train $u(t)$ in terms of the ambiguity surface of the single chirp pulse $s_p(t)$:

$$\begin{aligned}|\chi_u(\tau,\nu)| = |\chi_{u_M}(\tau,\nu - k_M\tau)| &= \left|\chi_{s_p}(\tau - nt_r - mT_r, \nu - (k_N+k_M)\tau + mk_NT_r)\right| \\ \times \left|\frac{\sin\left[\pi t_r(\nu - (k_N+k_M)\tau + mk_NT_r)(N-|n|)\right]}{N\sin\left[\pi(\nu - (k_N+k_M)\tau + mk_NT_r)t_r\right]}\right.&\left.\cdot\frac{\sin\left[\pi(\nu - k_M\tau)T_r(M-|m|)\right]}{M\sin\left[\pi(\nu - k_M\tau)T_r\right]}\right|, \qquad (4.27)\end{aligned}$$

for $|\tau - mT_r - nt_r| \le t_p$. Since we want $|\chi_u(\tau,\nu)|$ to be expressed in terms of frequency characteristics $B, \triangle f, \triangle f_{in}$ and $\triangle f_{out}$ (defined by (4.12), (4.7), (4.13), and (4.15), respectively), the last formula leads us to the following final representation of $|\chi_u(\tau,\nu)|$:

$$|\chi_u(\tau,\nu)| = |\chi_1(\tau,\nu)|\cdot|\chi_2(\tau,\nu)|\cdot|\chi_3(\tau,\nu)|, \qquad |\tau - mT_r - nt_r| \le t_p, \qquad (4.28)$$

where

$$|\chi_1(\tau,\nu)| = \left|\chi_{s_p}(\tau - nt_r - mT_r, \nu - (k_N + k_M)\tau + mk_N T_r)\right|, \tag{4.29}$$

$$|\chi_2(\tau,\nu)| = \left|\frac{\sin\left[\pi(\nu t_r - \Delta f_{in}\tau + m\Delta f T_r)(N - |n|)\right]}{N\sin\left[\pi(\nu t_r - \Delta f_{in}\tau + m\Delta f T_r)\right]}\right|, \tag{4.30}$$

$$|\chi_3(\tau,\nu)| = \left|\frac{\sin\left[\pi(\nu T_r - \Delta f_{out}\tau)(M - |m|)\right]}{M\sin\left[\pi(\nu T_r - \Delta f_{out}\tau)\right]}\right|. \tag{4.31}$$

As can be seen from (4.28), for each subinterval $|\tau - mT_r - nt_r| \leq t_p$, the ambiguity surface of the stepped-frequency train $u(t)$ is the three-term product. The first factor in (4.28) can be obtained from the ambiguity surface of the chirp pulse (4.1) by appropriate translation of both time-delay and Doppler-delay axes. The explicit analytical representation of $|\chi_{s_p}(\tau,\nu)|$ is given by (3.5). Then,

$$\begin{aligned}|\chi_1(\tau,\nu)| &= \left|\chi_{s_p}(\tau - nt_r - mT_r, \nu - (k_N + k_M)\tau + mk_N T_r)\right| \\ &= \left|\left(1 - \frac{|\tau - nt_r - mT_r|}{t_p}\right)\operatorname{sinc}\left[(\nu - B\tau + mk_N T_r)\,(t_p - |\tau - nt_r - mT_r|)\right]\right|.\end{aligned} \tag{4.32}$$

We remark here that $|\chi_1(\tau,\nu)|$ also admits other simple interpretation. Note that stepped-frequency waveform $u(t)$, given by (4.10), can be constructed by repeating of the chirp pulse $s_u(t) = s_p(t)e^{j\pi(k_N+k_M)t^2}$ exactly NM times and applying appropriate time, phase, and frequency shifts to each subpulse. In other words, the chirp pulse $s_u(t)$ constitutes the waveform $u(t)$. Using the Quadratic Phase Property, we obtain $|\chi_{s_u}(\tau,\nu)| = |\chi_{s_p}(\tau, \nu - (k_N + k_M)\tau)|$. Hence,

$$|\chi_1(\tau,\nu)| = |\chi_{s_u}(\tau - nt_r - mT_r, \nu + mk_N T_r)|. \tag{4.33}$$

It follows from (4.33) that (1) the central envelope of $|\chi_1(\tau,\nu)|$ is the ambiguity surface of $s_u(t)$; (2) the other envelopes of $|\chi_1(\tau,\nu)|$ are obtained by translation $|\chi_{s_u}(\tau,\nu)|$ along time-delay and, for $m \geq 1$, Doppler-delay axes. Two remaining two factors in (4.28) are both periodic sinc functions. The first of them, $|\chi_2(\tau,\nu)|$, arises

due to the existence of the "inner" uniform train of N pulses, whereas the second one, $|\chi_3(\tau,\nu)|$, appears due to the outer uniform train of M pulses. As we will see later, the presence of these two factors enables us to perform much more flexible design comparing with traditional stepped-frequency LFM trains.

4.2.3 Autocorrelation function of the proposed waveform

As follows from subsection 1.1.2, the time-delay cross-section of the ambiguity surface produced by waveform $u(t)$ is nothing but the magnitude of the autocorrelation function of $u(t)$. Applying this observation to (4.28)–(4.31), we obtain

$$|R_u(\tau)| = |R_1(\tau)| \cdot |R_2(\tau)| \cdot |R_3(\tau)|\,, \qquad |\tau - mT_r - nt_r| \le t_p, \tag{4.34}$$

where $|R_u(\tau)| = |\chi_u(\tau,0)|$ and $|R_i(\tau)| = |\chi_i(\tau,0)|$ $(i = 1,2,3)$. In more details, the factors in (4.34) have the form

$$\begin{aligned}
|R_1(\tau)| &= |(1 - |\tau - nt_r - mT_r|/t_p)\,\mathrm{sinc}\,[(mk_NT_r - B\tau)\,(t_p - |\tau - nt_r - mT_r|)]|\,,\\
|R_2(\tau)| &= \left|\frac{\sin\left[\pi(m\Delta fT_r - \Delta f_{in}\tau)(N - |n|)\right]}{N\sin\left[\pi(m\Delta fT_r - \Delta f_{in}\tau)\right]}\right|,\\
|R_3(\tau)| &= \left|\frac{\sin\left[\pi\Delta f_{out}\tau(M - |m|)\right]}{M\sin\left[\pi\Delta f_{out}\tau\right]}\right|.
\end{aligned}$$

We recall from section 4.2.1 that the autocorrelation function of a pulse train with $t_r \ge 2t_p$ is a collection of nonoverlapping envelopes distributed along the time-delay axis. Among those envelopes, the central one, containing the main lobe, has the most practical importance, since, primarily, its shape evaluates the quality of radar measurements. In what follows, we concentrate on the profile of this central envelope only.

Letting $n = m = 0$ in (4.34), we obtain the representation for the magnitude of the autocorrelation function of train (4.10) for $|\tau| \le t_p$. The factors in the right-hand

side of (4.34) are now defined by formulas

$$|R_1(\tau)| = |(1 - |\tau|/t_p)\,\mathrm{sinc}\,[B\tau\,(t_p - |\tau|)]|\,, \tag{4.35}$$

$$|R_2(\tau)| = \left|\frac{\sin[\pi N \Delta f_{in}\tau]}{N\sin[\pi\Delta f_{in}\tau]}\right|, \qquad |R_3(\tau)| = \left|\frac{\sin[\pi M \Delta f_{out}\tau]}{M\sin[\pi\Delta f_{out}\tau]}\right|, \tag{4.36}$$

and the quantities $B, \Delta f_{in}$, and Δf_{out} are given by relations (4.12), (4.13), and (4.15), respectively.

Thus, the ACF of proposed here waveform $u(t)$ is the three-term product (4.34), where the first factor represents the ACF of any single subpulse forming the train and $|R_2(\tau)|$ and $|R_3(\tau)|$ are periodic sinc functions that appear due to the "inner" and "outer" trains described in section 4.1. In the next section we study some properties of $|R_u(\tau)|$.

4.3 Suppression of autocorrelation sidelobes in the proposed train

It is well-known that the autocorrelation function of traditional stepped-frequency LFM train (3.8) suffers from the grating lobes as well as a few relatively high first sidelobes in the vicinity of the main lobe. These high spikes essentially reduce waveform's resolution capabilities and, hence, they are completely undesirable. The purpose of this section is to demonstrate that the both issues can be successfully avoided in train (4.10) by right choice of waveform's parameters.

4.3.1 Preliminary comments

In this section we analyze the central envelope of $|R_u(\tau)|$. Although its structure, given by (4.34), (4.35), and (4.36), is more complicated than that one for the ACF of a traditional stepped-frequency LFM train (shown in (3.9)), each term in the

product (4.34) admits a simple geometric interpretation (see Figure 4.6 for details). Evidently, the relationship between the shapes of $|R_1(\tau)|, |R_2(\tau)|$, and $|R_3(\tau)|$ determines the $|R_u(\tau)|$'s profile and, as consequence, the height of the $|R_u(\tau)|$'s sidelobes.

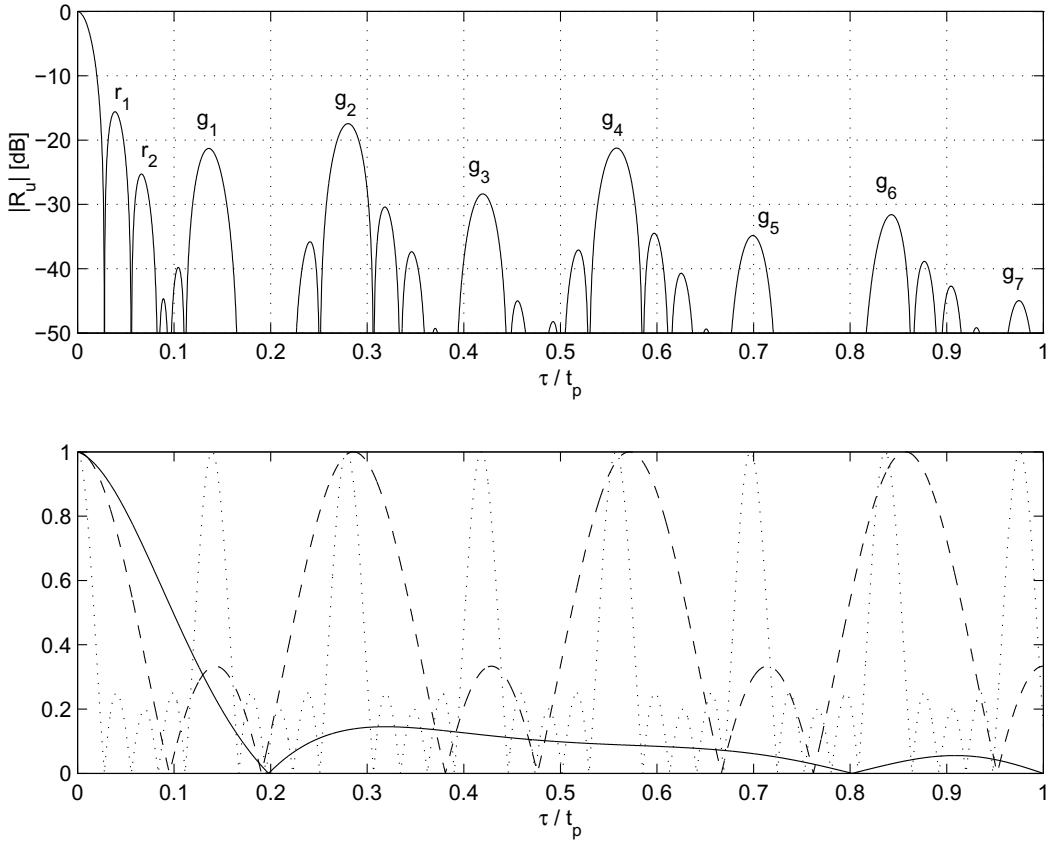

Figure 4.6: Top: the magnitude of the ACF of $u(t)$ with $N = 3, M = 5, \Delta f_{in} t_p = 3.5, \Delta f_{out} t_p = 7.175$, and $B t_p = 6.3$ (zoom on the interval $0 \leq \tau/t_p \leq 1$). Bottom: the relationship between $|R_1(\tau)|$ (solid), $|R_2(\tau)|$ (dashed), and $|R_3(\tau)|$ (dotted).

Depending on their sources and locations, the sidelobes of $|R_u(\tau)|$ can be classified into groups in the fashion similar to the classification of the $|R_s(\tau)|$'s sidelobes. Namely, we distinguish grating lobes (that are caused by the presence of two last

factors in (4.34) and located near the points of their maxima, i.e.

$$\tau_p^{\text{gr\_in}} = \frac{p}{\Delta f_{in}} \quad \text{and} \quad \tau_q^{\text{gr\_out}} = \frac{q}{\Delta f_{out}}$$

with $p = 1, 2, \ldots, \lfloor t_p \Delta f_{in} \rfloor$ and $q = 1, 2, \ldots, \lfloor t_p \Delta f_{out} \rfloor$), a few range sidelobes surrounding the main lobe, etc.

Figure 4.6 illustrates a typical profile of $|R_u(\tau)|$ with indication of two important groups (range and grating lobes) of time sidelobes. These groups would normally contain all the high sidelobes of $|R_u(\tau)|$. We denote two first (out of total four) range sidelobes near the main lobe of $|R_u(\tau)|$ by r_1 and r_2. The g_is (i=1,2,..., 7) indicate all the grating lobes presented in the ACF's profile. Note that most of the grating lobes are now located not exactly at the maxima of $|R_i(\tau)|(i = 2, 3)$, but at their close vicinity. The lobes g_2, g_4, and g_6 are caused by each of two last factors in (4.34), while g_1, g_3, g_5, and g_7 arise due to the third one only.

Taking into account the previous discussion and formula (4.34), it might seem, at the first look, that we had to expect worse (comparing with traditional LFM train) profile of $|R_u(\tau)|$. Indeed, now $|R_u(\tau)|$ is the product of three factors, two of which are periodic sinc functions that cause the appearance of the grating lobes. Hence, if $\Delta f_{in} \neq \Delta f_{out}$, the total number of the grating lobes should increase. In the contrary, our analysis shows that an appropriate relationship between the frequency steps Δf_{in} and Δf_{out} as well as right choice of the number of pulses in both "inner" and "outer" trains allows to suppress not only all the grating lobes but all the time sidelobes of $|R_u(\tau)|$ below the desired level.

As can be noticed from Figure 4.6, the ACF produced by train (4.10) contains, in general, a number of relatively high peaks. Analyzing the shape of the factors $|R_i(\tau)|(i = 1, 2, 3)$, however, one can observe that it is possible to choose the $u(t)$'s parameters such that the values of two of those three factors would be relatively small at the points where the third one attains its largest values. Hence, multiplying the

factors altogether should result in the ACF that takes on small values along the time-delay axis. Furthermore, a quite simple analytical representation (4.34) for $|R_u(\tau)|$ and relatively small number of the waveform's parameters make it possible to perform a systematic search for waveforms whose ACF sidelobes lowered below a desired level. Below we describe our approach and present results we have obtained.

Figures 4.7 and 4.8 illustrate the results that can be obtained by applying the approach mentioned above. For some applications, it is acceptable if the autocorrelation function would have the sidelobe level less than -30 dB at some vicinity of the main lobe and -40 dB otherwise. The $|R_u(\tau)|$ satisfying this requirement is presented in Figure 4.7. For the situations when very high range resolution is desired, waveforms producing the autocorrelation function similar to that one depicted in Figure 4.8 can be used. Note that in the both cases the total number of pulses in the resulting waveform is not large in contrast with the results of paper [29] which has reported about the possibility of acceptable sidelobe suppression by introducing a nonlinear frequency step in LFM trains with large number of pulses.

4.3.2 Formulation of the problem

In this subsection we describe the set of assumptions and restrictions we have made while analyzing the shape of $|R_u(\tau)|$.

First, we assume that the total number $K = NM$ of pulses in the train (4.10) is given and form the set Λ of all possible two-term factorizations of K with both factors greater than unity, i.e. $\Lambda = \{(n, m) : n, m \in \mathbb{Z}^+, n, m \geq 1, n \cdot m = K\}$. Then, for each pair $(n, m) \in \Lambda$, we let $N = n, M = m$ and look for values of the remaining parameters (i.e. $B, \Delta f_{in}, \Delta f_{out}$, and t_p) that would guarantee a low level of $u(t)$'s time sidelobes.

In what follows, we restrict the range of the parameters under consideration by

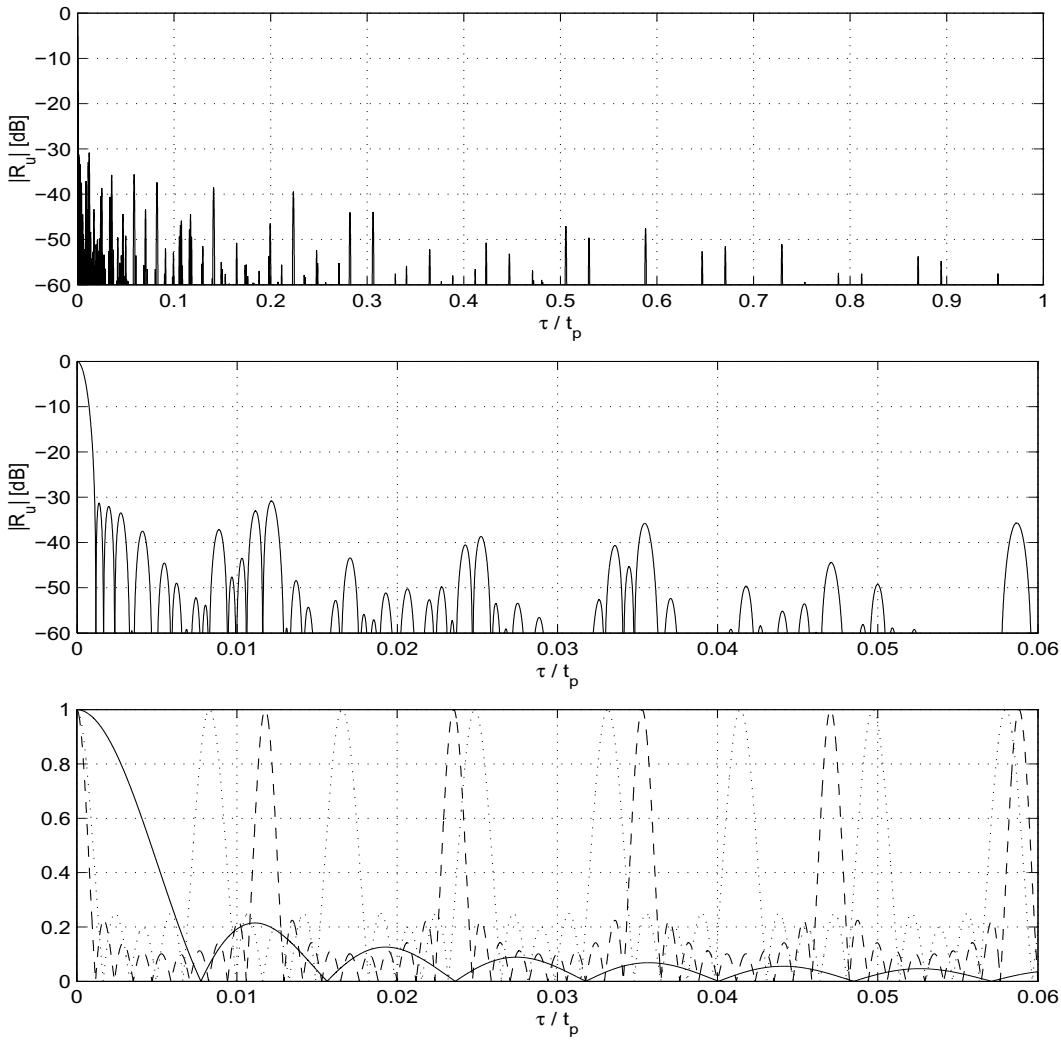

Figure 4.7: The magnitude $|R_u(\tau)|$ of the autocorrelation function of stepped-frequency pulse train (4.10) with $N = 10, M = 5, \Delta f_{in} t_p = 85, \Delta f_{out} t_p = 120.7, Bt_p = 130$. Top: zoom on the interval $0 \leq \tau/t_p \leq 1$. Middle: zoom on the interval $0 \leq \tau/t_p \leq 0.06$. Bottom: the relationship between $|R_1(\tau)|$ (solid), $|R_2(\tau)|$ (dashed), and $|R_3(\tau)|$ (dotted) for $0 \leq \tau/t_p \leq 0.06$.

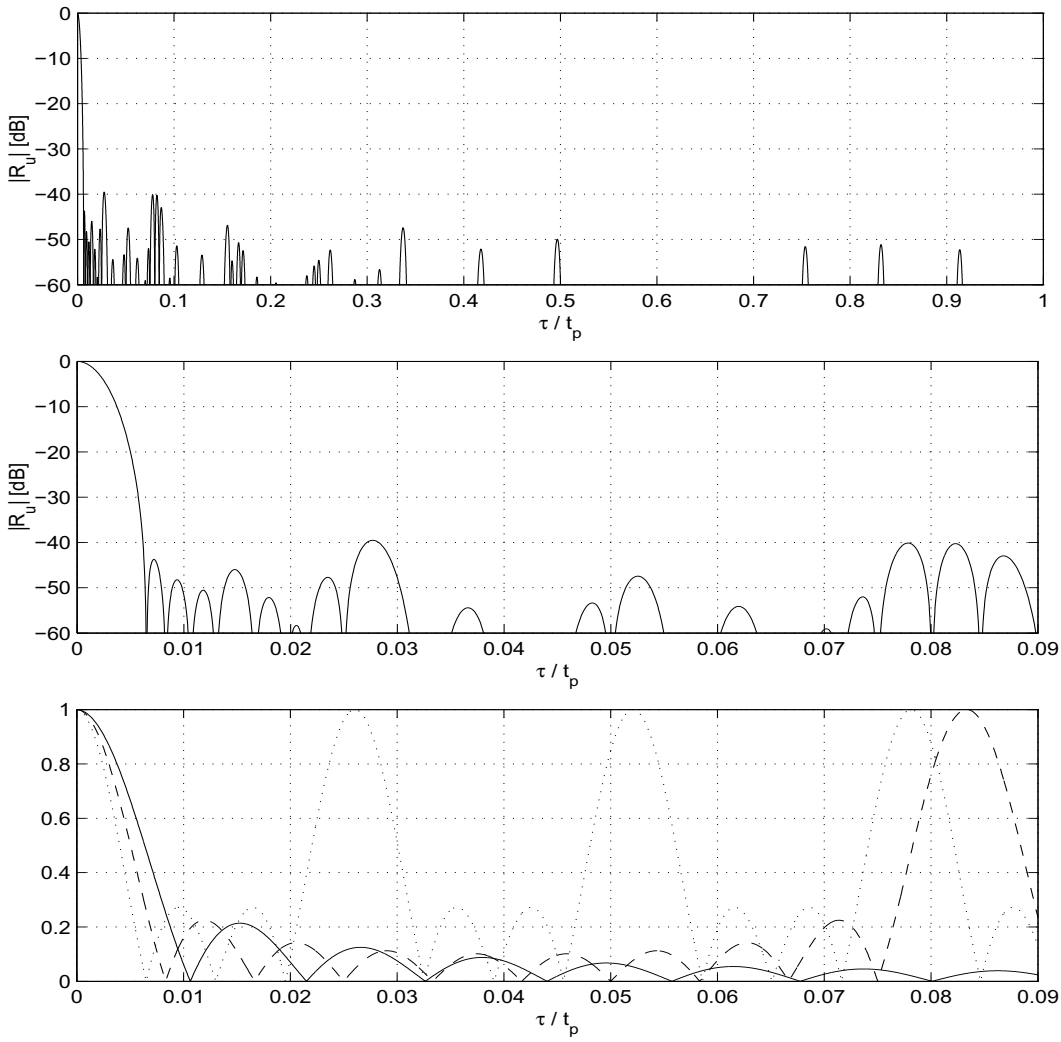

Figure 4.8: The magnitude $|R_u(\tau)|$ of the autocorrelation function of stepped-frequency pulse train (4.10) with $N = 10, M = 4, \Delta f_{in} t_p = 12, \Delta f_{out} t_p = 38.4, Bt_p = 95$. Top: zoom on the interval $0 \leq \tau/t_p \leq 1$. Middle: zoom on the interval $0 \leq \tau/t_p \leq 0.09$. Bottom: the relationship between $|R_1(\tau)|$ (solid), $|R_2(\tau)|$ (dashed), and $|R_3(\tau)|$ (dotted) for $0 \leq \tau/t_p \leq 0.09$.

the following set of conditions:

(i) We recall from section 4.1 that

$$\Delta f_{in} \leq B \tag{4.37}$$

and $\Delta f_{out} \leq B_{in}$. (The above conditions allow us to avoid frequency gaps between subpulses of $u(t)$.) The latter is equivalent to

$$\Delta f_{out}/\Delta f_{in} \leq B/\Delta f_{in} + N - 1. \tag{4.38}$$

(ii) We require that $|R_u(\tau)|(0 < \tau < t_p)$ would have at least one grating lobe caused by each of the terms $|R_2(\tau)|$ and $|R_3(\tau)|$. It can be done, if

$$\Delta f_{in} t_p > 1 \qquad \text{and} \qquad \Delta f_{out} t_p > 1. \tag{4.39}$$

(iii) We denote the first (counting from the origin) positive null of $|R_i(\tau)|$ by $\tau_i^{\text{null}}(i = 1, 2, 3)$. It can be noticed from both (4.35) and (4.36) that $\tau_1^{\text{null}} \approx 1/B, \tau_2^{\text{null}} = 1/(N\Delta f_{in})$, and $\tau_3^{\text{null}} = 1/(M\Delta f_{out})$. The first null τ^{null} of $|R_u(\tau)|$ (that manages the ACF main lobe width – one of most important resolution characteristics) is the smallest of those three quantities. Depending on the relationship between $\tau_1^{\text{null}}, \tau_2^{\text{null}}$, and τ_3^{null}, we can obtain three possible cases (illustrated in Figures 4.9 and 4.10) that would affect the resolution of $u(t)$.

We observe that, if $\tau^{\text{null}} = \tau_1^{\text{null}}$ (and, hence, $\tau_1^{\text{null}} < \tau_2^{\text{null}}$ and $\tau_1^{\text{null}} < \tau_3^{\text{null}}$), the overlap ratios, $B/\Delta f_{in}$ and $B/\Delta f_{out}$, become large. In more details, we would have both $B/\Delta f_{in} > N$ and $B/\Delta f_{out} > M$. In general, this would lead to significant (and undesirable) reduction of the waveform's total bandwidth B_{out}. That is why below we suppose that the value of τ^{null} would be originated by the first null of either $|R_2(\tau)|$ or $|R_3(\tau)|$. Hence,

$$\tau^{\text{null}} = \min\{\tau_2^{\text{null}}, \tau_3^{\text{null}}\} \tag{4.40}$$

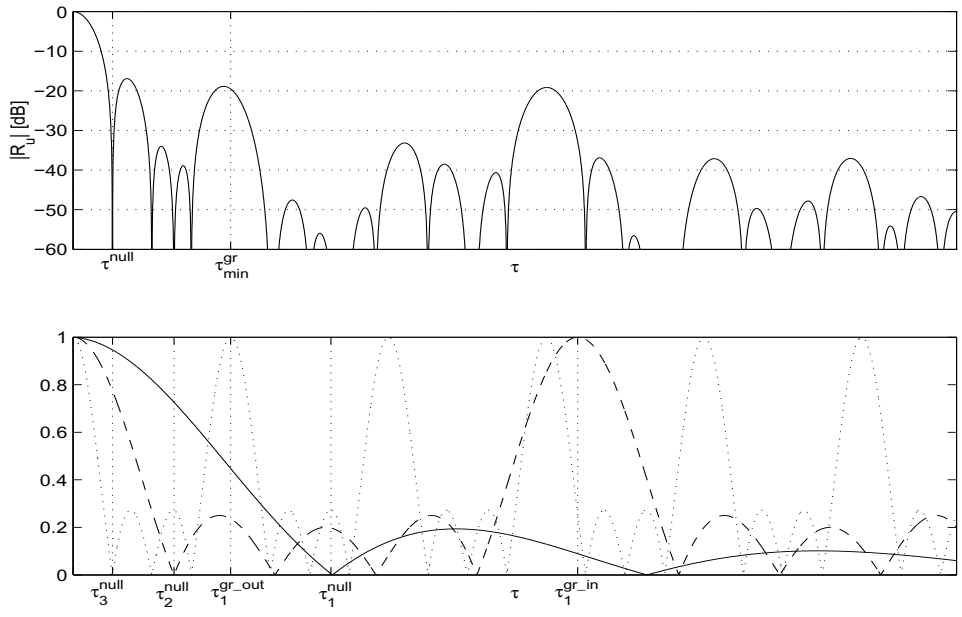

a) Case 1: $\tau^{\text{null}} = \tau_3^{\text{null}}$ and $\tau_{\text{min}}^{\text{gr}} = \tau_1^{\text{gr\_out}}$.

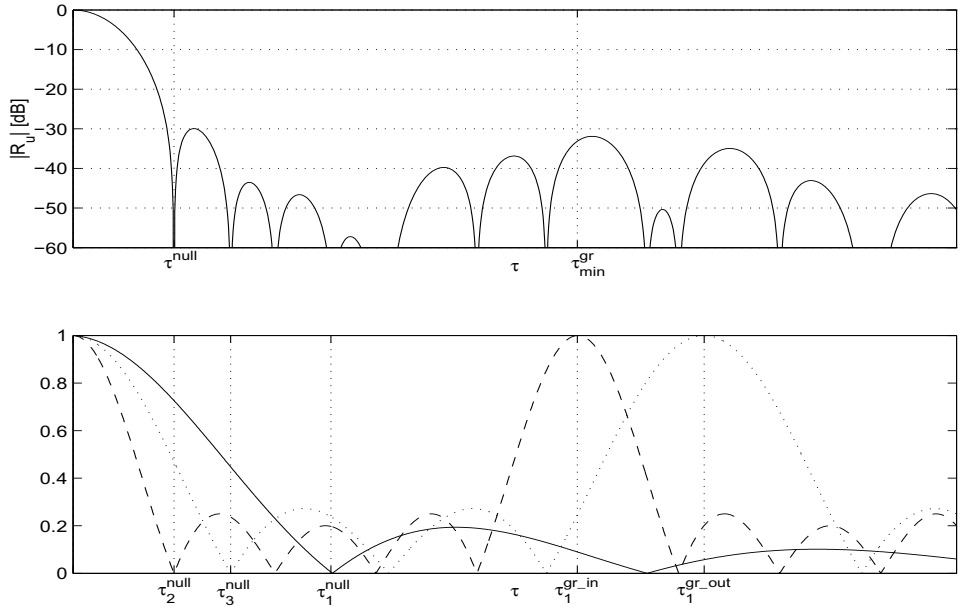

b) Case 2: $\tau^{\text{null}} = \tau_2^{\text{null}}$ and $\tau_{\text{min}}^{\text{gr}} = \tau_1^{\text{gr\_in}}$.

Figure 4.9: Relationship between the quantities (i) $\tau_1^{\text{null}}, \tau_2^{\text{null}}, \tau_3^{\text{null}}$, and τ^{null}, and (ii) $\tau_1^{\text{gr\_in}}, \tau_1^{\text{gr\_out}}$, and $\tau_{\text{min}}^{\text{gr}}$. For each subfigure, the top subplot shows partial ACF of $u(t)$ and the bottom subplot represents relationship between $|R_1(\tau)|$ (solid), $|R_2(\tau)|$ (dashed), and $|R_3(\tau)|$ (dotted) over the same time-delay interval.

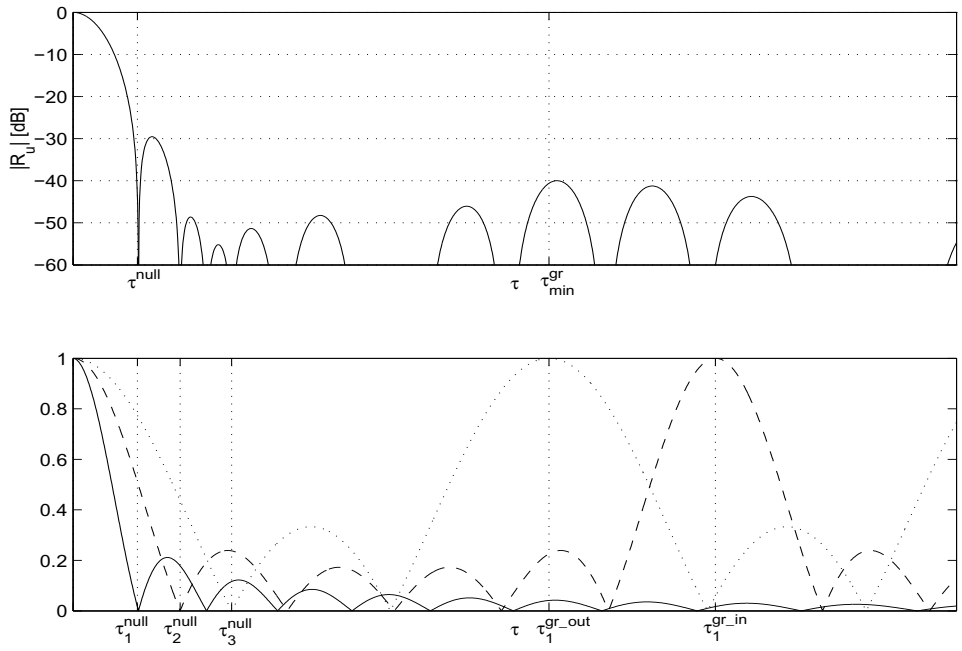

Figure 4.10: Relationship between the quantities (i) $\tau_1^{\text{null}}, \tau_2^{\text{null}}, \tau_3^{\text{null}}$, and τ^{null}, and (ii) $\tau_1^{\text{gr\_in}}, \tau_1^{\text{gr\_out}}$, and $\tau_{\min}^{\text{gr}}$. Case 3: $\tau^{\text{null}} = \tau_1^{\text{null}}$ and $\tau_{\min}^{\text{gr}} = \tau_1^{\text{gr\_out}}$. Top: partial ACF of $u(t)$. Bottom: relationship between $|R_1(\tau)|$ (solid), $|R_2(\tau)|$ (dashed), and $|R_3(\tau)|$ (dotted) over the same time-delay interval.

(i.e., only scenarios similar to those ones shown in Figure 4.9 will be considered). This fact implies that $\tau_1^{\text{null}} \geq \min\{\tau_2^{\text{null}}, \tau_3^{\text{null}}\}$. The last condition can be expressed in terms of the parameters of interest as follows

$$\begin{cases} B/\Delta f_{in} \leq N, & \text{if } \Delta f_{out}/\Delta f_{in} \leq N/M, \\ B/\Delta f_{out} \leq M, & \text{otherwise.} \end{cases} \tag{4.41}$$

We remark here that the first (from the main lobe) grating lobe of $|R_u(\tau)|$ arises near the point $\tau_{\min}^{\text{gr}} = \min\{\tau_1^{\text{gr\_in}}, \tau_1^{\text{gr\_out}}\} = \min\{1/\Delta f_{in}, 1/\Delta f_{out}\}$ (see Figure 4.9). That is why below we refer to the intervals $I_{\text{r}} = (\tau^{\text{null}}, \tau_{\min}^{\text{gr}})$ and $I_{\text{gr}} = [\tau_{\min}^{\text{gr}}, t_p)$ as of range sidelobes and grating lobes regions, respectively.

(iv) Note that if one seeks to push all the sidelobes, appearing in the grating lobes region, below some predetermined level ϵ (here ϵ is some small, a priori chosen, value defining the desired level of sidelobes suppression), then, generally speaking, only a few (if any) time sidelobes, belonging to a portion of $I_{\rm gr}$, should be pushed down in order to satisfy this desideratum. Indeed, since all the factors in (4.34) do not exceed 1 and, for any $\tau > 0$, the $|R_1(\tau)|$ admits an upper estimate

$$|R_1(\tau)| = \frac{|\sin(\pi B\tau(1-|\tau|/t_p))|}{\pi B\tau} \le \frac{1}{\pi B\tau},$$

we conclude that the inequality $|R_u(\tau)| \le \epsilon$ will be automatically fulfilled for all $\tau \ge \tau_*$, where $\tau_* = 1/(\pi B\epsilon)$. In particular, all the peaks from the grating lobes region will be lowered below the ϵ-level, when $\tau_* \le \tau_{\min}^{\rm gr}$. This assumption yields that $\tau_* \le \tau_1^{\rm gr\_in}$ and $\tau_* \le \tau_1^{\rm gr\_out}$ or, equivalently, $B/\Delta f_{in} \ge 1/(\pi\epsilon)$ and $B/\Delta f_{out} \ge 1/(\pi\epsilon)$. The ACF of a waveform with parameters satisfying to these conditions is shown in Figure 4.11. As can be seen from the figure, all the sidelobes from the grating lobes region and some sidelobes from the range sidelobes region are suppressed below -40dB level. Again, we note that, in this case, the overlap ratios, $B/\Delta f_{in}$ and $B/\Delta f_{out}$, become large. So, we eliminate this possibility from further discussion and set

$$B/\Delta f_{in} < 1/(\pi\epsilon) \qquad \text{and} \qquad B/\Delta f_{out} < 1/(\pi\epsilon). \tag{4.42}$$

Now we form the set $\Omega_{(n,m)} \subset \mathbb{R}^3$ of quantities

$$(x, y, z) = (\Delta f_{in} t_p, B/\Delta f_{in}, \Delta f_{out}/\Delta f_{in})$$

satisfying the conditions (4.37)-(4.39), (4.41), and (4.42). Note that $\Omega_{(n,m)}$ is not empty for small values of ϵ. (It is usually desirable to suppress the grating lobes below a level which does not exceed -40dB. Consequently, we have to deal with

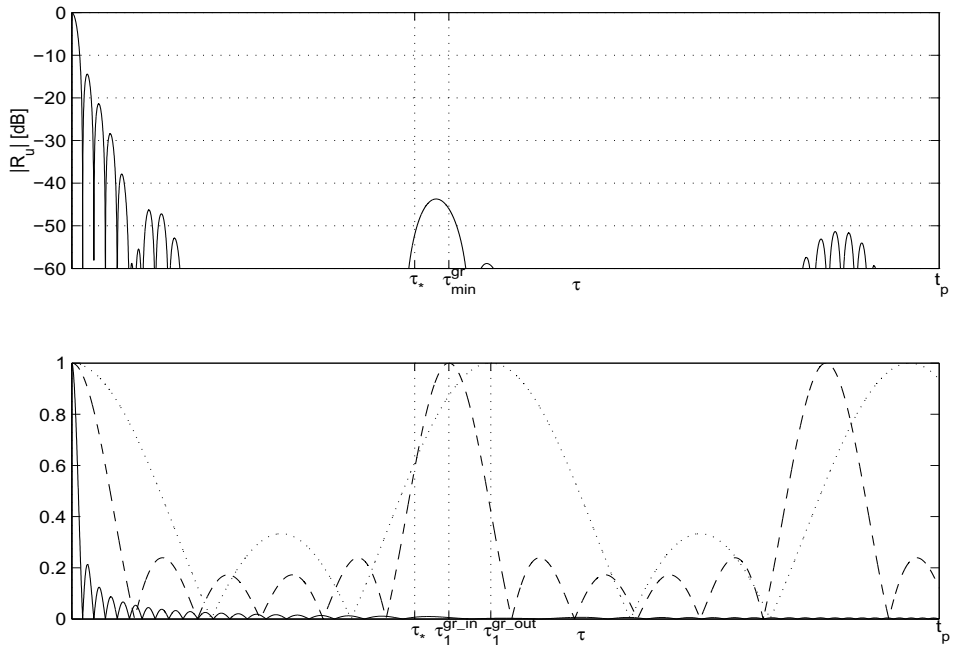

Figure 4.11: Example of the ACF with $\tau_* \leq \tau_{\min}^{\mathrm{gr}}$. All the grating lobes of $R_u(\tau)$ are suppressed below -40dB ($\epsilon = 0.01$). Top: The ACF of stepped-frequency pulse train (4.10) with $N = 6, M = 3, \Delta f_{in} t_p = 2.3, \Delta f_{out} t_p = 2.07, B t_p = 80.5$. Bottom: Relationship between $|R_1(\tau)|$ (solid), $|R_2(\tau)|$ (dashed), and $|R_3(\tau)|$ (dotted).

values of ϵ which are not greater than 0.01). To justify our claim, we rewrite the set of conditions (4.37)-(4.39), (4.41), and (4.42) in terms of new variables x, y, and z. For our convenience, we represent them as the union of two sets of inequalities:

$$\begin{cases} 1 \leq y \leq N, \\ y < 1/(\pi\epsilon), \\ \pi\epsilon y < z \leq y + N - 1, \\ 1/x < z \leq N/M, \\ x > 1, \end{cases} \quad \text{or} \quad \begin{cases} y \geq 1, \\ y < 1/(\pi\epsilon), \\ \pi\epsilon y < z \leq y + N - 1, \\ z > N/M, \\ z > y/M, \\ x > 1. \end{cases} \tag{4.43}$$

Next, we consider a cross-section of $\Omega_{(n,m)}$, which is parallel to the Oyz-plane, for a relatively large x. It is schematically depicted in Figure 4.12. All the el-

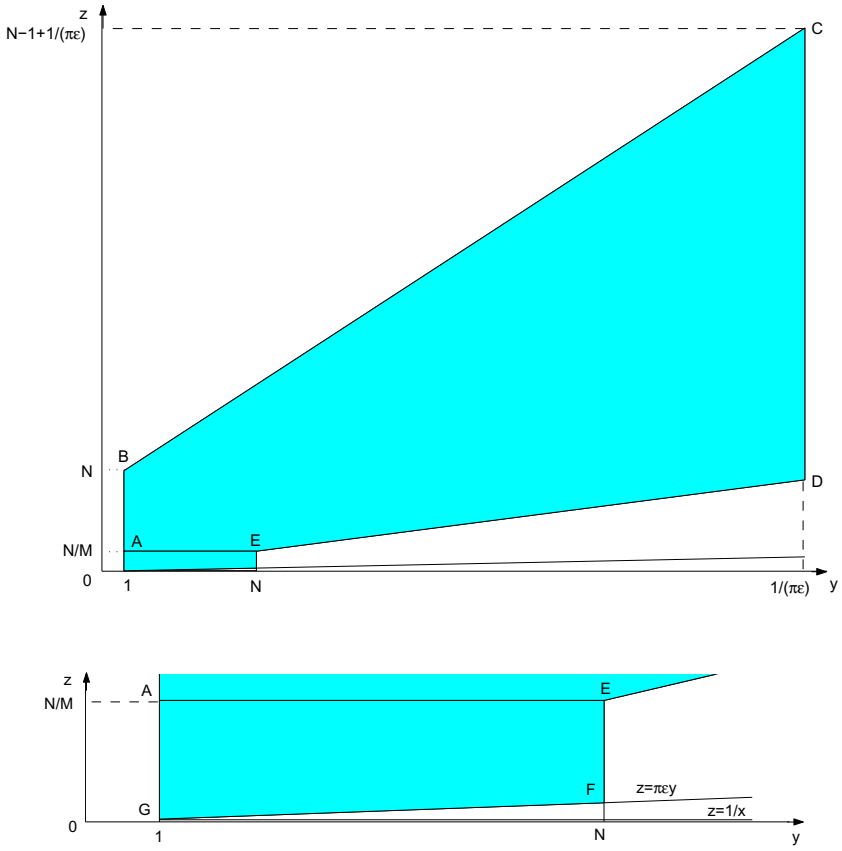

Figure 4.12: Parallel to the Oyz-plane cross-section of $\Omega_{(n,m)}$ for $x > 1/(\pi\epsilon)$. (Top: polygon $ABCDEFG$. Bottom: polygon $AEFG$.)

ements of $\Omega_{(n,m)}$ belonging to the cross-section form a region bounded by the edges of polygon $ABCDEFG$ (here $A(1, N/M), B(1, N), C(1/(\pi\epsilon), N-1+1/(\pi\epsilon))$, $D(1/(\pi\epsilon), 1/(M\pi\epsilon)), E(N, N/M), F(N, N\pi\epsilon)$, and $G(1, \pi\epsilon)$). Edges AB, BC, CD, DE, and AE of polygon $ABCDE$ lie on straight lines given by $y = 1, z = y + N - 1, y = 1/(\pi\epsilon), z = y/M$, and $z = N/M$, respectively. It is easy to check that any point chosen from the interior of $ABCDE$ satisfies the left system of inequalities in (4.15). At the same time, the interior of polygon $AEFG$ is described by the right set of inequalities in (4.15). We note that, although, generally speaking, a cut of $\Omega_{(n,m)}$ may look different from that one we have shown, Figure 4.12 corresponds

to the most interesting case, when $M < 1/(\pi\epsilon) < x$. It can be also noticed that, once quantities N, M, and ϵ have been chosen in accordance with the above conditions, all the cross-sections of $\Omega_{(n,m)}$ parallel to the Oyz-plane will be identical for $x > 1/(\pi\epsilon)$.

Finally, we perform numerical search for members of $\Omega_{(n,m)}$ that correspond to waveforms producing desired ACF profiles. In our study, we are interested in the waveforms whose ACF exhibit a predetermined (and, generally, different) levels of sidelobes suppression over I_{r} and I_{gr} (we write ϵ_1 and ϵ_2, respectively, for the quantities defining those levels). Therefore, we set the search criteria as follows:

$$|R_u(\tau)| \leq \epsilon_1,\ \tau \in I_{\mathrm{r}}, \tag{4.44}$$

$$|R_u(\tau)| \leq \epsilon_2,\ \tau \in I_{\mathrm{gr}}. \tag{4.45}$$

As the result, we obtain the "output" set $\Omega_{(n,m)}^{(\mu_1,\mu_2)} \subseteq \Omega_{(n,m)}$ consisting of the parameter values of interest. (Here $\mu_i (i = 1, 2)$ represents the desired level of suppression ϵ_i expressed in dB units).

4.3.3 Numerical Results

In this subsection we demonstrate some results we have obtained while studying two variants of problem (4.44), (4.45) corresponding to the ACF peaks suppression over: 1) the grating lobes region only (here we set $\epsilon_1 = 1$), or 2) both regions of interest.

We have conducted the numerical search for two cases, when the total number of pulses forming the proposed waveform, K, is 35 and 77, respectively. In the first case ($K = 35$), the number of pulses can be only factorized as $K = 5 \cdot 7$. Hence, in this case $\Lambda = \{(5, 7), (7, 5)\}$ and we have the sets $\Omega_{(5,7)}$ and $\Omega_{(7,5)}$ of parameter values to search in. Likewise, if $K = 77$, we consider sets $\Omega_{(11,7)}$ and $\Omega_{(7,11)}$, since $\Lambda = \{(11, 7), (7, 11)\}$. While analyzing the above parameter sets, we

have additionally assumed that $\Delta f_{in} t_p$ would take on integer values up to 200.

Our analysis of the first variant of problem (4.44), (4.45), for $K = 35$, shows that it is possible to push the ACF sidelobes over I_{gr} down below the level as low as -50 dB. Figure 4.13 illustrates the ACF of one of the waveforms we have found. Since the search have been conducted for waveforms with low sidelobes over I_{gr} only, most of the waveforms found exhibit high range sidelobes. For instance, the ACF shown in Figure 4.13 has PSL about -26dB.

Figures 4.14-4.19 are related to the case of overall sidelobe suppression. Figure 4.14 demonstrates the sets $\Omega_{(7,5)}^{(-30,-40)}$ and $\Omega_{(5,7)}^{(-30,-40)}$. Evidently, one can construct numerous LFM trains having the range sidelobes suppressed below -30dB and the grating lobes lowered below -40dB. Figures 4.15 and 4.16 show the sets $\Omega_{(7,5)}^{(-40)}$ and $\Omega_{(5,7)}^{(-40)}$ (we write $\Omega_{(n,m)}^{(-40)}$ for $\Omega_{(n,m)}^{(-40,-40)}$). As can be seen from the figures, parameters providing the desired threshold level form non-overlapping regions in the $\mathbb{R}^3$. A typical ACF for a waveform with the parameters chosen from $\Omega_{(7,5)}^{(-40)}$ is drawn in Figure 4.17.

It appears that the best level of suppression we have been able to find for proposed waveforms consisting of 35 pulses is achieved by small number of waveforms associated with $\Omega_{(n,m)}^{(-40,-45)}, (n,m) \in \Lambda$. We list the parameters of a few waveforms from this set in Table 4.1. The ACFs produced by two of them are shown in Figures 4.18 and 4.19. The overall level of time sidelobes suppression, for the ACFs depicted, is -41.3dB and -42dB, respectively.

Next, we present the results we have obtained for waveforms consisting of 77 pulses. It is well-known that the increase in the number of pulses constituting the train makes the design of its ACF more flexible. In our case, this claim can be justified based on the following observation. Let us consider two LFM trains $u_1(t)$ and $u_2(t)$ defined by (4.10). We assume that $u_1(t)$ consists of 35 pulses, while $u_2(t)$

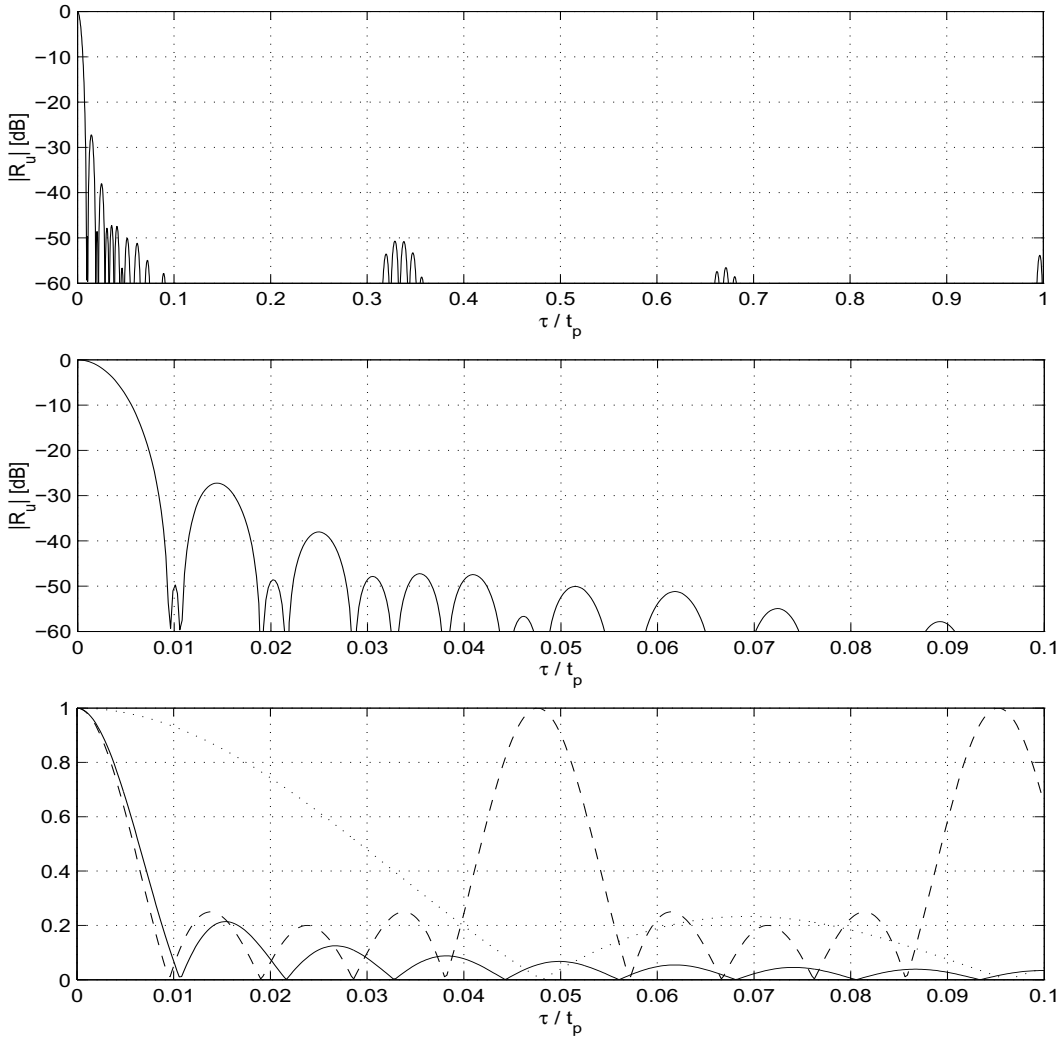

Figure 4.13: Partial ACF of $u(t)$ with $N = 5, M = 7$, $\Delta f_{in} t_p = 21, \Delta f_{out} t_p = 2.97$, and $Bt_p = 94.5$. Top: zoom on the interval $0 \leq \tau/t_p \leq 1$. Middle: zoom on the interval $0 \leq \tau/t_p \leq 0.1$. Bottom: the relationship between $|R_1(\tau)|$ (solid), $|R_2(\tau)|$ (dashed), and $|R_3(\tau)|$ (dotted).

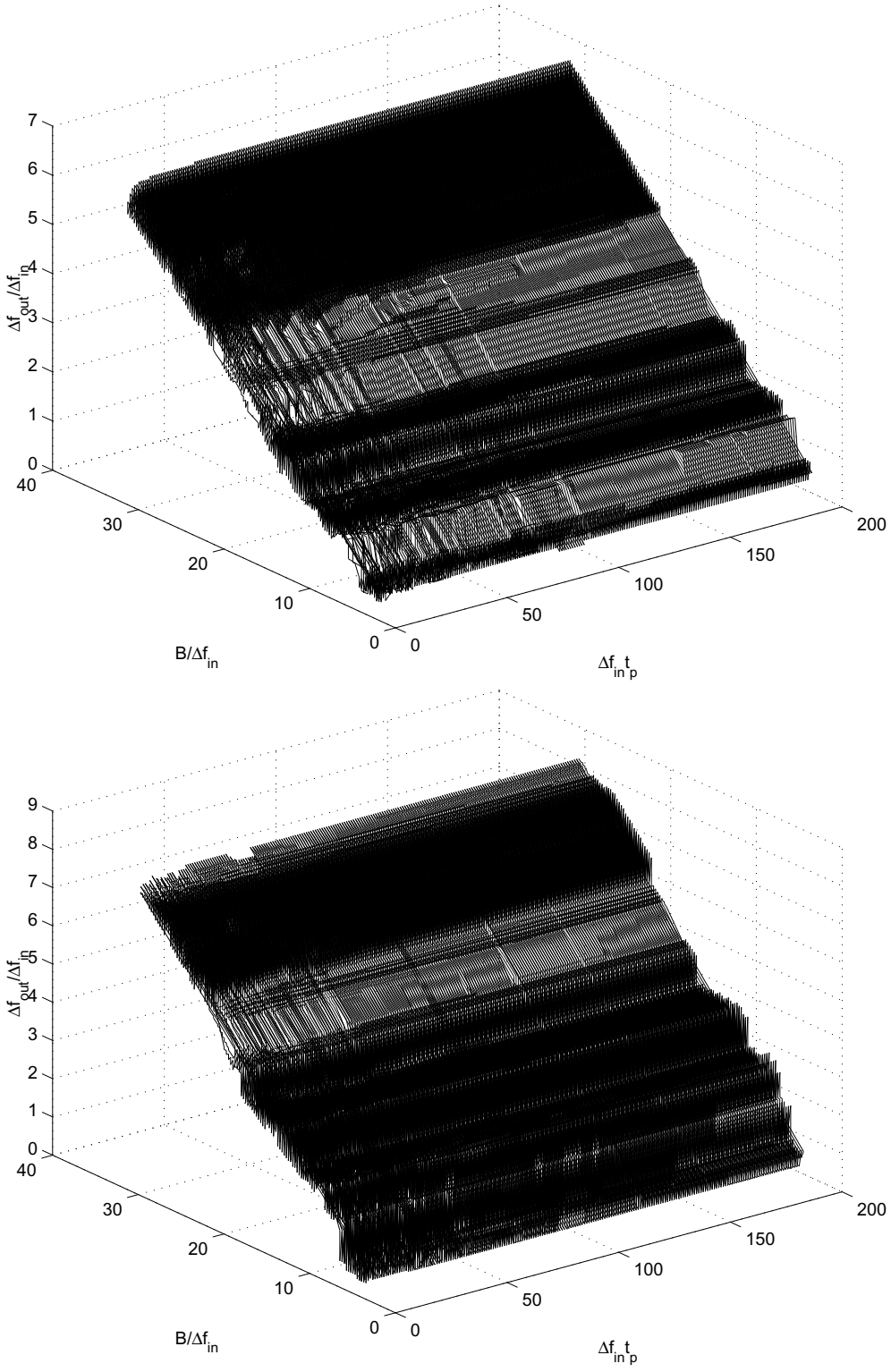

Figure 4.14: Pictorial representation of $\Omega_{(7,5)}^{(-30,-40)}$ (top) and $\Omega_{(5,7)}^{(-30,-40)}$ (middle).

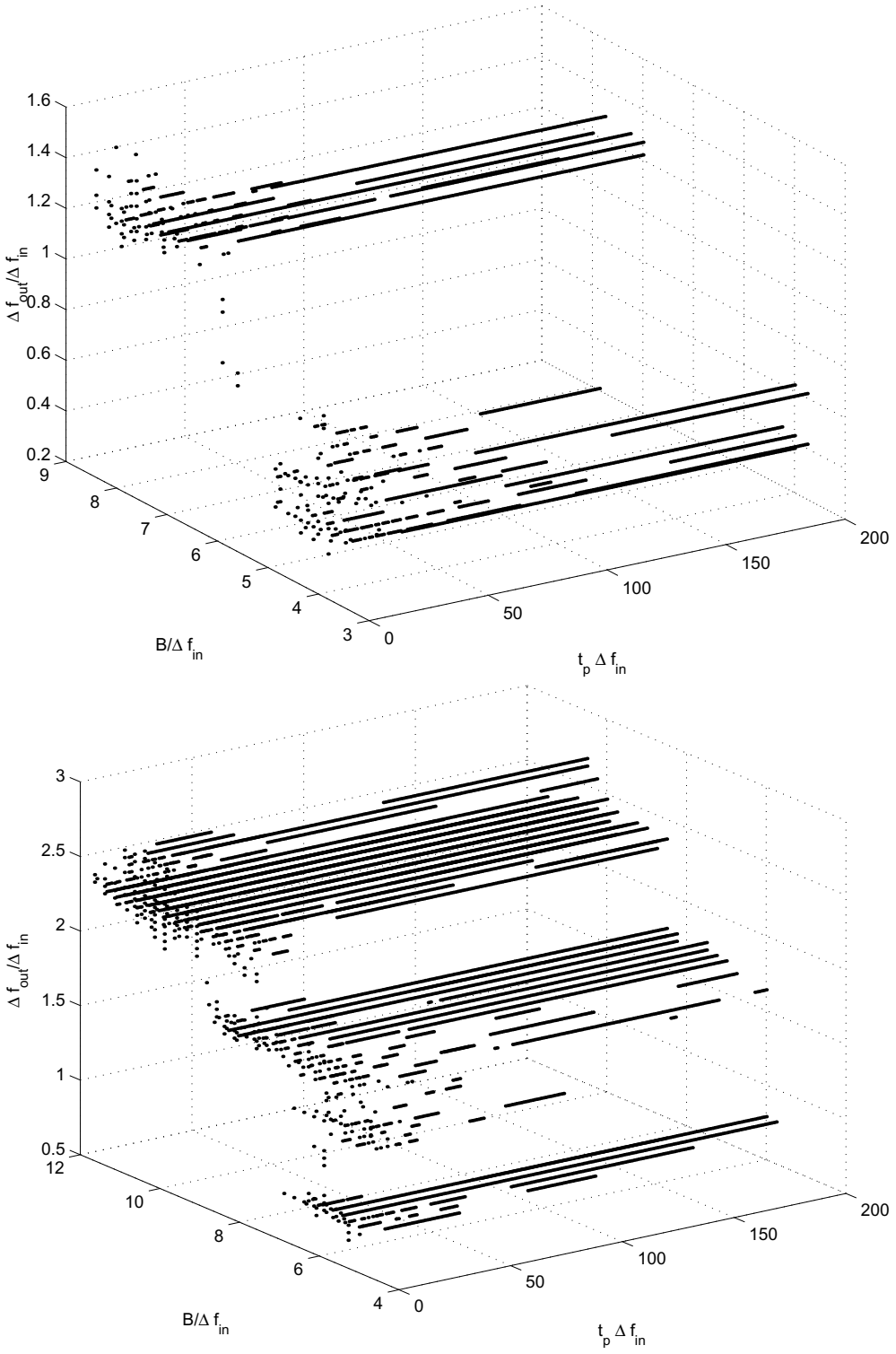

Figure 4.15: Pictorial representation of $\Omega^{(-40)}_{(5,7)}$ (top) and $\Omega^{(-40)}_{(7,5)}$ (middle).

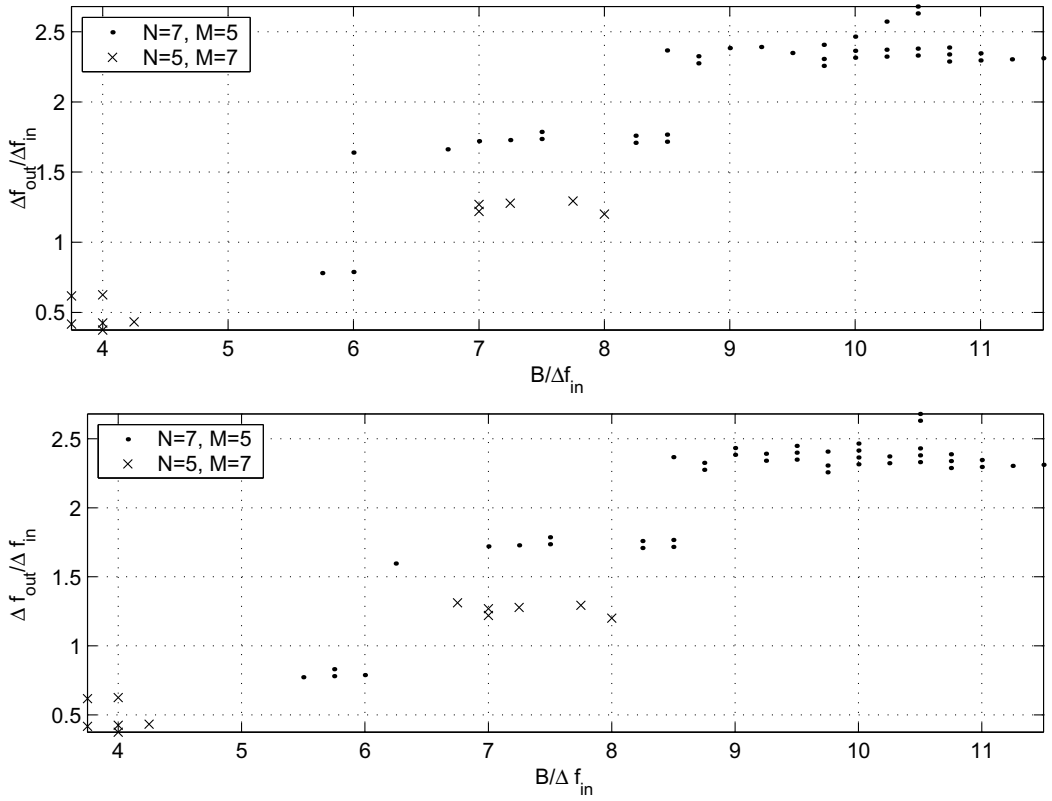

Figure 4.16: The elements of $\Omega_{(7,5)}^{(-40)}$ (denoted by '$\cdot$') and $\Omega_{(5,7)}^{(-40)}$ ('$\times$') for $\Delta f_{in} t_p = 100$ (top) and $\Delta f_{in} t_p = 150$ (bottom).

N	M	$\Delta f_{in} t_p$	$\Delta f_{out} t_p$	$B t_p$	$B_{total} t_p$	PSL, dB	τ^{null}
7	5	15	39.57	161.25	409.5	-40.12	0.0051
7	5	21	48.93	220.5	542.2	-41.3	0.0041
5	7	9	12.02	67.5	175.2	-42	0.0119
5	7	43	16.15	172	440.92	-40	0.0047

Table 4.1: Examples of waveforms with the parameters belonging to either $\Omega_{(5,7)}^{(-40,-45)}$ or $\Omega_{(7,5)}^{(-40,-45)}$.

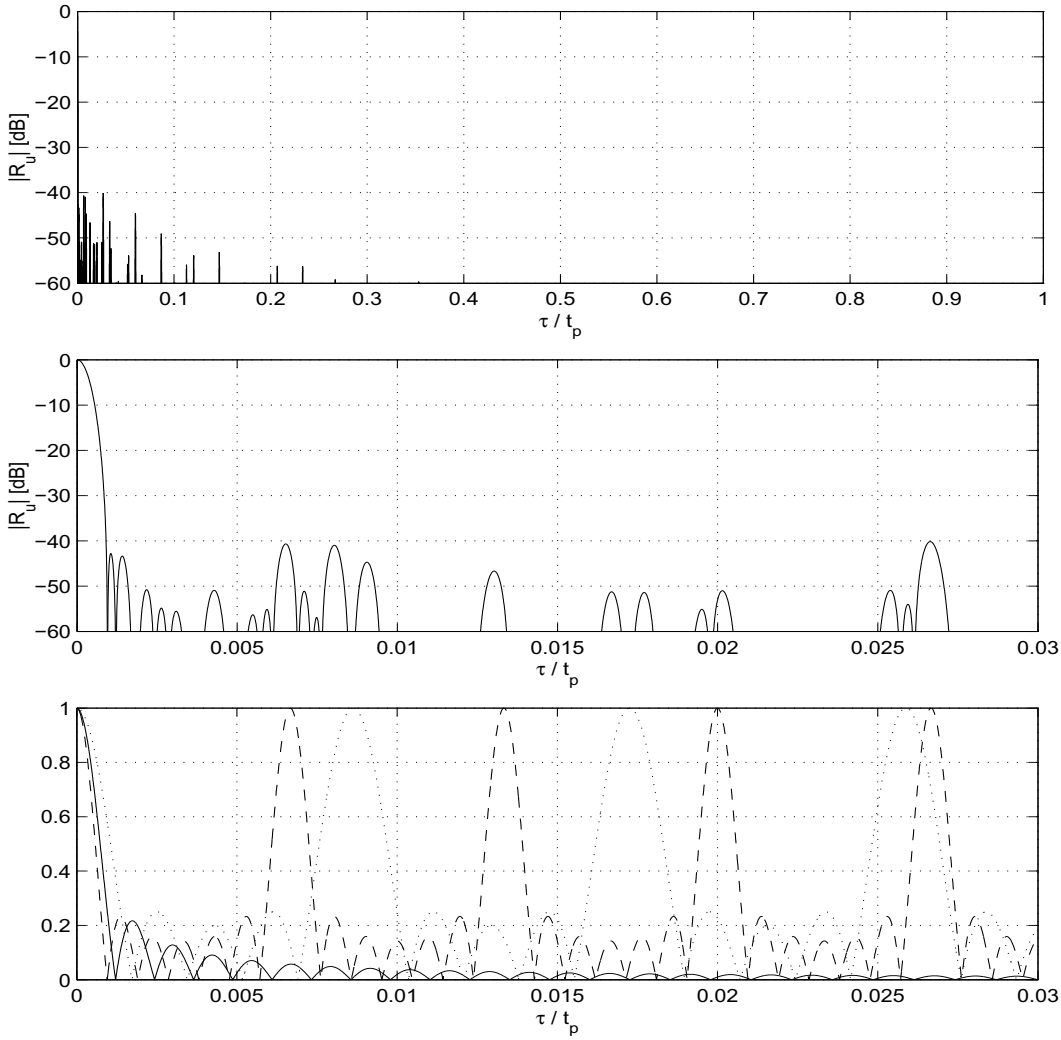

Figure 4.17: Partial ACF of $u(t)$ with $N = 7, M = 5$, $\Delta f_{in} t_p = 150, \Delta f_{out} t_p = 115.92$, and $Bt_p = 825$. Top: zoom on the interval $0 \leq \tau/t_p \leq 1$. Middle: zoom on the interval $0 \leq \tau/t_p \leq 0.03$. Bottom: the relationship between $|R_1(\tau)|$ (solid), $|R_2(\tau)|$ (dashed), and $|R_3(\tau)|$ (dotted).

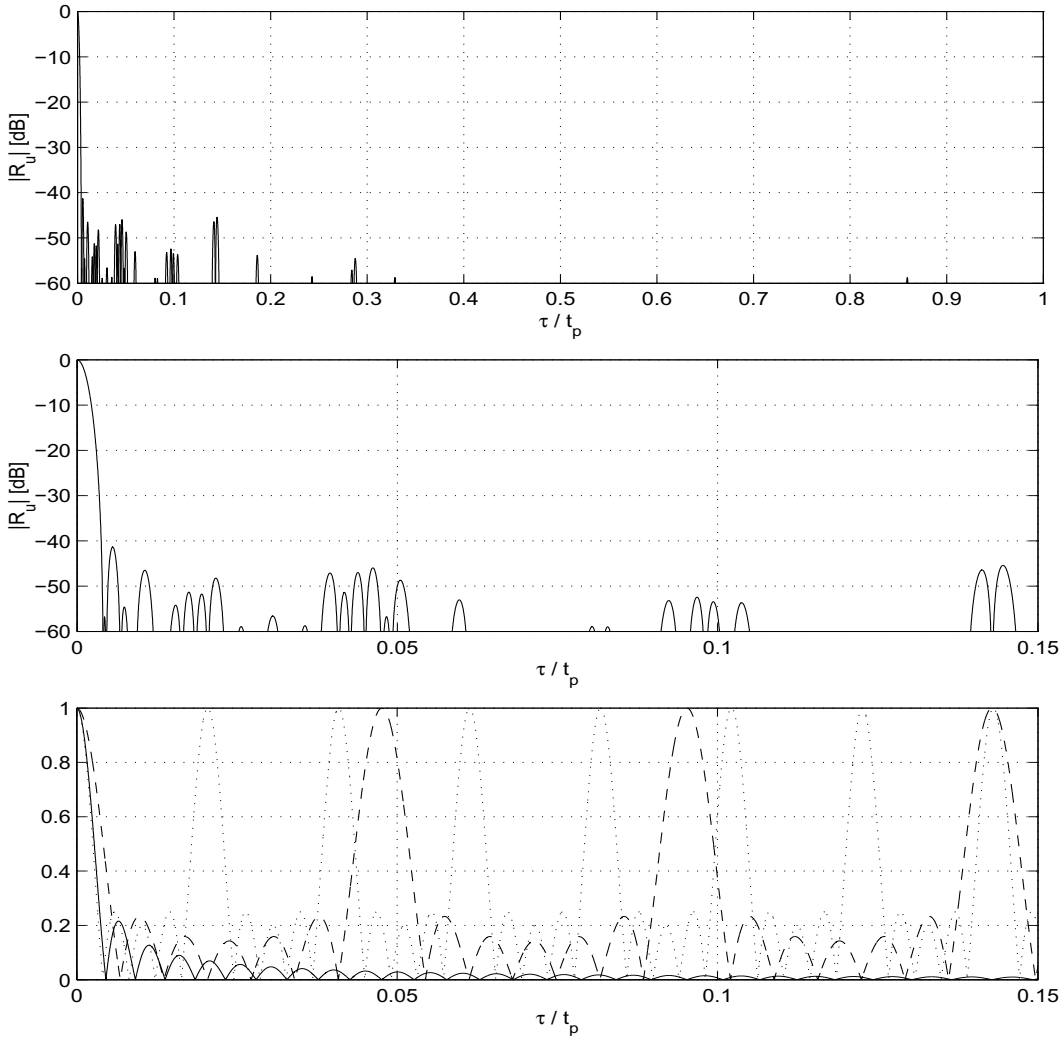

Figure 4.18: Partial ACF of $u(t)$ with $N = 7, M = 5$, $\Delta f_{in} t_p = 21, \Delta f_{out} t_p = 48.93$, and $Bt_p = 220.5$. Top: zoom on the interval $0 \leq \tau/t_p \leq 1$. Middle: zoom on the interval $0 \leq \tau/t_p \leq 0.15$. Bottom: the relationship between $|R_1(\tau)|$ (solid), $|R_2(\tau)|$ (dashed), and $|R_3(\tau)|$ (dotted).

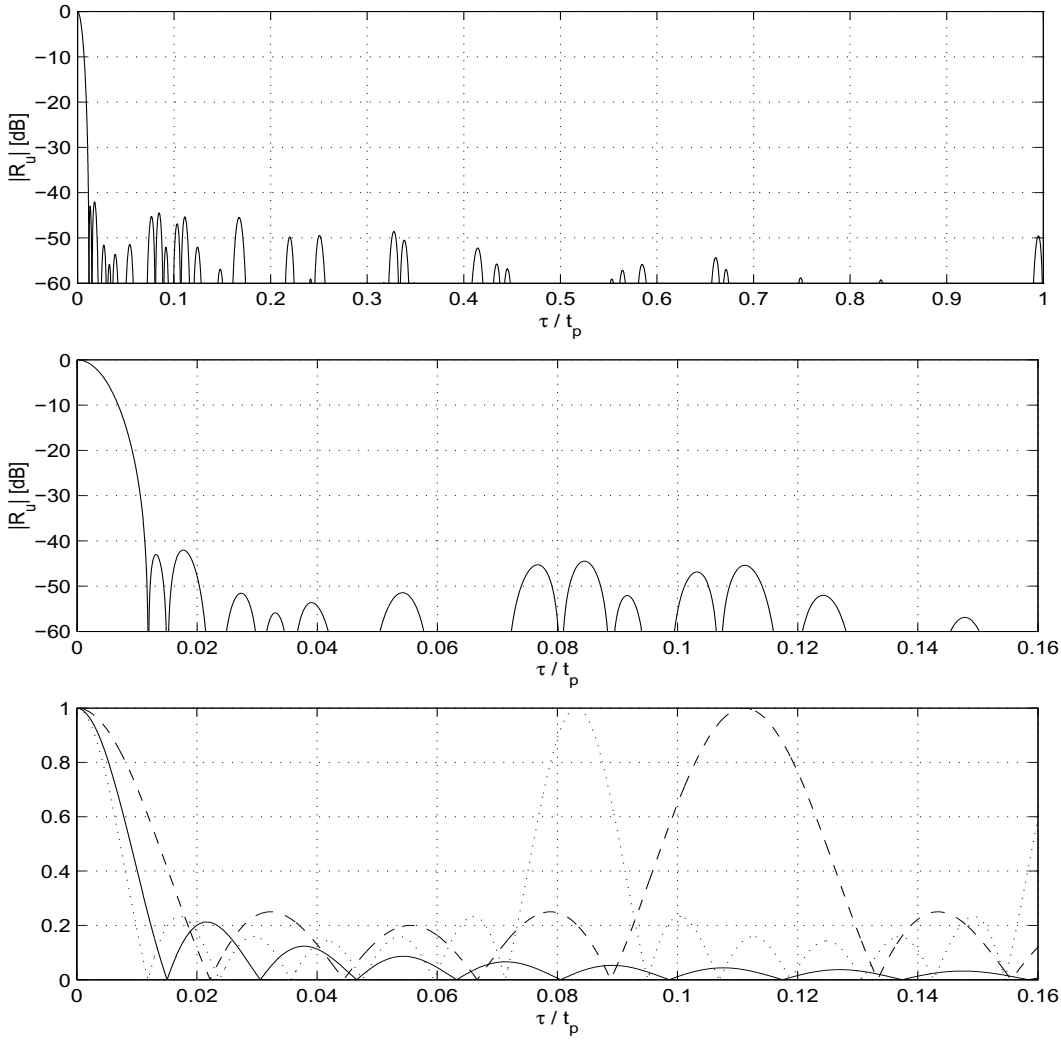

Figure 4.19: Partial ACF of $u(t)$ with $N = 5, M = 7$, $\Delta f_{in} t_p = 9, \Delta f_{out} t_p = 12.02$, and $Bt_p = 67.5$. Top: zoom on the interval $0 \leq \tau/t_p \leq 1$. Middle: zoom on the interval $0 \leq \tau/t_p \leq 0.16$. Bottom: the relationship between $|R_1(\tau)|$ (solid), $|R_2(\tau)|$ (dashed), and $|R_3(\tau)|$ (dotted).

has 77 pulses. (Without loss of generality, we let $N = 7, M = 5$, for $u_1(t)$, and $N = 7, M = 11$, for $u_2(t)$.) It is further assumed that the other parameters of both trains (i.e., $Bt_p, \Delta f_{in} t_p$, and $\Delta f_{out} t_p$) are the same. It can be noticed now from (4.34) that the ACF of $u_2(t)$ can be obtained from the $|R_{u_1}(\tau)|$ by replacing the last term, which is a periodic sinc function with $N_2 = 5$, by other periodic sinc function with $N_2 = 11$. As shown in Figure 4.20, the shape of the latter function is narrower. This feature leads not only to essential reduction of the sidelobes height, but also increases the number of waveforms producing ACF whose sidelobes are lowered below the desired threshold level.

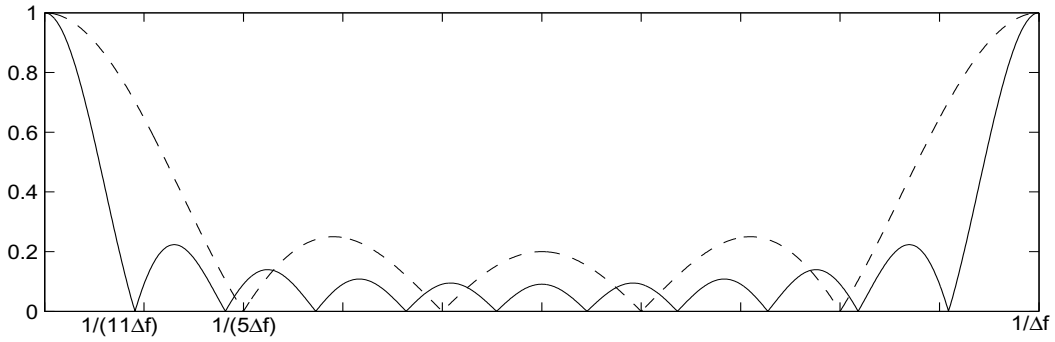

Figure 4.20: The shape of periodic sinc function $\sin(N\pi\Delta f\tau)/(N\sin(\pi\Delta f\tau))$ for $N = 11$ (solid) and $N = 5$ (dotted). (Zoom on a period of the function.)

Figures 4.21-4.23 illustrate the above remarks. For instance, comparing the top subplots of Figures 4.15 and 4.21, one can see that the number of waveforms whose PSL is less than -40dB is much greater in the case of 77 pulse trains. As follows from the bottom subplot of Figure 4.21, this number drops significantly if we set a new threshold level to -45dB. (The matched filter response for one of the waveforms satisfying this criteria is shown in Figure 4.23.) It can be also noticed from the above figures that the waveform's length does not affect the structure of $\Omega_{(n,m)}^{(\mu_1,\mu_2)}$. In particular, it means that, for each $\Delta f_{in} t_p$, there are possibilities to choose the

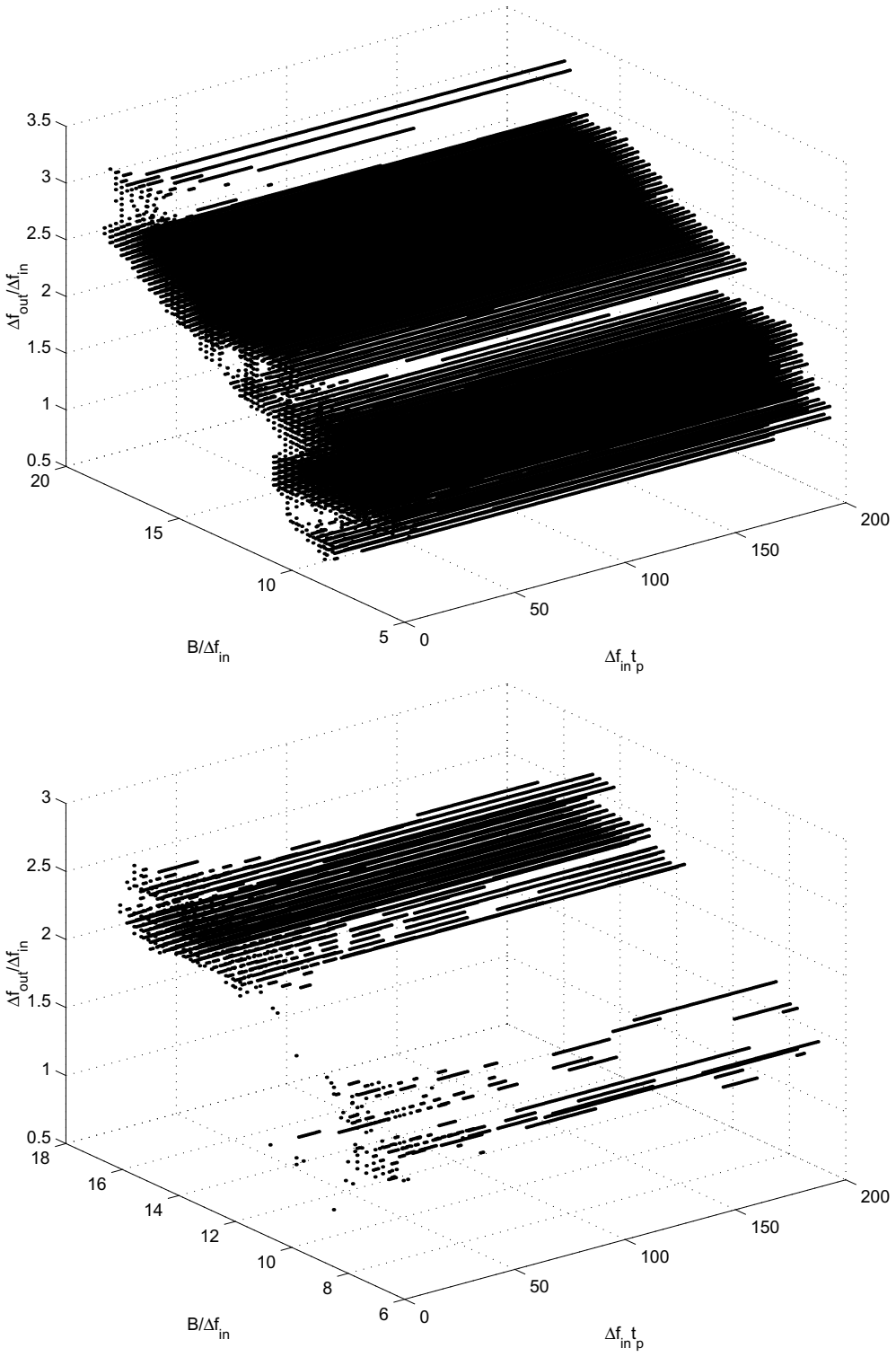

Figure 4.21: Pictorial representation of $\Omega^{(-40)}_{(11,7)}$ (top) and $\Omega^{(-45)}_{(11,7)}$ (middle).

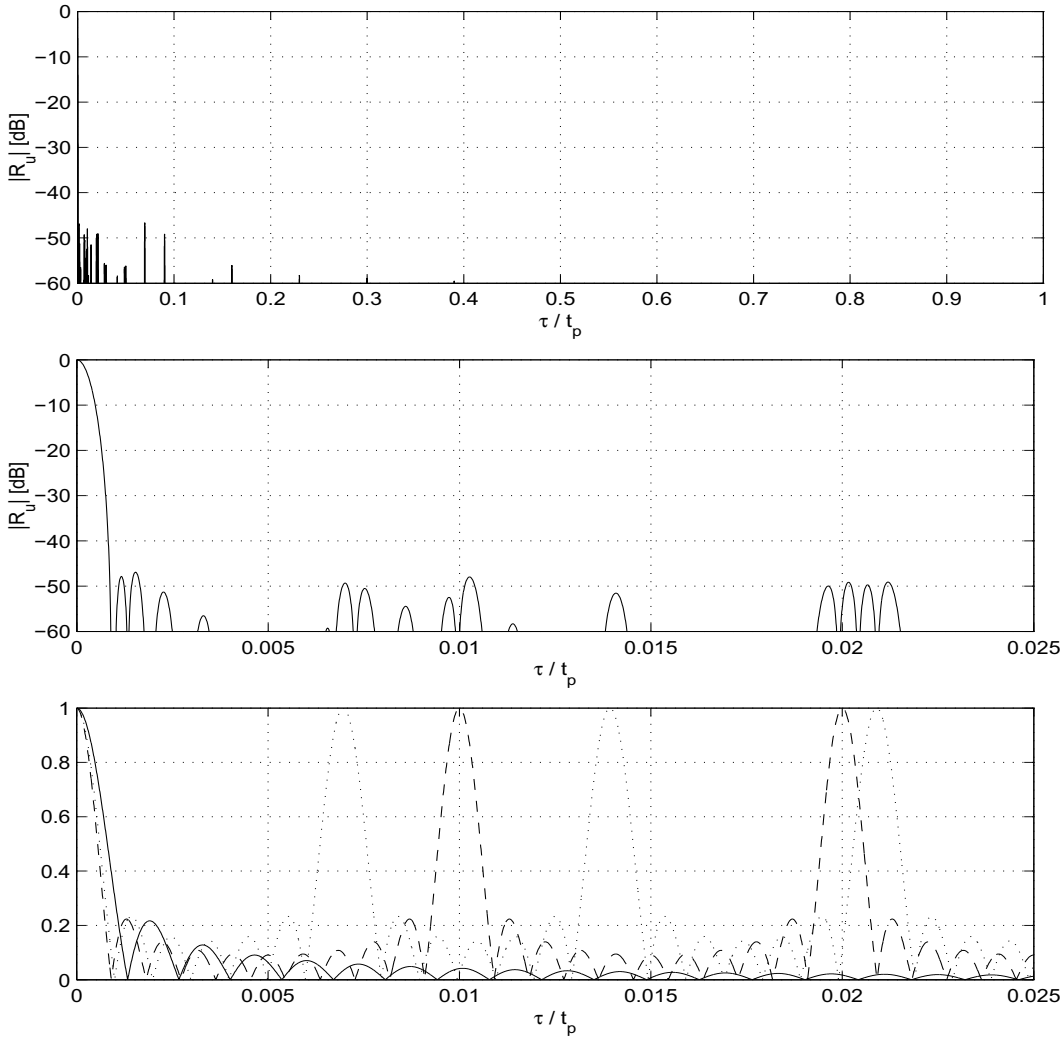

Figure 4.22: Partial ACF of $u(t)$ with $N = 11, M = 7$, $\Delta f_{in} t_p = 100, \Delta f_{out} t_p = 143.56$, and $Bt_p = 750$. Top: zoom on the interval $0 \leq \tau/t_p \leq 1$. Middle: zoom on the interval $0 \leq \tau/t_p \leq 0.025$. Bottom: the relationship between $|R_1(\tau)|$ (solid), $|R_2(\tau)|$ (dashed), and $|R_3(\tau)|$ (dotted).

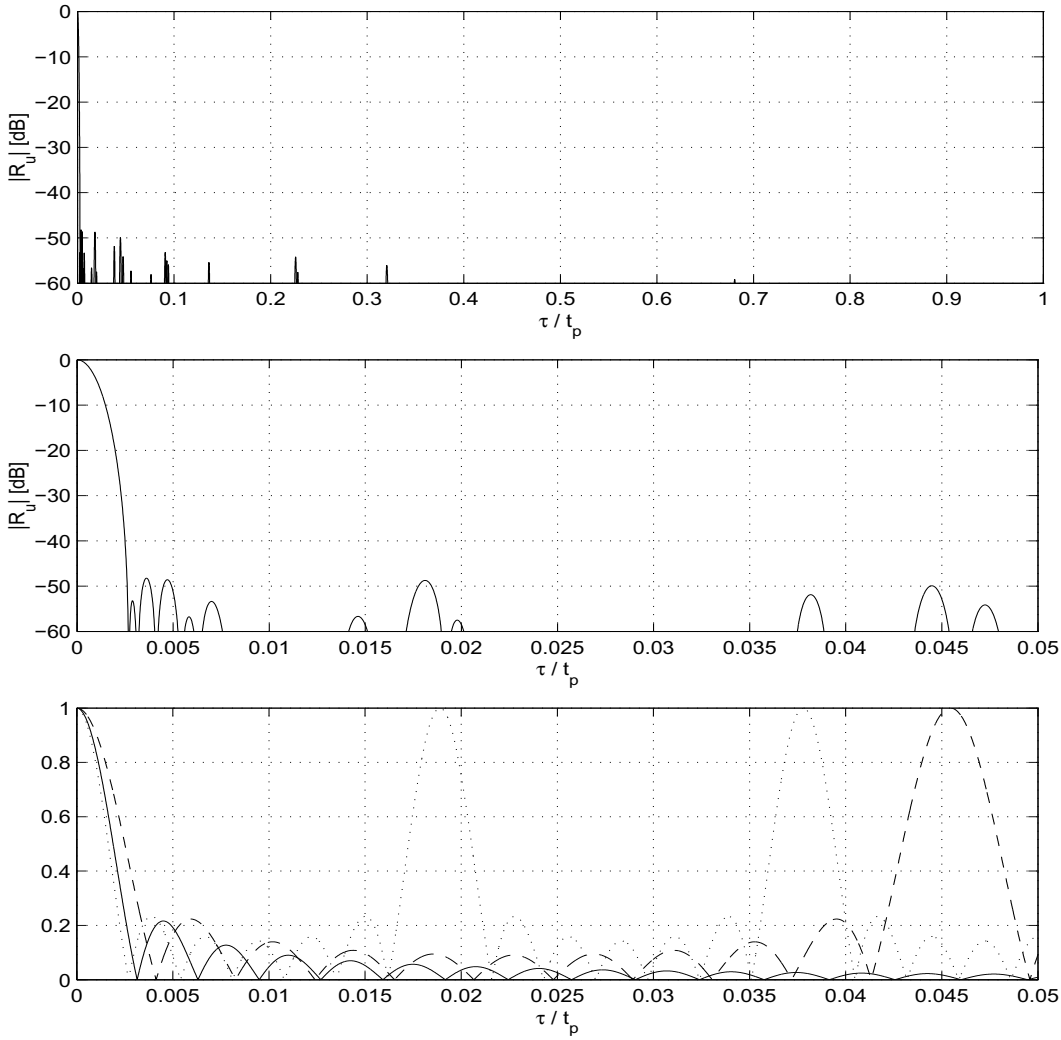

Figure 4.23: Partial ACF of $u(t)$ with $N = 11, M = 7$, $\Delta f_{in} t_p = 22, \Delta f_{out} t_p = 52.92$, and $Bt_p = 319$. Top: zoom on the interval $0 \leq \tau/t_p \leq 1$. Middle: zoom on the interval $0 \leq \tau/t_p \leq 0.05$. Bottom: the relationship between $|R_1(\tau)|$ (solid), $|R_2(\tau)|$ (dashed), and $|R_3(\tau)|$ (dotted).

N	M	$\Delta f_{in}t_p$	$\Delta f_{out}t_p$	Bt_p	$B_{total}t_p$	PSL, dB	τ^{null}
11	7	22	52.92	319	856.5	-48.22	0.0027
11	7	38	91.41	551	1479.5	-48.13	0.0016
11	7	48	115.09	684	1854.5	-48.22	0.0012
11	7	68	163.58	986	2647.5	-48.07	0.0009
11	7	83	199.66	1203.5	3231.5	-48.06	0.0007
11	7	108	258.95	1539	4172.7	-48.28	0.0006

Table 4.2: Examples of waveforms with the parameters belonging to $\Omega^{(-48)}_{(11,7)}$.

other parameters (i.e. Bt_p and $\Delta f_{out}t_p$) such that the resulting waveform would have a desired PSL. Finally, Table 4.2 contains samples from a numerical search for waveforms whose peaks are reduced to -48dB level. This is the best level of sidelobe suppression that can be achieved by waveforms consisting of 77 pulses. The ACF produced by one of those waveforms listed in the Table 4.2 is depicted in Figure 4.23.

4.4 Family of pulse trains having the same auto-correlation function over $|\tau| \leq t_p$

As can be noticed from the previous discussion, large time gaps between "outer" pulses in train (4.10) make the total time duration of the waveform to be relatively long (compared with "ordinary" train (3.8)). This fact should be considered as a disadvantage of the train (4.10). Below we show how this problem can be resolved.

LEMMA 4.4.1 *Let $s_0(t), s_1(t), \ldots, s_{N-1}(t)$ be arbitrary pulses, each of duration t_p.*

Then, the autocorrelation function of the waveform

$$u(t) = \sum_{n=0}^{N-1} s_n \left(t - \sum_{i=0}^{n} T_i \right) \tag{4.46}$$

(here $T_0 = 0, T_i \geq 2t_p (k = 1, 2, \ldots, N-1)$) can be represented, for $|\tau| \leq t_p$, as

$$R_u(\tau) = \sum_{n=0}^{N-1} R_{s_n}(\tau), \tag{4.47}$$

where $R_{s_n}(\tau)$ is the autocorrelation function of pulse $s_n(t)$.

PROOF. For our convenience, we use the following notation: $\widetilde{T}_n = \sum_{i=0}^{n} T_i$. Now, we can write

$$R_u(\tau) = \sum_{n=0}^{N-1} \sum_{m=0}^{N-1} \int_{-\infty}^{\infty} s_n \left(t - \widetilde{T}_n - \frac{\tau}{2} \right) \overline{s_m \left(t - \widetilde{T}_m + \frac{\tau}{2} \right)} \, dt. \tag{4.48}$$

For each integral in the double sum (4.48), we perform the change of variable $t = t_1 + \frac{\widetilde{T}_n + \widetilde{T}_m}{2}$. As the result, we obtain

$$R_u(\tau) = \sum_{n=0}^{N-1} \sum_{m=0}^{N-1} \int_{-\infty}^{\infty} s_n \left(t_1 - \frac{\tau + \widetilde{T}_n - \widetilde{T}_m}{2} \right) \overline{s_m \left(t_1 + \frac{\tau + \widetilde{T}_n - \widetilde{T}_m}{2} \right)} \, dt_1.$$

Note that the cross-correlation function of pulses $s_n(t)$ and $s_m(t)$ has the form

$$R_{s_n, s_m}(\tau) = \int_{-\infty}^{\infty} s_n \left(t - \frac{\tau}{2} \right) \overline{s_m \left(t + \frac{\tau}{2} \right)} \, dt.$$

Hence, $R_u(\tau) = \sum_{n=0}^{N-1} \sum_{m=0}^{N-1} R_{s_n, s_m}(\tau + \widetilde{T}_n - \widetilde{T}_m)$.

At last, we observe that $R_{s_n, s_m}(\tau)$ vanishes outside the interval $|\tau| \leq t_p$, since the time duration of both pulses $s_n(t)$ and $s_m(t)$ is t_p. It is also evident that, if $n \neq m$, $|\widetilde{T}_n - \widetilde{T}_m| = \left| \sum_{i=\min\{n,m\}+1}^{\max\{n,m\}} T_i \right| \geq 2t_p$. Therefore, for $|\tau| \leq t_p$ and $n \neq m$, $R_{s_n, s_m}(\tau + \widetilde{T}_n - \widetilde{T}_m) = 0$. The last implies the correctness of (4.47).

Lemma 4.4.1 leads to the following important result.

COROLLARY 4.4.1 *Let* $S(t) = \{s_0(t), s_1(t), \ldots, s_{N-1}(t)\}$ *be a sequence of arbitrary pulses, each of duration* t_p, *and* $\widetilde{S}(t) = \{\widetilde{s}_0(t), \widetilde{s}_1(t), \ldots, \widetilde{s}_{N-1}(t)\}$ *be other sequence of pulses obtained by permutation of the elements of* $S(t)$. *Let also* $\{T_i^{(k)}\}_{i=0}^{N-1} (k = 1, 2)$ *be a sequence of real numbers satisfying* $T_0^{(k)} = 0$ *and* $T_i^{(k)} \geq 2t_p (i = 1, 2, \ldots, N-1)$. *Then, the autocorrelation functions of the trains*

$$u_1(t) = \sum_{n=0}^{N-1} s_n \left(t - \sum_{i=0}^{n} T_i^{(1)} \right) \qquad \textit{and} \qquad u_2(t) = \sum_{n=0}^{N-1} \widetilde{s}_n \left(t - \sum_{i=0}^{n} T_i^{(2)} \right)$$

coincide over $|\tau| \leq t_p$.

The above corollary gives us a powerful way to construct a variety of stepped-frequency waveforms having desired autocorrelation shape. Indeed, when (by applying the algorithm described in Section 4.1) at least one such waveform $u(t)$ has been found, we can obtain others by changing the time repetition intervals between consecutive subpulses and/or permuting their order. In particular, we can choose all the time gaps between the subpulses to be the same. This leads to waveforms with uniform time gapping and nonuniform frequency stepping.

Figure 4.24 illustrates the procedure described above. It shows the time-frequency distribution of three stepped-frequency trains whose autocorrelation functions coincide along $|\tau| \leq t_p$. The top subplot displays a nine pulse train $u(t)$ designed in accordance with the scheme we have proposed in Section 4.1. The middle subplot the waveform $\widetilde{u}(t)$ obtained from $u(t)$ by reducing the large time gaps between "outer" trains. The waveform $\widetilde{u}(t)$ has the same time repetition interval t_r between all the consecutive subpulses (i.e., it is a uniform pulse train). Note that such transformation of $u(t)$ reduces its total time duration from $2T_r + T_p$ (which is greater than $5T_p = 5(t_p + 2t_r)$) to $8t_r + t_p$. The bottom subplot contains a train $\widehat{u}(t)$ that can be obtained from the $\widetilde{u}(t)$ by changing the order of the subpulses in $\widetilde{u}(t)$ so that their frequency shifts are sorted in increasing order (in our example it means changing

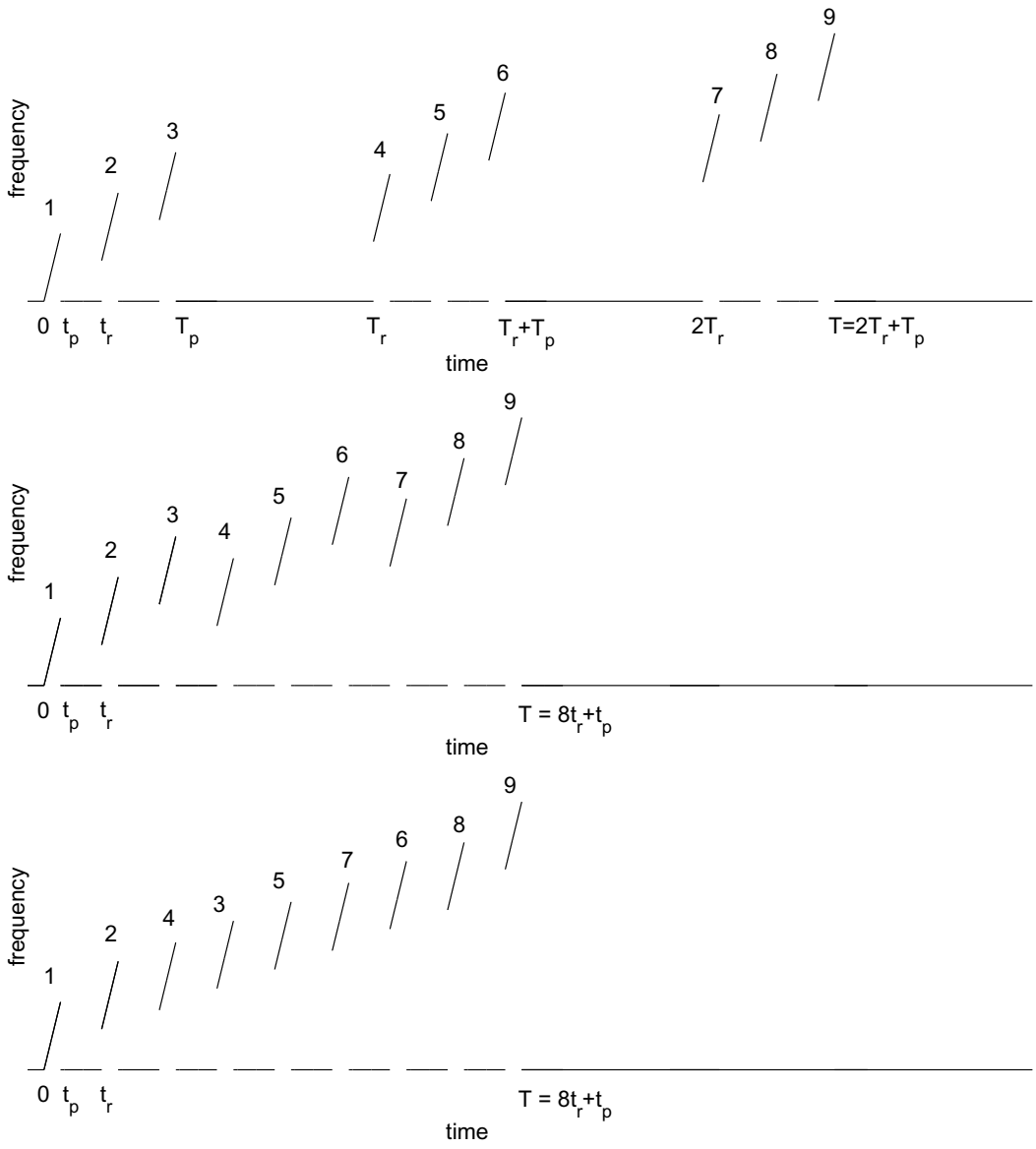

Figure 4.24: Stepped-frequency LFM trains producing the same autocorrelation function for $|\tau| \leq t_p$

the order of the subpulses from $\{1,2,3,4,5,6,7,8,9\}$ to $\{1,2,4,3,5,7,6,8,9\}$). As a consequence, $\widehat{u}(t)$ is a uniform pulse train with nonlinear frequency shifts between subpulses. Finally, we note that, according to the previous discussion, the ACFs of stepped-frequency waveforms $u(t), \widetilde{u}(t)$, and $\widehat{u}(t)$ coincide along $|\tau| \leq t_p$. Hence, if $u(t)$ has been designed to have a low peak sidelobe level (PSL), then $\widehat{u}(t)$ would as well. Thus, we have achieved our goal to design stepped-frequency LFM pulse trains with good range resolution capabilities.

4.5 Proposed waveform vs. traditional stepped-frequency train

In this section we compare the performance of waveforms obtained by using our approach and traditional stepped-frequency trains (see section 3.7).

The top subplots of Figures 4.25 and 4.26 display the time-frequency evolution of two different stepped-frequency trains consisting of 35 and 55 LFM pulses, respectively. In both cases, we have applied our algorithm to generate nonlinear-FM-like waveforms described in section 4.1. Then we have eliminated large time gaps between inner subtrains as proposed in section 4.4 so that the waveforms depicted have constant pulse repetition intervals. To demonstrate the benefits of those waveforms we have constructed corresponding traditional stepped-frequency trains (see the middle subplots of Figures 4.25 and 4.26) with the same number of pulses NM, pulse duration t_p, pulse repetition interval t_r, instantaneous bandwidth B, and total processing band B_{total}. For convenience, we denote nonlinear-like waveforms by $u(t)$ and traditional trains by $u^*(t)$. The constant frequency step Δf between the center frequencies of the consecutive subpulses in $u^*(t)$ is computed by

$$\Delta f = [(M-1)\Delta f_2 + (N-1)\Delta f_1]/(MN-1). \tag{4.49}$$

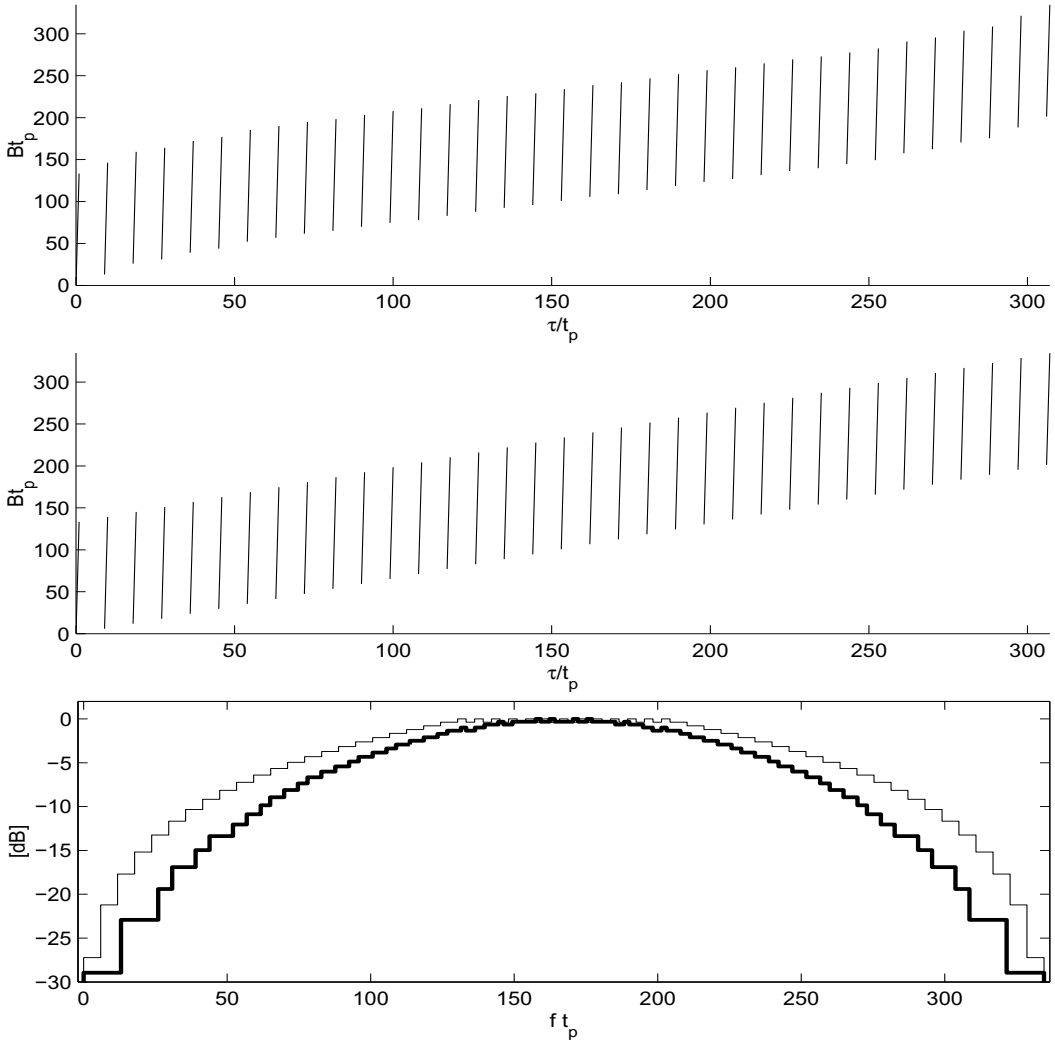

Figure 4.25: Top and middle: Frequency evolution of uniform stepped-frequency trains consisting of 35 LFM pulses with $Bt_p = 133.25$ and $t_r/t_p = 9$ (top: nonlinear frequency stepping, $N = 7, M = 5, \Delta f_1 t_p = 13, \Delta f_2 t_p = 30.836$; middle: linear frequency stepping, $\Delta f t_p = 5.9219$). Bottom: Normalized energy distribution of both waveforms (bold line represents waveform with nonlinear stepping).

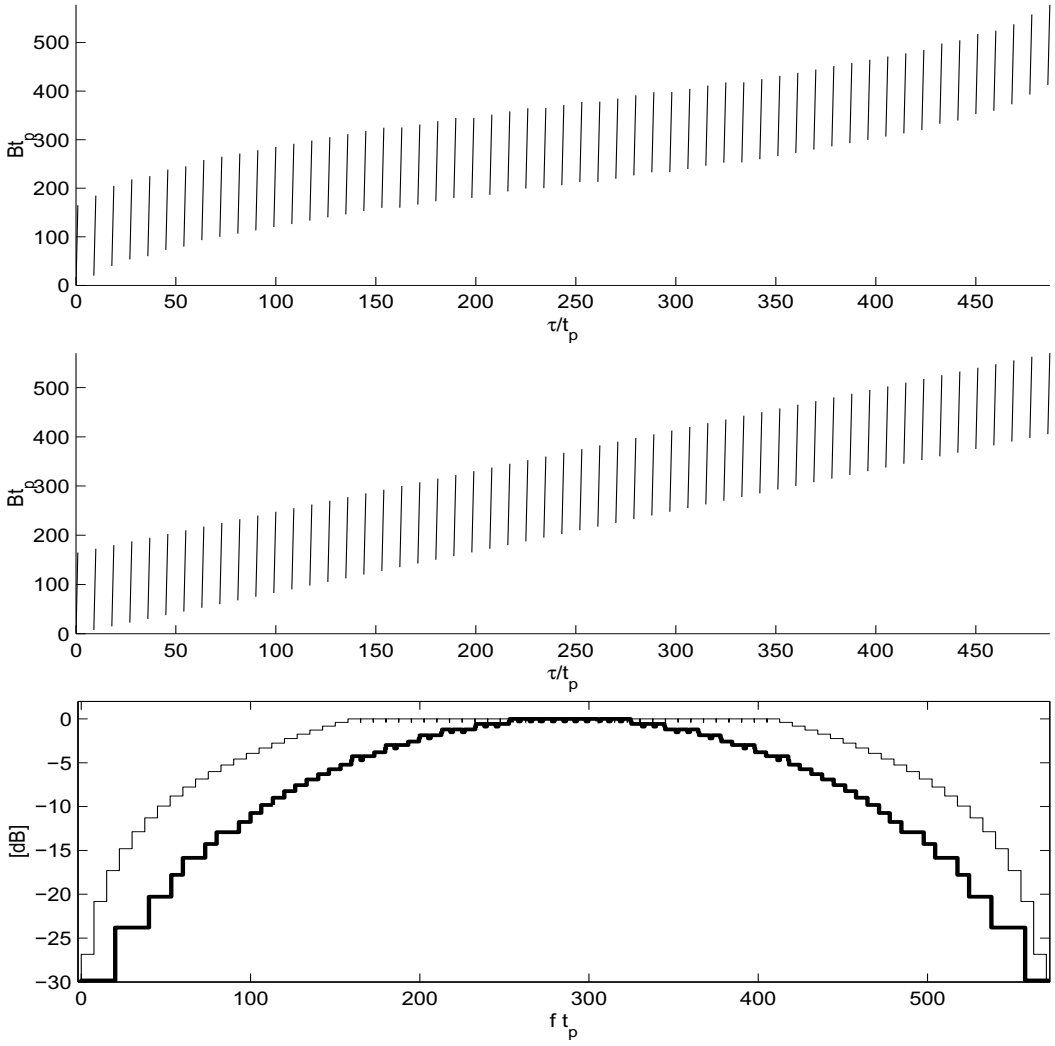

Figure 4.26: Top and middle: Frequency evolution of uniform stepped-frequency trains consisting of 55 LFM pulses with $Bt_p = 165$ and $t_r/t_p = 9$ (top: nonlinear frequency stepping, $N = 11, M = 5, \Delta f_1 t_p = 20, \Delta f_2 t_p = 53.184$; middle: linear frequency stepping, $\Delta f t_p = 7.5043$). Bottom: Normalized energy distribution of both waveforms (bold line represents waveform with nonlinear stepping).

The bottom plots of Figures 4.25 and 4.26 show normalized energy distributions of $u(t)$ and $u^*(t)$ under the assumption that each component pulse constituting both trains has a rectangular spectrum. As can be seen from the plots, a right choice of the frequency shifts between pulses allows one to reshape the wavefrom's spectrum, creating a weighting in the frequency domain. The number of pulses to be processed controls the quality of such reshaping. Similar to the known weightings, introducing nonlinearity in frequency stepping causes energy concentration in the middle frequencies. This, in turn, leads to reduction of the autocorrelation sidelobe peaks (the ACF for the waveforms given in Figures 4.25 and 4.26 is drawn in Figures 4.27 and 4.28, respectively). Note that since in both examples the frequency overlap ratio $B/\Delta f$ (computed for traditional waveforms $u^*(t)$) is large (22.5 and 22, respectively), all the grating lobes of $|R_{u^*}(\tau)|$ are already lowered below -40dB in Figure 4.27 and -45dB in Figure 4.28, and only suppression of a few near-source sidelobes is required. This can be done by using nonlinear-FM-like waveforms displayed in Figures 4.25 and 4.26. They reduce the PSL by about -14dB and -28dB, respectively.

We also observe that in both cases traditional trains provide better capabilities to resolve targets. This remains correct for all the pairs of $u(t)$ and $u^*(t)$ having the same parameters and small overlap ratios. Indeed, it follows from (4.40) and (4.49) that, in this case, τ^{null} is always greater than the first null of $u^*(t)$ which is located at the point $1/(NM\Delta f)$. There is no surprise in this result, since it reflects well-known trade-off: the PSL reduction is always associated with losses in resolution. To further examine this phenomena with respect to the family of trains under consideration, we have applied the Hamming interpulse amplitude weighting (as described in [22]) to the traditional burst $u^*(t)$ shown in Figure 4.25 and compared its performance with "natural" frequency weighting we have created by means of nonlinear stepping.

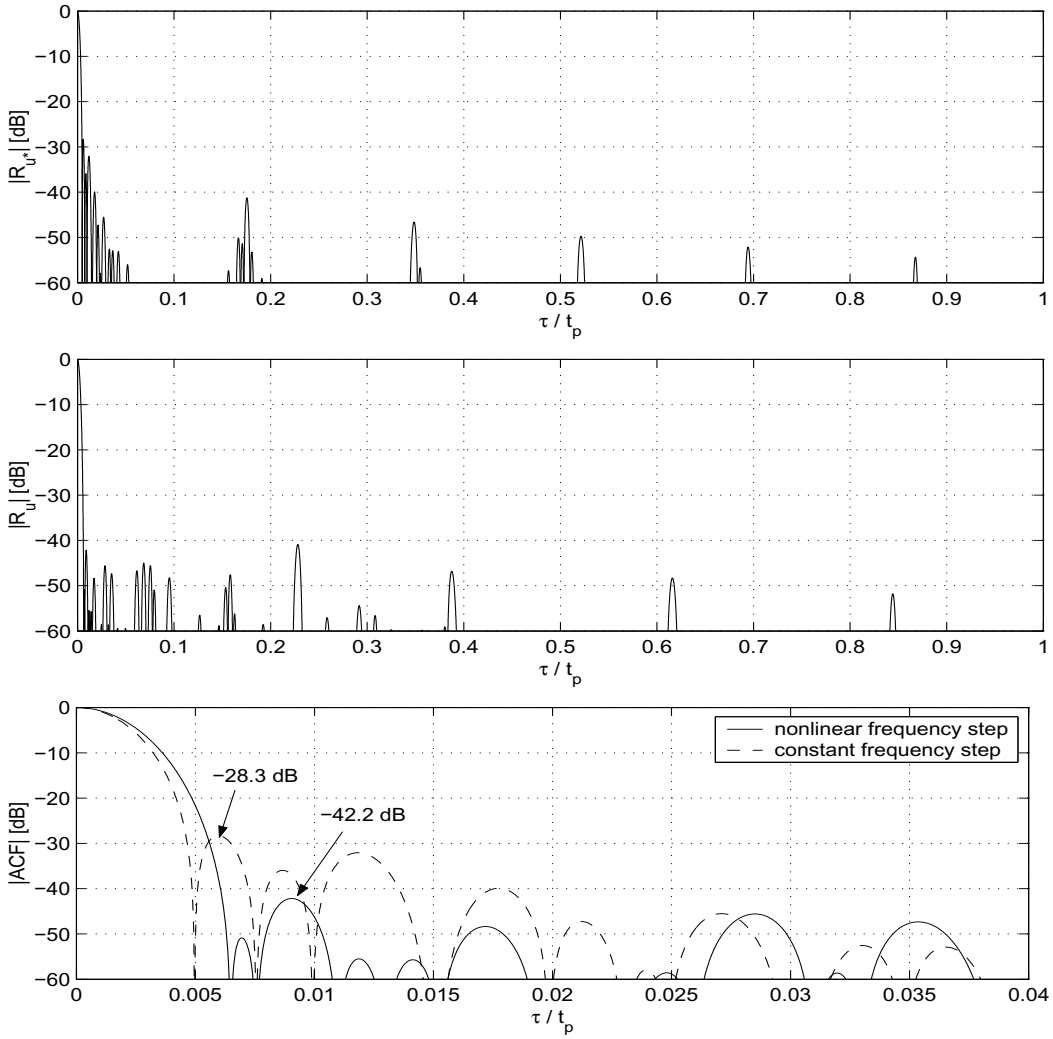

Figure 4.27: Top and middle: The ACF of the waveforms depicted in the top and middle subplots of Figure 4.25, respectively (zoom on $0 \leq \tau/t_p \leq 1$). Bottom: The same ACFs zoomed on $0 \leq \tau/t_p \leq 0.04$.

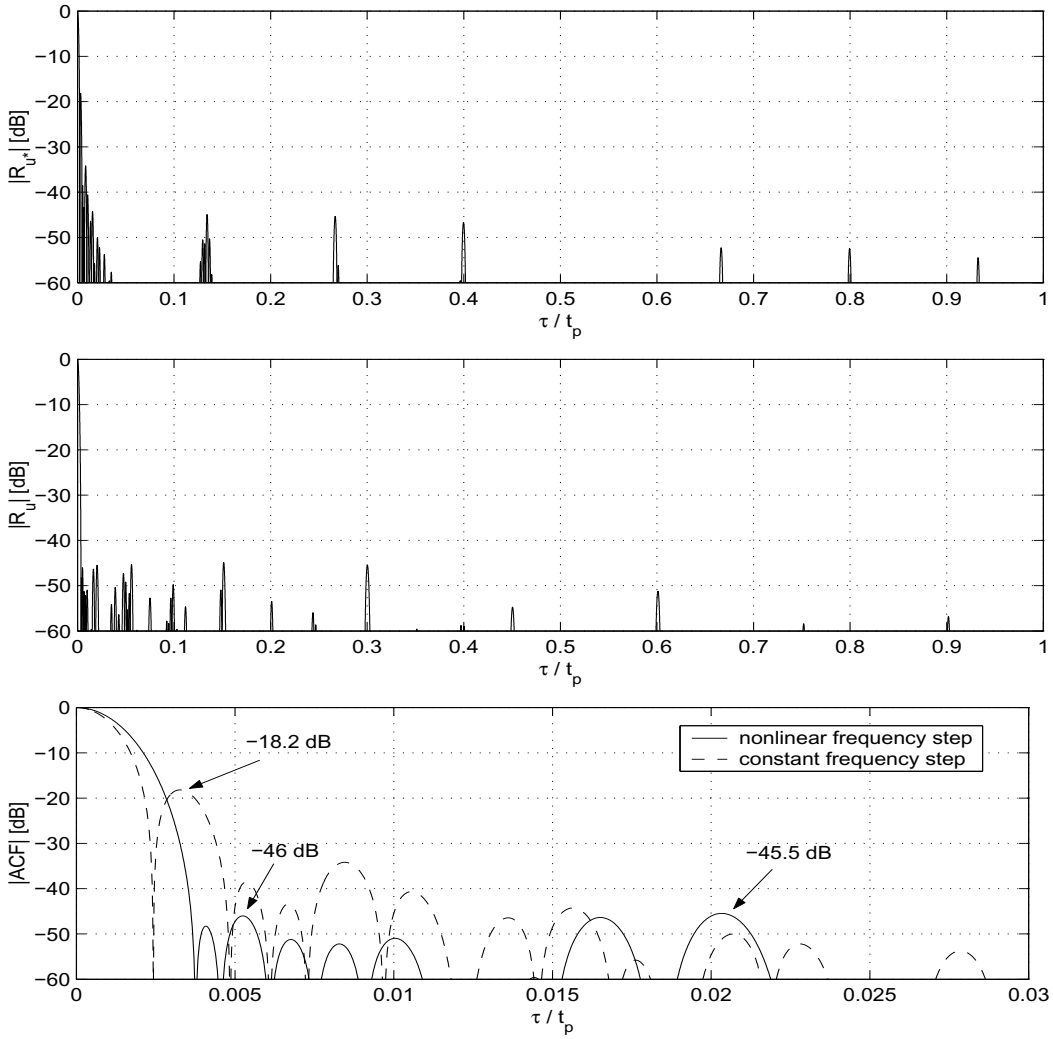

Figure 4.28: Top and middle: The ACF of the waveforms depicted in the top and middle subplots of Figure 4.26, respectively (zoom on $0 \leq \tau/t_p \leq 1$). Bottom: The same ACFs zoomed on $0 \leq \tau/t_p \leq 0.03$.

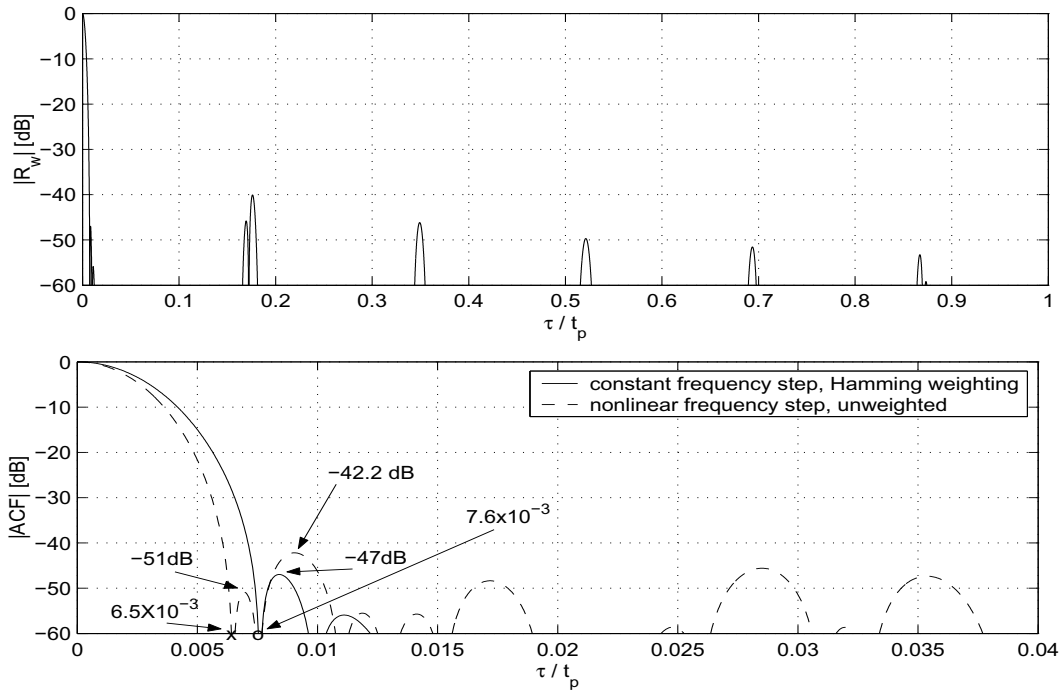

Figure 4.29: Top: The ACF of weighted traditional stepped-frequency waveform depicted in the middle subplot of Figure 4.25, amplitude weighting with Hamming window (zoom on $0 \leq \tau/t_p \leq 1$). Bottom: The same ACF vs. the ACF of the waveform shown in the top subplot of Figure 4.25 (zoom on $0 \leq \tau/t_p \leq 0.04$).

As follows from Figure 4.29, the amplitude weighting results in much better sidelobe suppression: the PSL drops to -45.5dB. However, it leads to undesirable losses in resolution that can be softened by the usage of the proposed waveform $u(t)$. Finally, we would like to point out other advantage of the "built-in" weighting we have proposed: it allows one to completely avoid heavy SNR losses inherent in weighted filters.

Summarizing the results of this section, we conclude that proposed waveforms exhibit improved performance compared with traditional approaches.

4.6 Sidelobe suppression for extended Doppler

In this section we investigate the behavior of the central part of the AF of $u(t)$ and compare it with the AF of traditional stepped-frequency waveform.

It follows from (4.28) that the central envelope of $|\chi_u(\tau,\nu)|$ is defined by

$$|\chi_u(\tau,\nu)| = |\chi_1(\tau,\nu)| \cdot |\chi_2(\tau,\nu)| \cdot |\chi_3(\tau,\nu)|, \qquad |\tau| \le t_p, \tag{4.50}$$

where

$$|\chi_1(\tau,\nu)| = \left| \left(1 - \frac{|\tau|}{t_p}\right) \operatorname{sinc}\left[t_p\left(\nu - B\tau\right)\left(1 - \frac{|\tau|}{t_p}\right)\right] \right|, \tag{4.51}$$

$$|\chi_2(\tau,\nu)| = \left| \frac{\sin\left[N\pi(\nu t_r - \Delta f_{in}\tau)\right]}{N\sin\left[\pi(\nu t_r - \Delta f_{in}\tau)\right]} \right|, \tag{4.52}$$

$$|\chi_3(\tau,\nu)| = \left| \frac{\sin\left[M\pi(\nu T_r - \Delta f_{out}\tau)\right]}{M\sin\left[\pi(\nu T_r - \Delta f_{out}\tau)\right]} \right|. \tag{4.53}$$

As we already mentioned before, the first factor in (4.50) represents the envelope of the AF of the repeated chirp pulse. Two other factors are caused by pulse repetition and have similar shapes: they both are two-dimensional periodic sinc functions. Note that $|\chi_i(\tau,\nu)|$ $(i = 2, 3)$ preserves its values along the line

$$\alpha_i\nu - \beta_i\tau = 0, \tag{4.54}$$

where $\alpha_2 = t_r, \alpha_3 = T_r, \beta_2 = \Delta f_{in}$, and $\beta_3 = \Delta f_{out}$. Hence, any cross-section $|\chi_i(\tau,\nu_*)|$ of $|\chi_i(\tau,\nu)|$ along $\nu = \nu_*$ is a shifted (along time-delay axis) version of $|R_i(\tau)|$, i.e.

$$|\chi_i(\tau,\nu_*)| = \left| R_i\left(\tau - \frac{\alpha_i}{\beta_i}\nu_*\right) \right|.$$

It also follows from the above observation that the ridges of $|R_i(\tau)|$ run parallel to the line (4.54). Note, however, that the shape of the product $|R_2(\tau)| \cdot |R_3(\tau)|$ is not preserved for non-zero Doppler shifts, since the factors have different directions of propagation over the Euclidean plane. Therefore, in general, we have to expect the presence of relatively high peaks in the $|\chi(\tau,\nu_*)|$'s profile.

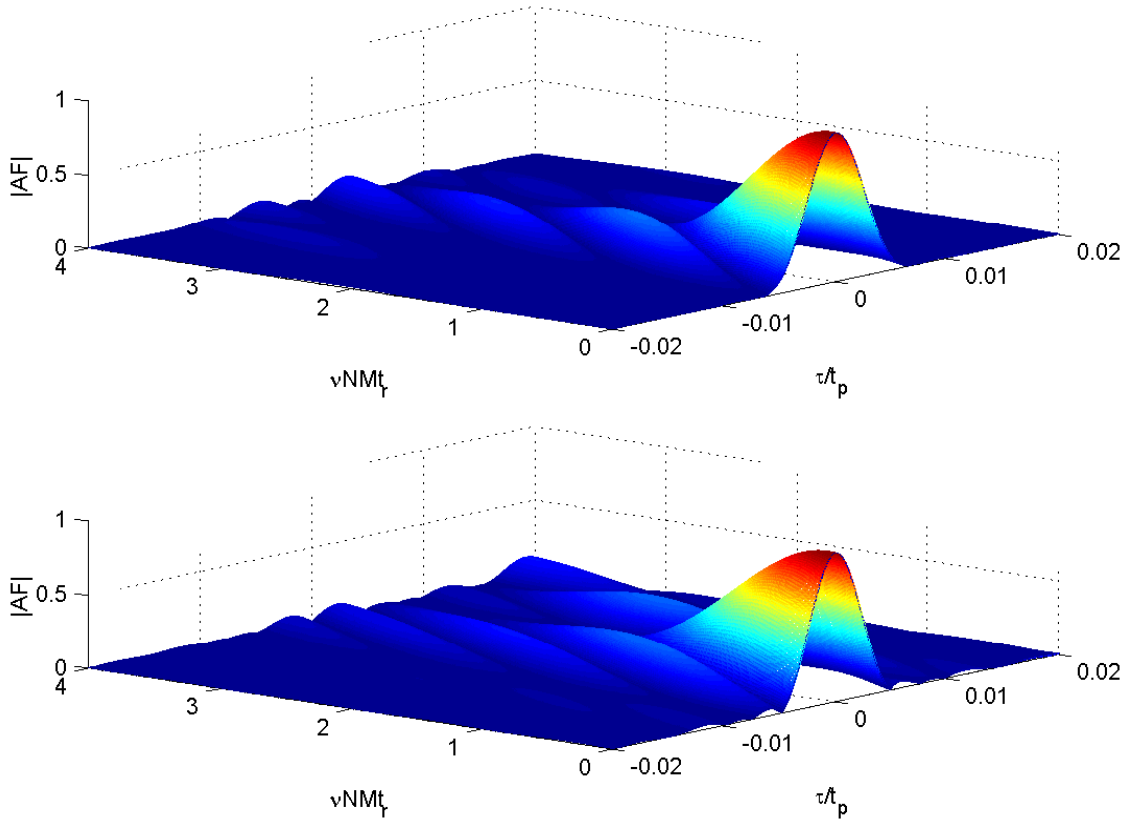

Figure 4.30: Partial AF of the nonlinear-FM-like waveform (4.10) with $N = 7, M = 5, \Delta f_1 t_p = 13, \Delta f_2 t_p = 30.836, Bt_p = 133.25$, and $t_r/t_p = 9$ (top) and corresponding traditional stepped-frequency waveform depicted in the middle subplot of Figure 4.25 (bottom). Zoom on the region $\{|\tau/t_p| \leq 0.02, 0 < \nu NMt_r < 4\}$.

The top subplot of Figure 4.30 illustrates the AF of the proposed waveform designed with $N = 7, M = 5, \Delta f_1 t_p = 13, \Delta f_2 t_p = 30.836, Bt_p = 133.25$, and $t_r/t_p = 9$. (Note that NMt_r, which normalizes the Doppler axis, is the entire duration of the waveform.) Note that the shape of the AF heavily depends on the order of subpulses in the train. This fact should be taken into account in order to obtain waveforms with low sidelobe level over some stripe containing the time-delay axis. The AF of the corresponding traditional stepped-frequency waveform is depicted in the bottom subplot of Figure 4.30.

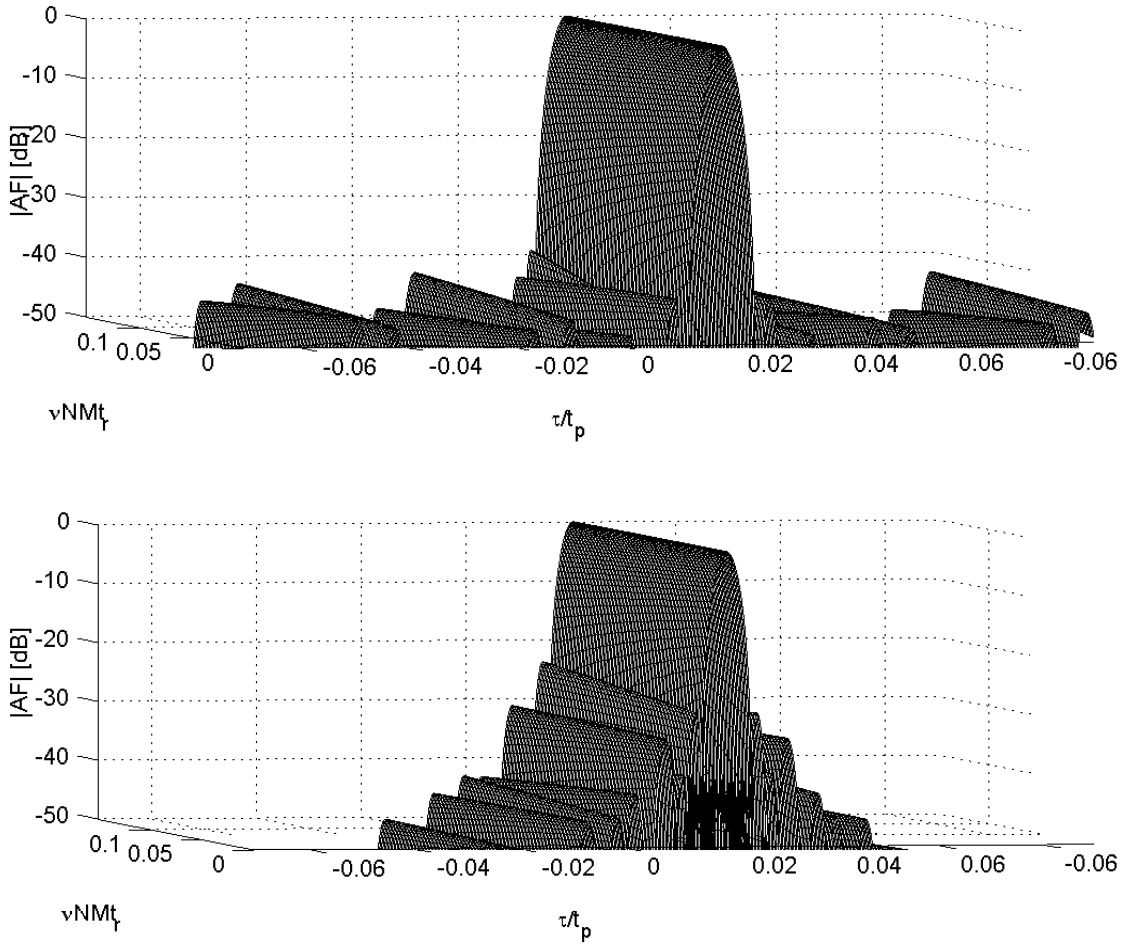

Figure 4.31: Zoomed on the region $\{|\tau/t_p| \leq 0.07, 0 < \nu NMt_r < 0.15\}$, AFs shown in Figure 4.30.

Figures 4.31 and 4.32 show that in both cases the sidelobes build-up with Doppler is relatively slow and the low sidelobe level associated with the ACF of the proposed nonlinear-FM-like waveform is effective for extended Doppler, as well. In particular, for $\nu NMt_r = 0.15$, its PSL = -39 dB (see Fig. 4.32). Hence, the proposed waveform allows us to achieve overall sidelobe suppression below -39dB over the stripe $\{(\tau, \nu) : |\tau/t_p| \leq 1, |\nu NMt_r| \leq 0.15\}$. Note that PSL produced by the traditional waveform is about -24dB. Thus, in some instances, proposed waveforms are Doppler tolerant and can be used to detect moving targets in the presence of unknown Doppler.

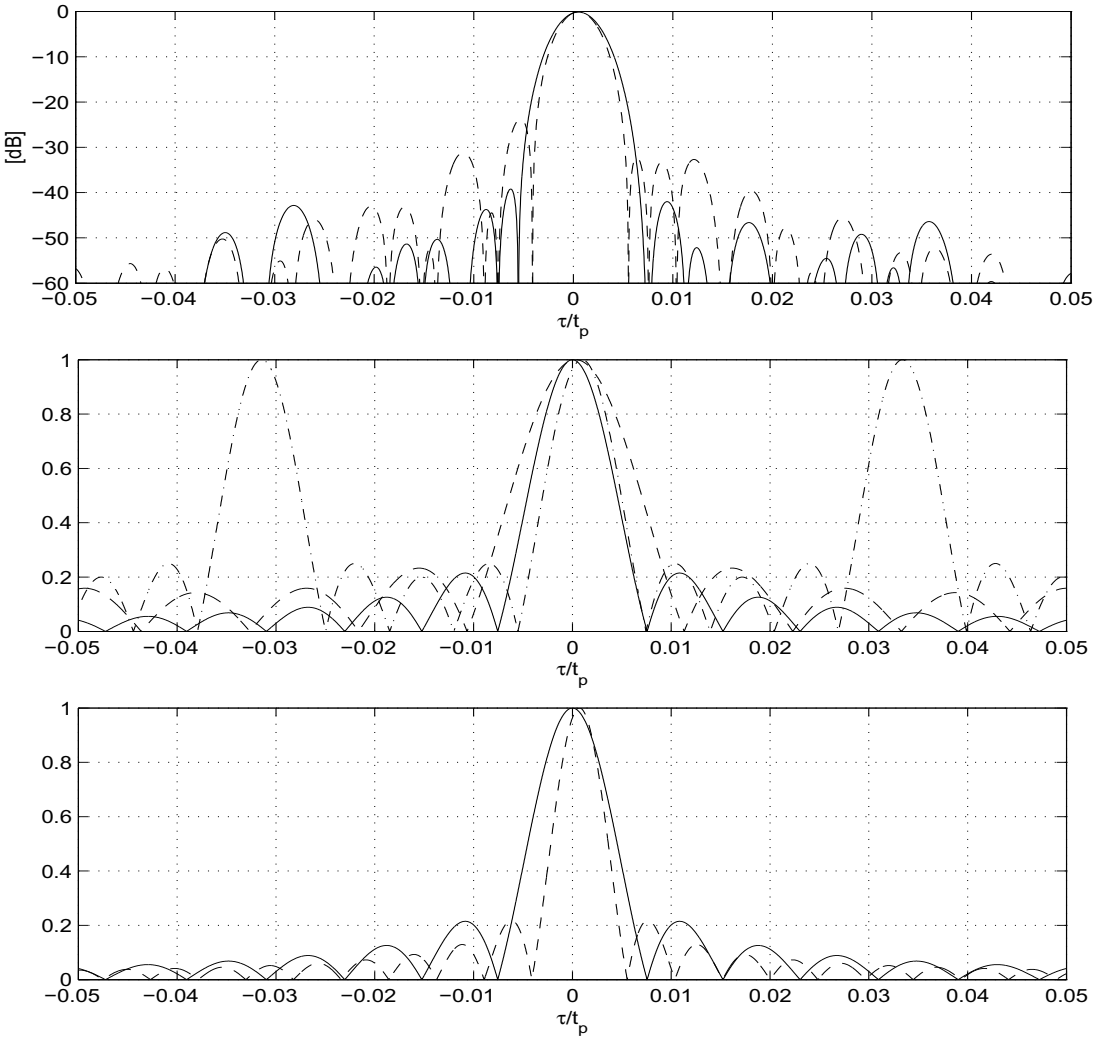

Figure 4.32: Top: Non-zero Doppler cut of the AFs depicted in the top (solid) and bottom (dash) subplots of Figure 4.30 for $\nu_* NMt_r$=0.15 (zoom on the interval $|\tau/t_p| \leq 0.05$). Middle: the relationship between the factors $|\chi_1(\tau, \nu_*)|$ (solid), $|\chi_2(\tau, \nu_*)|$ (dashed), and $|\chi_3(\tau, \nu_*)|$ (dotted) of the AF of the nonlinear waveform. Bottom: similar relationship between the factors of the AF of the corresponding traditional stepped-frequency train.

4.7 Summary and Further Work

In this chapter we have proposed a new family of waveforms that have been designed by a composition of two different stepped-frequency LFM trains with constant frequency steps between the center frequencies of the consecutive pulses. We have showed that, despite of the waveform's complicated structure, its AF (and, hence, ACF) could be written in the closed form. We have used this fact to perform a systematic analysis of the set of the waveform's parameter values, aimed to study their influence on the ACF shape. As the result, we have been able to find a large number of family members producing the ACF with excellent profiles. Our analysis clearly reveals that they have desirable built-in characteristics such as low range sidelobes and low grating lobes. Frequently, the low sidelobe level associated with the ACF of the proposed nonlinear-FM-like waveforms is effective for extended Doppler, as well. New waveforms are also shown to exhibit improved performance when compared with traditional stepped-frequency trains. The features of the proposed nonlinear waveforms we have mentioned above, along with the other advantages associated with the stepped-frequency waveforms, make them attractive for usage in a high range resolution radar.

The future work in this area can be done in studying more general stepped-frequency waveforms obtained from those ones we have proposed here by replacing the "innermost" chirp pulse by other (phase-coded, nonlinear-FM, etc.) signals and/or repeating the proposed design schema a few times. The later will increase the number of "nested" trains and, as consequence, will have additional factors in the factorization (4.34). In both cases, we introduce a new set of independent parameters that gives us possibility to control the sidelobe level better. As consequence, these waveforms are expected to provide excellent resolution capabilities.

Chapter 5

Conclusions

In this thesis, we have proposed new approaches for solving two challenging problems appearing in the radar waveform design: the problem of constructing waveforms with desired ambiguity characteristics in a chosen a priori region of the Euclidean plane and the problem of designing stepped-frequency waveforms with low sidelobes. In this chapter, we summarize our results.

Chapter 1: Introduction. Suitable waveform selection is an important problem in radar design, because it controls the resolution, clutter performance, and computational complexity of the processing. The ambiguity function of a transmitted signal measures the uncertainty with which the returning echo distinguishes, simultaneously, both ranges and velocities of a target system. Therefore, it is natural, to use the ambiguity function as a measure of performance in radar waveform design. In this chapter, we give alternative definitions of the ambiguity function and describe its meaning. We also provide a tidy set of interlocking properties of the ambiguity function. In general, it is unusual for an arbitrary two-dimensional function to satisfy these properties, and so, in a set of possible two-dimensional functions, ambiguity functions are very rare. We also introduce a theoretical concept of an

ideal ambiguity function, which would have ideal range-doppler characteristics, and describe its reasonable approximation – a "thumbtack" function.

Chapter 2: On the synthesis problem for a waveform having a desired ambiguity profile. In radar design problems, one has a pretty good idea of the desired ambiguity surface and wishes to work backwards to find a corresponding waveform. This, however, is an unsolved problem: no techniques are known for finding a waveform corresponding to a desired ambiguity surface, nor is a set of rules known for ensuring that a desired surface is in fact an ambiguity surface; a waveform that gives rise to this desired surface might not exist. Nevertheless there might be a waveform with ambiguity surface that is an acceptable approximation to the desired surface.

In this chapter, we investigate the problem of an approximation of an arbitrary two-dimensional square-integrable function by ambiguity functions. We first recall the fundamental results in this area obtained by Calvin Wilcox. In report [41], he presented a mathematically complete solution to this challenging problem, provided that the desired ambiguity shape is given in analytical form. It is, however, not the case in any practical radar application. In practice, engineers have a general idea of acceptable shape rather than the formulas describing it, thus making Wilcox's algorithm not applicable. Moreover, in many situations, it is not even necessary to have a certain shape for all the values of time and doppler delays (the region where the ambiguity surface is desired to be small depends on the particular radar application), and Wilcox's algorithm does not treat the situations where only part of the ambiguity surface has to be approximated.

Next, we introduce our model of a radar waveform which extends the Wilcox's model and formulate the problem of producing a close match, over a specified subregion of $\mathbb{R}^2$, to a good ambiguity surface. Our formulation is based on the projection

of the signal onto an appropriate orthonormal basis in the space of radar waveforms and approximating the signal with desired ambiguity properties by a finite number of basis waveforms. The optimization over a subregion of $\mathbb{R}^2$ generalizes Wilcox's approach. There are new subtleties that appear with this approach, since we can seek, for example, to make an ambiguity small over some region, which, if successful, will push the bulk of the function outside the region where we want it to be small. Obviously, this is not possible if the region is all of $\mathbb{R}^2$, because of the volume property of the ambiguity function.

Finally, we investigate this new problem in the special case, when the function to be approximated is the ideal ambiguity function. We analyze our problem for the case of the specific orthonormal basis formed by well-known Hermite waveforms and the specific class of regions having circular symmetry. In particular, we find the conditions

Chapter 3: Radar signals. In this chapter we present an overview of some known classes of radar waveforms and their ambiguity/autocorrelation function. We start with an unmodulated pulse which is a basic radar signal. Then, we describe pulse compression techniques (e.g., phase coding, LFM) which produce "thumbtack"-like profile of the matched filter response. We also mention basic approaches for designing pulse trains – long duration signals generated by periodically repeating a suitable short duration pulses. We describe advantages and drawbacks of an important class of pulse trains – a family of stepped-frequency LFM pulse trains with constant frequency steps between the center frequencies of the subpulses.

Chapter 4: Sidelobe suppression in the stepped-frequency train of LFM pulses. For purposes of a high range resolution radar, it is desirable to transmit signals with wide overall bandwidth. Frequency stepping is one of the known and

well-studied techniques that can be used to achieve this goal. A stepped-frequency waveform is a collection of short narrowband pulses separated by time intervals that are sufficient to receive scattering echoes from the targets located at some range of interest. The center frequencies of the pulses forming the waveform are shifted with respect to each other. This leads to essential broadening of the waveform's total bandwidth.

A stepped-frequency waveform can be processed using a matched filter. It is well-known that the resulting autocorrelation function (ACF) suffers from relatively high delay sidelobes. In this chapter, we propose a new algorithm for designing stepped-frequency waveforms with nonlinear frequency stepping that would have a low level of autocorrelation sidelobes. We suggest specific relationships between the center frequencies of the subpulses constituting the waveform that allow us to derive the waveform's ambiguity function (and, hence, autocorrelation function) in the closed form. This gives us the possibility to search for waveforms with a desired threshold level by analyzing the set of their parameter values and, by doing so, to find a variety of desired waveforms. We also show that, frequently, the low sidelobe level associated with the ACF of the proposed nonlinear-FM-like waveforms is effective for extended Doppler, as well.

To illustrate the improvement that can be achieved by applying our approach, we compare the performance of waveforms we have derived with the performance of traditional stepped-frequency LFM trains with constant frequency steps between consecutive pulses. Our analysis reveals that the proposed waveforms have desirable built-in characteristics such as low range sidelobes and low grating lobes and allow to avoid undesirable SNR losses due to weighting on receive. These features, along with other advantages associated with stepped-frequency waveforms, make them attractive for usage in a high range resolution radar.

Appendix A

Proof of Theorem 2.5.1

In this appendix, we give the proof of Theorem 2.5.1. It consists of two parts. First, we prove the following lemma in section A.1.

LEMMA A.0.1 *Let N be a positive integer, R be a positive real number, G be a circular region:*

$$G = \{(\tau, \nu) : \tau^2 + \nu^2 \leq R^2\}, \tag{A.1}$$

and $\mathcal{W}_N = \mathcal{W}_N(\{u_i(t)\}_{i=0}^N)$ be a linear span of Hermite waveforms $u_i(t)$ $(i = 0, 1, \ldots, N)$, given by (2.6), with coefficients from N-dimensional unit sphere $\mathfrak{S}_N$ (see Definition 2.2.3). Then, a complex-valued vector $\widehat{\boldsymbol{a}} = (\widehat{a}_0, \widehat{a}_1, \ldots, \widehat{a}_N) \in \mathfrak{S}_N$ is a solution of the problem $\arg\min_{\boldsymbol{a}\in\mathfrak{S}_N} F(\boldsymbol{a})$, defined in section 2.5, if and only if a real-valued row-vector $\widehat{\boldsymbol{y}} = \left(\widehat{\boldsymbol{y}}^{(1)}, \widehat{\boldsymbol{y}}^{(2)}\right)$ with $\widehat{\boldsymbol{y}}^{(k)} = \left(\widehat{y}_0^{(k)}, \widehat{y}_1^{(k)}, \ldots, \widehat{y}_N^{(k)}\right)$ $(k = 1, 2)$, $\widehat{\boldsymbol{y}}^{(1)}\widehat{\boldsymbol{y}}^{(1)T} = 1$ and $\widehat{a}_i = \widehat{y}_i^{(1)} e^{j\widehat{y}_i^{(2)}}$ $(i = 0, 1, \ldots, N)$ is a solution of the problem

$$\arg\max_{\boldsymbol{y}^{(1)}\boldsymbol{y}^{(1)T}=1} G(\boldsymbol{y}), \tag{A.2}$$

where $\boldsymbol{y}$ is a (2N+2)-dimensional real-valued row-vector such that $\boldsymbol{y} = \left(\boldsymbol{y}^{(1)}, \boldsymbol{y}^{(2)}\right)$ with $\boldsymbol{y}^{(k)} = \left(y_0^{(k)}, y_1^{(k)}, \ldots, y_N^{(k)}\right)$ $(k = 1, 2)$, $G(\boldsymbol{y}) : \mathbb{R}^{2N+2} \to \mathbb{R}$ is the function given

by

$$G(\boldsymbol{y}) = \widetilde{\boldsymbol{y}}^{(1)}\Psi\widetilde{\boldsymbol{y}}^{(1)T} + 4\sum_{i=1}^{N-1}\sum_{k=0}^{i-1}\sum_{m=i+1}^{N}\psi_{ik(m-i)}y_i^{(1)}y_m^{(1)}y_k^{(1)}y_{k+m-i}^{(1)}\cos\left(y_m^{(2)} - y_i^{(2)} + y_{k+m-i}^{(2)} - y_k^{(2)}\right) \tag{A.3}$$

$\left(\textit{here } \widetilde{\boldsymbol{y}}^{(1)} = \left(\left(y_0^{(1)}\right)^2, \left(y_1^{(1)}\right)^2, \ldots, \left(y_N^{(1)}\right)^2\right)\right)$. *The elements of symmetric matrix* $\Psi = \{\psi_{ik}\}_{i,k=0}^{N}$ *and the coefficients* ψ_{ikq} *in* (A.3) *are computed by the formulas*

$$\psi_{ii} = \widetilde{\gamma}_{i0i0}, \qquad \psi_{ik} = \widetilde{\gamma}_{i0k0} + \widetilde{\gamma}_{i(k-i)i(k-i)} \tag{A.4}$$

$(i = 0, 1, \ldots, N; k = i+1, i+2, \ldots, N)$, *and* $\psi_{ikq} = \widetilde{\gamma}_{iqkq}$ $(i = 0, 1, \ldots, N; k = 0, 1, \ldots, i-1; q = 1, 2, \ldots, N)$, *respectively, where*

$$\widetilde{\gamma}_{iqkq} = \sqrt{\frac{i!k!}{(i+q)!(k+q)!}}\widetilde{\mu}_{iqkq} \tag{A.5}$$

and the quantities $\widetilde{\mu}_{iqkq}$ *are given by the following recurrence relations:*

$$\begin{aligned} x_0\widetilde{\mu}_{iqkq} = \Bigg(& x_0^q\left(L_i^{(q)}(x_0) - L_{(i-1)}^{(q)}(x_0)\right)\left(L_k^{(q)}(x_0) - L_{(k-1)}^{(q)}(x_0)\right) \\ & + \widetilde{\mu}_{(i-1)q(k-1)q} + q\widetilde{\mu}_{i(q-1)k(q-1)} - \frac{(i+q)!}{i!}\delta_{ik}\Bigg), \\ x_0\widetilde{\mu}_{i000} = & \left(L_i^{(0)}(x_0) - L_{(i-1)}^{(0)}(x_0) - \delta_{i0}\right). \end{aligned} \tag{A.6}$$

Here $x_0 = \pi R^2$, $L_i^{(q)}$ *is the Laguerre polynomial* (2.9), *and*

$$\delta_{ik} = \begin{cases} 1, & \textit{if } i = k, \\ 0, & \textit{otherwise.} \end{cases}$$

Based on Lemma A.0.1, we conclude that Problem 2.5.1 of minimizing $F(\mathbf{a})$ has a set of solutions $\widehat{\mathbf{a}} = (0, 0, \ldots, e^{j\phi})$ with arbitrary real ϕ if and only if the problem (A.2) of maximizing $G(\mathbf{y})$ admits solutions of the form $\widehat{\mathbf{y}} = (\widehat{\mathbf{y}}_1, \mathbf{y}_2)$, where $\widehat{\mathbf{y}}_1 = (0, 0, \ldots, 0, 1)$ and $\mathbf{y}_2$ is an arbitrary real-valued vector of length $N+1$. Therefore, to prove Theorem 2.5.1, we have to show the correctness of the following lemma.

LEMMA A.0.2 *If conditions* (2.24) *are fulfilled, then Problem* (A.2) *has a set of solutions of the form* $\widehat{\boldsymbol{y}} = (\widehat{\boldsymbol{y}}_1, \boldsymbol{y}_2)$*, where* $\widehat{\boldsymbol{y}}_1 = (0, 0, \ldots, 0, 1)$ *and* $\boldsymbol{y}_2$ *is an arbitrary real-valued vector of length* $N + 1$*.*

The proof of Lemma A.0.2 is given in Section A.2.

A.1 Proof of Lemma A.0.1

It follows from (2.23) that, for every signal $s(t) \in \mathcal{W}_N$, the volume under its ambiguity surface $|\chi_s(\tau, \nu)|$ can be expressed via the coefficients a_i $(i = 0, 1, \ldots, N)$ of expansion (2.17):

$$\|\chi_s(\tau, \nu)\|^2_{L^2(G)} = F(\mathbf{a}) = \sum_{i,k,m,n=0}^{N} c_{ikmn} a_i \overline{a}_k \overline{a}_m a_n, \tag{A.7}$$

where $\mathbf{a} = (a_0, a_1, \ldots, a_N), c_{ikmn} =< \xi_{ik}(\tau, \nu), \xi_{mn}(\tau, \nu) >_{L^2(G)}$, and $\xi_{ik}(\tau, \nu)$ $(i, k = 0, 1, \ldots, N)$ are cross-ambiguity functions induced from the sequence $\{u_i(t)\}_{i=0}^{N}$ by the rule (2.3). Therefore, the optimization problem of interest can be reformulated with respect to the elements of vector $\mathbf{a}$ as it is done in Problem 2.5.1.

It appears, however, that, in the case when the Hermite waveforms are chosen to form the basis in $\mathcal{W}$, it is more convenient to work with other representation of $\|\chi_s(\tau, \nu)\|^2_{L^2(G)}$ which we derive below.

According to Lemma 2.2.3, the ambiguity function of any signal $s(t) \in \mathcal{W}_N$ can be expanded in a finite series

$$\chi_s(\tau, \nu) = \sum_{i=0}^{N} \sum_{k=0}^{N} b_{ik} \xi_{ik}(\tau, \nu), \tag{A.8}$$

where $b_{ik} = a_i \overline{a}_k$ (see (2.5)).

Applying the change of indices $(i,k) \leftrightarrow (p,q)$, given by [41]

$$\left\{ \begin{array}{l} i = p + \dfrac{|q|+q}{2}, \\ \\ k = p + \dfrac{|q|-q}{2}, \end{array} \right. \iff \left\{ \begin{array}{l} p = \left\{ \begin{array}{ll} k, & i \geq k \\ i, & k \leq i \end{array} \right\} = \dfrac{i+k-|i-k|}{2}, \\ \\ q = i-k, \end{array} \right. \tag{A.9}$$

to (A.8) yields the following representation of $\chi_s(\tau,\nu)$:

$$\chi_s(\tau,\nu) = \sum_{q=-N}^{N} \sum_{p=0}^{N-|q|} d_{pq} \widetilde{\xi}_{pq}(\tau,\nu), \tag{A.10}$$

where $d_{pq} = b_{ik}$ and $\widetilde{\xi}_{pq}(\tau,\nu) = \xi_{ik}(\tau,\nu)$ for each set of pairs (i,k) and (p,q) satisfying to (A.9). Then,

$$\|\chi_s(\tau,\nu)\|^2_{L^2(G)} = \sum_{q=-N}^{N} \sum_{p=0}^{N-|q|} \sum_{s=-N}^{N} \sum_{r=0}^{N-|s|} \gamma_{pqrs} d_{pq} \overline{d}_{rs}, \tag{A.11}$$

where

$$\gamma_{pqrs} = < \widetilde{\xi}_{pq}(\tau,\nu), \widetilde{\xi}_{rs}(\tau,\nu) >_{L^2(G)} . \tag{A.12}$$

In this section, we work with the form of $\|\chi_s(\tau,\nu)\|^2_{L^2(G)}$ given by (A.11). Note that we still consider $\|\chi_s(\tau,\nu)\|^2_{L^2(G)}$ as a function of $\mathbf{a}$. Formula (A.11) just provides implicit expression of $\|\chi_s(\tau,\nu)\|^2_{L^2(G)}$ in terms of the elements of $\mathbf{a}$ (representation (A.11) of $\|\chi_s(\tau,\nu)\|^2_{L^2(G)}$ can be easily converted into (A.7) via the procedure described above).

Next, we list some properties of quantities d_{pq} and coefficients γ_{pqrs} useful in our work.

LEMMA A.1.1 *The following statements hold:*

1) If $q \geq 0$, *then* $d_{pq} = a_{p+q}\overline{a}_p$;

2) $d_{p\,0}$ *is real and* $0 \leq d_{p\,0} \leq 1$;

3) If $q \geq 1$, *then* $|d_{pq}|^2 = d_{p+q0} d_{p0}$;

4) $\sum_{p=0}^{N} d_{p0}^2 + 2\sum_{p=0}^{N-1}\sum_{r=p+1}^{N} d_{p0}d_{r0} = 1$;
5) $d_{p(-q)} = \overline{d}_{p\,q}$.

PROOF. The correctness of the first statement of the Lemma follows from the fact that, due to (A.9) and (2.5),

$$d_{pq} = b_{p+q,p} = a_{p+q}\overline{a}_p. \tag{A.13}$$

Therefore,

$$d_{p\,0} = b_{pp} = |a_p|^2 \tag{A.14}$$

and

$$|d_{pq}|^2 = |a_{p+q}|^2|a_p|^2 = d_{p+q0}d_{p0}. \tag{A.15}$$

Formulas (A.14) and(A.15) prove the second and third statements, respectively. We use them to derive

$$\sum_{p=0}^{N} d_{p0}^2 + 2\sum_{p=0}^{N-1}\sum_{r=p+1}^{N} d_{p0}d_{r0} = \left(\sum_{p=0}^{N} d_{p0}\right)^2 = \left(\sum_{p=0}^{N} |a_p|^2\right)^2. \tag{A.16}$$

Since $a_i \in \mathfrak{S}_N$, the last relation implies the correctness of the fourth statement of the lemma.

Finally, to prove the fifth statement, we observe that, for each pair of indices (i,k), $b_{ik} = a_i\overline{a}_k = \overline{a_k\overline{a}_i} = \overline{b}_{ki}$, and, hence,

$$d_{p(-q)} = b_{p+(|-q|-q)/2,\,p+(|-q|+q)/2} = \overline{b}_{p+(|q|+q)/2,\,p+(|q|-q)/2} = \overline{d}_{p\,q}.$$

LEMMA A.1.2 *The coefficients* γ_{pqrs} $(q,s = -N,-N+1,\ldots,N; p = 0,1,\ldots,N-|q|; r = 0,1,\ldots,N-|s|)$ *admit the following representation*

$$\gamma_{pqrs} = \begin{cases} \sqrt{\dfrac{p!r!}{(p+|q|)!(r+|q|)!}}\displaystyle\int_0^{x_0} e^{-x}x^{|q|}L_p^{(|q|)}(x)L_r^{(|q|)}(x)dx, & \text{if } q = s, \\ 0, & \text{if } q \neq s, \end{cases} \tag{A.17}$$

where $x_0 = \pi R^2$. *Moreover,*

$$\gamma_{p(-q)r(-q)} = \gamma_{pqrq} \qquad \text{and} \qquad \gamma_{pqrq} = \gamma_{rqpq}. \tag{A.18}$$

PROOF. We recall from (2.7) that $\widetilde{\xi}_{pq}(\tau,\nu)$ has a simple form as a function of the polar coordinates (r,θ) defined by $\tau + j\nu = re^{j\theta}$:

$$\widetilde{\xi}_{pq}(\tau,\nu) = \sqrt{\pi}\ \Xi_{pq}(r\sqrt{\pi})e^{j\,q\theta}, \tag{A.19}$$

where $\Xi_{pq}(r)$ is given by (2.8).

Now, bearing in mind that G is a circular region (A.1), we compute

$$\begin{aligned}\gamma_{pqrs} &= \iint\limits_{G} \widetilde{\xi}_{pq}(\tau,\nu)\overline{\widetilde{\xi}_{rs}(\tau,\nu)}d\tau d\nu \\ &= \int_0^R \int_0^{2\pi} \pi\Xi_{pq}(r\sqrt{\pi})\Xi_{rs}(r\sqrt{\pi})e^{j\,(q-s)\theta}rdrd\theta \\ &= \pi\int_0^{2\pi} e^{j\,(q-s)\theta}d\theta \cdot \int_0^R \Xi_{pq}(r\sqrt{\pi})\Xi_{rs}(r\sqrt{\pi})rdr. \end{aligned}\tag{A.20}$$

Since the sequence $\{e^{jq\theta}\}_{q=-N}^{N}$ is orthogonal on $0 \le \theta \le 2\pi$, we derive from (A.20) that

$$\gamma_{pqrs} = \begin{cases} 2\pi^2 \displaystyle\int_0^R \Xi_{pq}(r\sqrt{\pi})\Xi_{rs}(r\sqrt{\pi})rdr, & \text{if } q = s, \\ 0, & \text{if } q \ne s. \end{cases} \tag{A.21}$$

Substituting (2.8) into A.21, we obtain

$$\gamma_{pqrq} = 2\pi\sqrt{\frac{p!r!}{(p+|q|)!(r+|q|)!}}\int_0^R e^{-\pi r^2}(\pi r^2)^{|q|}L_p^{(|q|)}(\pi r^2)L_r^{(|q|)}(\pi r^2)rdr. \tag{A.22}$$

Finally, the change of variable $x = \pi r^2$ yields (A.17).

The correctness of formulas (A.18) follows immediately from (A.22). This observation completes the proof of the lemma.

We use the results of Lemmas A.1.1 and A.1.2 to rewrite (A.11) as follows

$$\begin{aligned}\|\chi_s(\tau,\nu)\|^2_{L^2(G)} &= \sum_{p=0}^{N}\gamma_{p0p0}d_{p0}^2 + 2\sum_{p=0}^{N-1}\sum_{r=p+1}^{N}\gamma_{p0r0}d_{p0}d_{r0} + 2\sum_{q=1}^{N}\sum_{p=0}^{N-q}\gamma_{pqpq}|d_{pq}|^2 \\ &\quad + 4\sum_{q=1}^{N}\sum_{p=0}^{N-q}\sum_{r=0}^{p-1}\gamma_{pqrq}\Re\{d_{pq}\overline{d}_{rq}\} \\ &= \sum_{p=0}^{N}\gamma_{p0p0}d_{p0}^2 + 2\sum_{p=0}^{N-1}\sum_{r=p+1}^{N}\left(\gamma_{p0r0}+\gamma_{p(r-p)p(r-p)}\right)d_{p0}d_{r0} \\ &\quad + 4\sum_{q=1}^{N}\sum_{p=0}^{N-q}\sum_{r=0}^{p-1}\gamma_{pqrq}\Re\{d_{pq}\overline{d}_{rq}\}.\end{aligned} \tag{A.23}$$

We also note that, since index q takes only positive values in (A.23), the absolute value sign in (A.17) can be omitted, i.e.,

$$\gamma_{pqrq} = \kappa_{pqrq}\mu_{pqrq}, \tag{A.24}$$

where

$$\kappa_{pqrq} = \sqrt{\frac{p!r!}{(p+q)!(r+q)!}} \quad \text{and} \quad \mu_{pqrq} = \int_0^{x_0} e^{-x}x^q L_p^{(q)}(x)L_r^{(q)}(x)dx. \tag{A.25}$$

Using properties of Laguerre polynomials [37], we compute

$$\begin{aligned}\mu_{pqrq} &= -e^{-x}\eta_{pqrq}(x)\,|_0^{x_0} + \mu_{(p-1)q(r-1)q} + q\mu_{p(q-1)r(q-1)}, \\ \mu_{p000} &= -e^{-x}\eta_{p000}(x)\,|_0^{x_0},\end{aligned}$$

where

$$\eta_{pqrq}(x) = x^q\left(L_p^{(q)}(x) - L_{(p-1)}^{(q)}(x)\right)\left(L_r^{(q)}(x) - L_{(r-1)}^{(q)}(x)\right).$$

Since $L_p^{(0)}(0) = 1$, we observe that

$$\eta_{pqrq}(0) = \begin{cases} 1, & \text{if } q = p = r = 0, \\ 0, & \text{otherwise.}\end{cases}$$

Therefore,

$$\mu_{pqrq} = \frac{(p+q)!}{p!}\left(1-e^{-x_0}\right)\delta_{pr} - e^{-x_0}x_0\widetilde{\mu}_{pqrq},$$

where

$$\widetilde{\mu}_{pqrq} = \left(\eta_{pqrq}(x_0) + \widetilde{\mu}_{(p-1)q(r-1)q} + q\widetilde{\mu}_{p(q-1)r(q-1)} - \frac{(p+q)!}{p!}\delta_{pr}\right)/x_0,$$

$$\widetilde{\mu}_{p000} = \left(\eta_{p000}(x_0) - \delta_{p0}\right)/x_0.$$

Taking into account the fourth statement of Lemma A.1.1, we obtain

$$\begin{aligned} F(\mathbf{a}) &= \left(1-e^{-x_0}\right)\left(\sum_{p=0}^{N} d_{p0}^2 + 2\sum_{p=0}^{N-1}\sum_{r=p+1}^{N} d_{p0}d_{r0}\right) - e^{-x_0}x_0F_1(\mathbf{a}) \\ &= \left(1-e^{-x_0}\right) - e^{-x_0}x_0F_1(\mathbf{a}), \end{aligned}$$

where

$$\begin{aligned} F_1(\mathbf{a}) = \sum_{p=0}^{N}\widetilde{\gamma}_{p0p0}d_{p0}^2 + 2\sum_{p=0}^{N-1}\sum_{r=p+1}^{N}\left(\widetilde{\gamma}_{p0r0} + \widetilde{\gamma}_{p(r-p)p(r-p)}\right)d_{p0}d_{r0} \\ + 4\sum_{q=1}^{N}\sum_{p=0}^{N-q}\sum_{r=0}^{p-1}\widetilde{\gamma}_{pqrq}\Re\{d_{pq}\overline{d}_{rq}\} \end{aligned} \tag{A.26}$$

and $\widetilde{\gamma}_{pqrq} = \kappa_{pqrq}\widetilde{\mu}_{pqrq}$.

It is clear that

$$\arg\min_{s\in\mathcal{W}_N}\|\chi_s(\tau,\nu)\|^2_{L^2(G)} = \arg\min_{\{a_i\}\in\mathfrak{S}_N}F(\mathbf{a}) = \arg\max_{\{a_i\}\in\mathfrak{S}_N}F_1(\mathbf{a}).$$

In other words, we have transformed the problem of minimizing $F(\mathbf{a})$ to the problem of maximizing $F_1(\mathbf{a})$. Replacing the variables $\{d_{pq}\}$ by the variables $\{a_i\}_{i=0}^N$ in (A.26) in accordance with the first statement of Lemma A.1.1 and introducing a new set of real-valued variables $\{y_i^{(1)}, y_i^{(2)}\}_{i=0}^N$, given by $a_i = y_i^{(1)}e^{jy_i^{(2)}}$ $(i = 0, 1, \ldots, N)$, yields $F_1(\mathbf{a}) = G(\mathbf{y})$. This implies the correctness of Lemma A.0.1.

A.2 Proof of Lemma A.0.2

To verify that vector $\widehat{\mathbf{y}}$ is a solution to the problem

$$\text{maximize} \quad G(\mathbf{y}),$$
$$\text{subject to} \quad g(\mathbf{y}^{(1)}) = \mathbf{y}^{(1)}\mathbf{y}^{(1)T} - 1 = 0,$$

we construct the function $G_1(\mathbf{y}, \lambda) = G(\mathbf{y}) - \lambda g(\mathbf{y}^{(1)})$. It is easy to check that $\nabla G_1(\widehat{\mathbf{y}}, \lambda) = 0$ yields $\lambda = \widehat{\lambda} = 2\psi_{NN}$. Then, we consider a quadratic form

$$Q(\mathbf{z}) = \sum_{l,m=1}^{2} \sum_{i,k=0}^{N} \frac{\partial^2 G_1(\widehat{\mathbf{y}}, \widehat{\lambda})}{\partial y_i^{(l)} \partial y_k^{(m)}} z_i^{(l)} z_k^{(m)} \tag{A.27}$$

subject to the constraint

$$\sum_{i=0}^{N} \frac{\partial g(\widehat{\mathbf{y}}^{(1)})}{\partial y_i^{(1)}} z_i^{(1)} = 0 \tag{A.28}$$

(here $\mathbf{z} = (\mathbf{z}^{(1)}, \mathbf{z}^{(2)})$ with $\mathbf{z}^{(i)} = (z_0^{(i)}, z_1^{(i)}, \ldots, z_N^{(i)})$ $(i = 1, 2)$). In our case, function $Q(\mathbf{z})$ and constraint (A.28) can be written as follows:

$$Q(\mathbf{z}) = 4 \sum_{i=0}^{N-1} (\psi_{iN} - \psi_{NN}) \left(z_i^{(1)} \right)^2 \tag{A.29}$$

and $z_N^{(1)} = 0$. Clearly, if $\psi_{iN} - \psi_{NN} < 0$ $(i = 0, 1, \ldots, N-1)$, then form $Q(\mathbf{z})$ is negative definite and, hence, function $G(\mathbf{y})$ considered on ... $g(\mathbf{y}^{(1)})$ attains its maximum at point $\widehat{\mathbf{y}}$.

A.3 Analysis of conditions (2.24)

It follows from (A.4) – (A.6) that the functions $\psi_{iN}(x) - \psi_{NN}(x)$ $(i = 0, 1, \ldots, N-1)$ are polynomials of x:

$$\psi_{iN}(x) - \psi_{NN}(x) = \frac{x}{(N!)^2} p_i^{(N)}(x), \tag{A.30}$$

where $p_i^{(N)}(x)$ are polynomials

$$p_i^{(N)}(x) = \sum_{k=0}^{2N-2} \alpha_{ik}^{(N)} x^k \tag{A.31}$$

such that $\alpha_{i(2N-2)}^{(N)} = -1$ and $\alpha_{i0}^{(N)} < 0$. Hence, conditions (2.24) are fulfilled for both sufficiently small and sufficiently large positive values of x. In more details, if $x_{i,\min}^{(N)}$

and $x_{i,\max}^{(N)}$ are the smallest and largest positive roots of $p_i^{(N)}(x)$, respectively, and $x_{\min}^{(N)} = \min\{x_{0,\min}^{(N)}, x_{1,\min}^{(N)}, \ldots, x_{N-1,\min}^{(N)}\}$, and $x_{\max}^{(N)} = \max\{x_{0,\max}^{(N)}, x_{1,\max}^{(N)}, \ldots, x_{N-1,\max}^{(N)}\}$, then conditions (2.24) are fulfilled for $x \in (0, x_{\min}^{(N)}] \cup [x_{\max}^{(N)}, \infty)$. In general, the problem of finding the values of x belonging to $[x_{\min}^{(N)}, x_{\max}^{(N)}]$ and satisfying (2.24) requires further investigation and remains open. Below we show its solutions for some specific values of N.

If $N = 1$, we deal with only one condition $\psi_{01}(x) - \psi_{11}(x) = -x$ which is negative for all the positive values of x. Hence, in this case, conditions (2.24) are fulfilled for $x \in (0, \infty)$.

If $N = 2$, we have the inequalities

$$\psi_{02}(x) - \psi_{22}(x) = -\frac{x}{4}(x-2)^2 \leq 0$$

and

$$\psi_{12}(x) - \psi_{22}(x) = -\frac{x}{4}(x^2 - 3x + 4) < 0.$$

Therefore, conditions (2.24) are fulfilled for $x \in (0, 2) \cup (2, \infty)$.

Tables A.1, A.2, and A.3 contain the coefficients of the polynomials $p_i^{(N)}(x)$ $(i = 0, 1, \ldots, N-1)$ (see (A.31)) for $N = 3, 4$, and 5, respectively, while Figures A.1, A.2, and A.3 display the intervals on which the polynomials $p_i^{(N)}(x)$ $(i = 0, 1, \ldots, N-2)$ are positive. We do not plot polynomial $p_{N-1}^{(N)}(x)$, since it appears to be negative for all positive values of x. As follows from Figures A.1 and A.2, inequalities (2.24) are true, if $x \in (0, x_1) \cup (x_2, x_3) \cup (x_4, \infty)$, where $x_1 \approx 0.569, x_2 = 6, x_3 \approx 6.851$, and $x_4 \approx 9.756$, for $N = 4$, and $x_1 \approx 0.756, x_2 = 3, x_3 \approx 4.196$, and $x_4 = 6$, for $N = 3$. Similarly, it can be seen from Figure A.3 that, for $N = 5$, conditions (2.24) are fulfilled for $x \in (0, x_1) \cup (x_2, x_3) \cup (x_4, x_5) \cup (x_6, \infty)$, where $x_1 \approx 0.463, x_2 \approx 4.143, x_3 \approx 5.562, x_4 \approx 9.093, x_5 \approx 9.668$, and $x_6 \approx 13.556$.

i	$\alpha_{i4}^{(3)}$	$\alpha_{i3}^{(3)}$	$\alpha_{i2}^{(3)}$	$\alpha_{i1}^{(3)}$	$\alpha_{i0}^{(3)}$
0	-1	12	-57	108	-54
1	-1	12	-45	60	-36
2	-1	12	-54	96	-72

Table A.1: The coefficients of polynomials $p_i^{(3)}(x)$ $(i = 0, 1, 2)$.

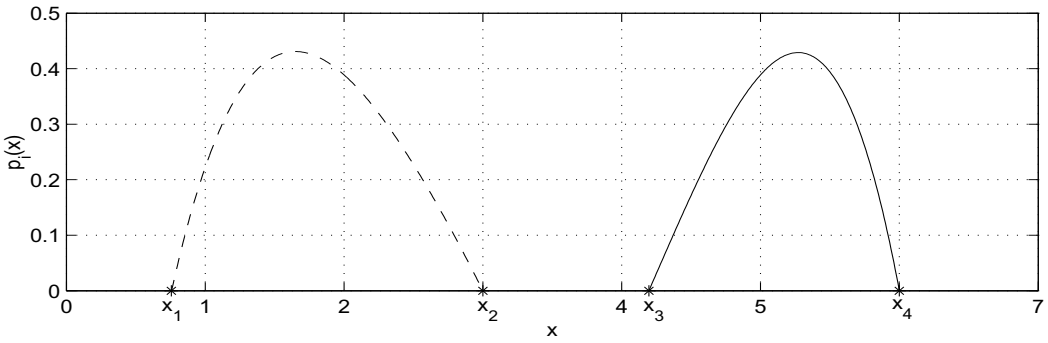

Figure A.1: The polynomials $p_0^{(3)}(x)$ (- -) and $p_1^{(3)}(x)$ (-).

i	$\alpha_{i6}^{(4)}$	$\alpha_{i5}^{(4)}$	$\alpha_{i4}^{(4)}$	$\alpha_{i3}^{(4)}$	$\alpha_{i2}^{(4)}$	$\alpha_{i1}^{(4)}$	$\alpha_{i0}^{(4)}$
0	-1	24	-232	1104	-2736	3264	-1152
1	-1	24	-232	1104	-2568	2592	-864
2	-1	24	-208	816	-1512	1248	-576
3	-1	24	-228	1056	-2520	2880	-1440

Table A.2: The coefficients of polynomials $p_i^{(4)}(x)$ $(i = 0, 1, 2, 3)$.

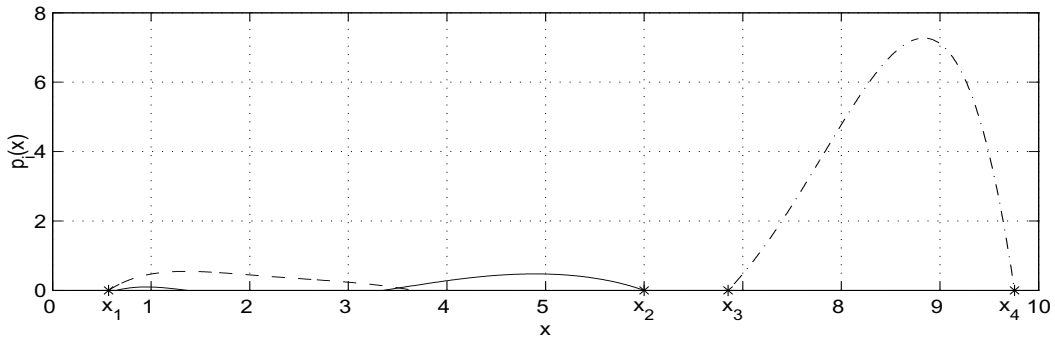

Figure A.2: The polynomials $p_0^{(4)}(x)$ (- -), $p_1^{(4)}(x)$ (-), and $p_2^{(4)}(x)$ (-·-).

i	$\alpha_{i8}^{(5)}$	$\alpha_{i7}^{(5)}$	$\alpha_{i6}^{(5)}$	$\alpha_{i5}^{(5)}$	$\alpha_{i4}^{(5)}$	$\alpha_{i3}^{(5)}$	$\alpha_{i2}^{(5)}$	$\alpha_{i1}^{(5)}$	$\alpha_{i0}^{(5)}$
0	-1	40	-665	5880	-30040	90000	-153000	132000	-36000
1	-1	40	-665	5880	-29800	87120	-140400	110400	-28800
2	-1	40	-665	5880	-29500	83520	-125400	86400	-21600
3	-1	40	-625	4920	-21000	48720	-59400	36000	-14400
4	-1	40	-660	5760	-28800	83520	-136800	115200	-43200

Table A.3: The coefficients of polynomials $p_i^{(5)}(x)$ $(i = 0, 1, 2, 3, 4)$.

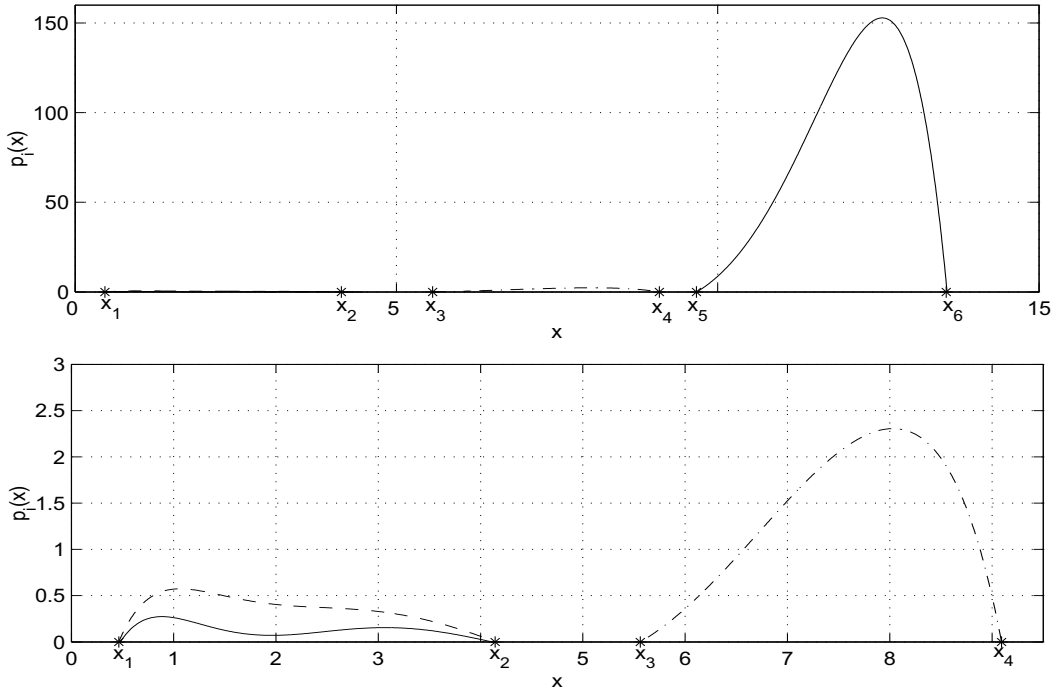

Figure A.3: The polynomials $p_i^{(5)}$ $(i = 0, 1, 2, 3)$. Top: zoom on interval $[0, 15]$; $p_4^{(5)}(x)$ (-). Bottom: zoom on interval $[0, 9.5]$; $p_0^{(5)}(x)$ (- -), $p_1^{(5)}(x)$ (-), and $p_2^{(5)}(x)$ (-·-).

Bibliography

[1] R.H. Barker, Group synchronization of binary digital systems, *in: Communication Theory*, Academic Press, 1953, pp. 273-287.

[2] R.E. Blahut, Theory of Remote Surveillance Algorithms, in "Radar and Sonar", Part 1, Springer-Verlag, 1991, p. 1-65.

[3] L. Bomer and M. Antweiler, Polyphase Barker sequences, *Electronics Letters*, vol. 25, no. 23, 1989, pp. 1577-1579.

[4] A. Bonami, B. Demange, and Ph. Jamming, Hermite functions and uncertainty principle for the Fourier and the windowed Fourier transforms, *Revista Mathematica Iberoamericana*, 19, 2003, pp. 23-55.

[5] M.N. Cohen, An overview of high range resolution radar techniques, *Proc. of The National Telesystems Conference*, 1991, pp. 107-115.

[6] M.N. Cohen, J.M. Baden, and P.E. Cohen, Biphase codes with minimum peak sidelobes, *Proc. of the IEEE National Radar Conference*, 1989, pp. 62-66.

[7] M.N. Cohen, M.R. Fox, and J.M. Baden, Minimum peak sidelobes pulse compression codes, *Proc. of the IEEE International Radar Conference*, 1990, pp. 633-638.

[8] C.E. Cook and M. Bernfeld, Radar Signal: An Introduction to Theory and Applications, Academic Press Inc., New York, 1967.

[9] J.P. Costas, A study of a class of detection waveforms having nearly ideal range-Doppler ambiguity properties, *Proc. of the IEEE*, vol. 72, no. 8, 1984, pp. 996-1009.

[10] G.E. Coxson, A. Hirschel, and M.N. Cohen, New results on minimum-PSL binary codes, *Proc. of the 2001 IEEE Radar Conference*, 2001, pp. 153-156.

[11] A.F. Culmone, Properties of uniform coherent frequency-jump waveforms, Technical Note, MIT Lincoln Lab, April 1973, 36 p.

[12] M. Friese, Polyphase Barker sequences up to length 36, *IEEE Trans. on Information Theory*, vol. 42, no. 4, 1996, pp. 1248-1250.

[13] M. Friese and H. Zottmann, Polyphase Barker sequences up to length 31, *Electronics Letters*, vol. 30, no. 23, 1994, pp. 1930-1931.

[14] I. Gladkova and D. Chebanov, On a new extension of Wilcox's method, *WSEAS Trans. on Mathematics*, Vol. 3, Issue 1, 2004, pp. 244-249.

[15] I. Gladkova and D. Chebanov, On the synthesis problem for a waveform having a nearly ideal ambiguity surface, *Proc. of the International Conference RADAR 2004*, CD-ROM.

[16] I. Gladkova and D. Chebanov, Suppression of grating lobes in stepped-Frequency train, *Proc. of the 2005 IEEE International Radar Conference*, Arlington, USA, 2005, 371-376. .

[17] S.W. Golumb and H. Taylor, Constructions and properties of Costas arrays, *Proc. of the IEEE*, vol. 72, no. 9, 1984, pp. 1143-1163.

[18] E. Kelly and R. Wishner, Mathched-filter theory for high-velocity accelerating targets, *IEEE Trans. on Military Electronics*, vol. 9, 1965, pp. 56-69.

[19] J.R. Klauder, The design of radar signals having both high range resolution and high velocity resolution, *Bell System Tech. J.*, vol. 39, no. 4, 1960, pp. 809-820.

[20] N. Levanon, Stepped-frequency pulse-train radar signal, *IEE Proc. - Radar, Sonar, and Navigation*, Vol. 149, No. 6, December 2002, pp. 297-309.

[21] N. Levanon and E. Mozeson, Nullifying ACF Grating Lobes in Stepped-Frequncy Train of LFM Pulses, *IEEE Transactions on Aerospace and Electronic Systems*, Vol. 39, No. 2, April 2003, pp. 694-703.

[22] N. Levanon and E. Mozeson, Radar Signals, Wiley, New York, 2004.

[23] D.E. Maron, Non-periodic frequncy-jumped burst waveforms, *Proc. of the IEE International Radar Conference*, 1987, pp. 484-488.

[24] D.E. Maron, Frequncy-jumped burst waveforms with stretch processing, *Proc. of the IEEE International Radar Conference*, 1990, pp. 274-279.

[25] W. Miller, Topics in harmonic analysis with applications to radar and sonar, in "Radar and Sonar", Part I, Springer-Verlag, 1991, pp. 66-168.

[26] B. Moran, Mathematics of Radar, in "20th Century Harmonic Analysis – A Celebration", Kluwer Publ., 2000, pp. 295-328.

[27] P. Peebles, Radar Principles, Wiley-Interscience, 1998.

[28] R. Price and E.M. Hofstetter, Bounds on the volume and height distributions of the ambiguity function, *IEEE Trans. on Information Theory*, vol. IT-11, April 1965, pp. 207-214.

[29] D.J. Rabideau, Nonlinear synthetic wideband waveforms, *Proc. of the IEEE Radar Conference*, 2002, pp. 212-219.

[30] M. Richards, Radar Signal Processing, ATlanta, Georgia Tech, 2004.

[31] F. Riesz and B. Sz.-Nagy: Functional Analysis, F. Ungar Publishing Co., New York, 1955.

[32] A.W. Rihaczek, Principles of High-Resolution Radar, Artech House, 1996.

[33] A.W. Rihaczek, Radar resolution of moving targets, *IEEE Trans. on Information Theory*, vol. 13, 1967, pp. 51-56.

[34] A.W. Rihaczek, Delay-Doppler Ambiguity function for wideband signals, *IEEE Trans. on Aerospace Electronics and Systems*, vol. 3, 1967, pp.705-711.

[35] M. Skolnik, Introduction to Radar Systems, McGraw-Hill, 3rd edition, 2002.

[36] S.M. Sussman, Least-square synthesis of radar ambiguity functions, *IRE Trans. on Information Theory*, Vol.IT-8, 1962, pp. 246-254.

[37] G. Szego, *Orthogonal Polynomials*, AMS Colloguium Publications, V. XXIII, New York, 1939

[38] E.C. Titchmarsh, Introduction to the theory of Fourier integrals, Oxford University Press, Oxford, 1937.

[39] D.R. Wehner, High-Resolution Radar, Artech House, 2nd edition, 1995.

[40] P.M. Woodward, Probability and Information Theory, with Applications to Radar, Pergamon Press, 1953.

[41] C.H. Wilcox, The synthesis problem for radar ambiguity functions, MRC Tech. Summary Report 157, US Army, Univ. of Wisconsin, Madison, Wisconsin, April 1960.

[42] C.H. Wilcox, The synthesis problem for radar ambiguity functions, in "Radar and Sonar", Part I, Springer-Verlag, 1991, p. 229-260.

[43] C.H. Wilcox, Sonar and radar echo structures, in "Radar and Sonar", Part I, Springer-Verlag, 1991, p. 169-228.

[44] R.M. White, B.H. Cantrell, J.P. McConnell, and J.J. Alter, Delta-Sigma Waveform Generation for Digital Radars, *Proc. of the 2004 IEEE Radar Conference*, CD-ROM.